EPFL

Thèse n° 9050

Defect formation and mitigation during laser powder bed fusion of copper

Présentée le 15 octobre 2021

Faculté des sciences et techniques de l'ingénieur
Laboratoire des matériaux photoniques et caractérisation
Programme doctoral en science et génie des matériaux

pour l'obtention du grade de Docteur ès Sciences

par

Carl Tore Viktor LINDSTRÖM

Acceptée sur proposition du jury

Prof. J. Brugger, président du jury
Prof. P. Hoffmann, Dr C. Leinenbach, directeurs de thèse
Dr I. Matthews, rapporteur
Prof. L. Nyborg, rapporteur
Prof. R. Logé, rapporteur

École
polytechnique
fédérale
de Lausanne

2021

Acknowledgements

Without the help and support of numerous people this thesis, which was written during my stay at the Swiss Federal Laboratories for Materials Science and Technology (Empa) and founded through the SFA-AM PREAMPA project, would have never been possible.

First and foremost I would like to thank my thesis directors: Dr. Christian Leinenbach, my thesis co-director, group leader and supervisor at Empa, and Prof. Patrik Hoffman, my thesis director and laboratory head at Empa. Dr. Leinenbach has through continuous feedback and scientific discussions helped me develop as a scientist, and I am in particular grateful for his assistance with my scientific writing, his guidance in helping manage my PhD project, and his unwavering support. His management of the group "Alloy design for advanced processes" has lead to a great team-spirit and friendly atmosphere, which has made working at Empa a pleasure. Prof. Hoffman has provided invaluable feedback and input on my scientific work, and I am deeply thankful for all discussions we have had throughout the last four years.

I am also thankful for the scientific collaborations I have had throughout the last years. I would like to mention in particular my experimental collaborators Dr. Oleksii Liashenko, Dr. Kai Zweiacker, Dr. Seth Griffiths, Sayedpayam Vadahti, Dr. Li Xiaoshuang, Dr. Yevhen Shynkarenko, Serhii Derevianko, Serhii Derevianko, Dr. Tri Le Quang, and Dr. Xiao Jia, who have been of great assistance and support in designing and carrying out experiments. I would also like to thank Dr. Kim Le Quy, Dr. Valdyslav Turlo, Dr. Giandomenico Lupo, and Magnus Carlsson for the discussions we had on various aspects of the simulation of LPBF. These discussions gave me the confidence to start working on CFD simulations and the tips and ideas helped greatly in performing the simulations.

The work would also not have been possible without the amazing support staff at Empa: Franz Stebler and his colleagues in the machine shop, Alexandra Lau and Peter Ramseier in the metallography labs, Robin Pauer in the electron microscope center, and Christian Affoltern and Bernhard von Gunten in Thun.

I would furthermore like to thank all my former and current colleagues in the group, Dr. Toni Ivas, Dr. Ariyan Arabi-Hashemi, Dr. Kai Zweiacker, Dr. Li Xiaoshuang, Dr. Oleksii Liashenko, Dr. Seth Griffiths, Rafał Wrobel, Marvin Schuster, Irene Ferretto, Dr. Anthony de Luca, Di Cui, Marc Leparoux, Antonios Barganis, Xiao Jia, and Jian Yang for all the interesting discussions, excursions, coffee breaks and long lunches. You all made my time at Empa something special.

I would also like to thank my other colleagues of department 204 and 206 in Thun, who always made me feel welcome when visiting.

Finally I would like to thank my family and friends. In particular I would like to thank my wife, Franziska. Franziska has supported and motivated me when I needed it, and distracted me when I needed that. Her help during my doctorate studies cannot be understated.

Wald ZH, September 30, 2021 Viktor Lindström

Abstract

Additive manufacturing (AM) is a group of processing technologies which has the potential to revolutionize manufacturing by allowing easy manufacturing of complex shapes and small series. One AM-method which is of high interest for processing of metals is laser powder bed fusion (LPBF), where a powerful laser is used to melt powder in a layer-by-layer fashion into a consolidated part. Many defects can form during LPBF processing, but copper, copper alloys, and similar metals are particularly prone to the formation of pores. The reason why these metals tend to have these defects is the high reflectivity decreasing the effective energy input, and the high thermal conductivity transporting the absorbed energy away.

Several ways of decreasing the pore formation tendency are known: increasing the power, increasing the absorptivity, and alloying to decrease thermal conductivity. The relative effectiveness of these strategies are however not known, making it difficult to choose the correct strategy for the different industrial applications of these metals. In this thesis a simple analytical model for predicting the occurrence of these defects is proposed, allowing a lowest possible processing power given the material properties to be estimated. The model agrees well with experiments, and can be used to predict the transition from so called balling mode processing to conduction mode processing, and for qualitative analysis of different processing strategies.

Two strategies of decreasing the porosity are proposed and tested: coating of the powder with an absorbing layer and processing with a green laser, which is mor e strongly absorbed by copper than the conventional IR-lasers. The copper powder was coated with thin layers of tin and nickel using a simple and cheap immersion deposition method, and it is shown that the amount of porosity is decreased more than can be expected of the alloying alone, showing both that the method is working and that laser interaction with the solid is important for the heat balance of the system.

The interaction with the solid is shown through computational fluid dynamics simulations to arise from periodic fluctuations of the molten metal which cause laser light to be reflected forward, pre-heating the powder bed. The preheating is larger the higher the solid absorptivity is, explaining the porosity decrease when using coated powders, and shows that processing using a green laser increase the laser coupling more than the absorptivity of the liquid would. Single line tracks made from fine 5 µm pure copper with a green laser source show that the desired conduction mode melting can be achieved at a power below 70 W, an order of magnitude lower than what is needed for processing of the conventionally used 45 µm powder with an IR-laser.

Zusammenfassung

Additive Fertigung (AM) ist ein Fertigungsbereich mit dem Potential, die Produktion komplexgeometrischer Beuteile und kleiner Serien zu revolutionieren. Eine interessante AM-Methode zur Verar-beitung von Metallen ist das Laserpulverbettschmelzen (LPBF), bei dem ein Laser benutzt wird, um ein Pulver schichtweise zu schmelzen. Verschiedene Defekte wie Poren oder Risse können während der LPBF-Verarbeitung auftreten. Kupfer, Kupferlegierungen, und ähnliche Metalle sind besonders anfällig für die Porenbildung. Der Grund dafür ist die hohe Reflektivität, welche den effektiven Wärmeeintrag senkt, sowie die hohe Wärmeleitfähigkeit dieser Metalle, welche die absorbierte Wärme rasch von der Schmelze abtransportiert. Mehrere Methoden zur Reduktion der Porenbildung sind bekannt, zum Bei-spiel die Erhöhung von Laserleistung, die Erhöhung der Absorbtivität des Kupferulvers, und Legieren, um die Wärmeleitfähigkeit zu vermindern. Die relative Effektivität dieser Methoden ist jedoch nicht be-kannt, so dass es schwierig ist die optimale Strategie für jede Situation zu finden. In dieser Doktorarbeit wird ein einfaches analytisches Modell zur Bildung dieser Poren vorgeschlagen. Das Modell erlaubt es, eine minimale Leistung für die LPBF-Verarbeitung unter Einbezug der Materi-aleigenschaften zu berechnen. Die experimentelle Validierung des Modells demonstriert eine gute Vor-hersage des Übergangs vom unerwünschten "Ballingmodus zum erwünschten Wärmeleitungsschweis-sen und kann dazu benutzt werden, eine qualitative Analyse verschiedener Verarbeitungsstrategien durchzuführen. Zwei Strategien zur Porenreduktion werden vorgeschlagen und getestet: Das Beschichten des Pulvers mit einer absorbierenden Schicht und die Verarbeitung mit einem grünen Laser anstelle eines konventionellen Infrarot-Lasers. Das Kupferpulver wird mit einer einfachen und günstigen Zinn- und Nickelim-mersionsdeposition beschichtet, und es wird gezeigt, dass die damit verarbeiteten Teile weniger Poren aufweisen, als durch die Legierung allein erklärbar ist. Somit wird nicht nur demonstriert, dass die Me-thode funktioniert, sondern auch, dass die Absorption im Festkörper eine wichtige Rolle spielt. Anhand von Fluiddynamiksimulationen wird weiterhin gezeigt, dass die optische Interaktion mit dem Festkörper von periodischen Fluktuationen der Flüssigkeit herstammt. Das Laserlicht wird von der Be-wegungsrichtung aus nach vorne reflektiert, heizt damit das Pulver vor und erhöht die Totalabsorption. Je höher die Festkörperabsorption, desto relevanter wird diese, was die Porenreduktion der geschich-teten Pulvers erklärt. Weiter zeigen die Simulationen, dass die Verarbeitung mit einem grünen Laser die Totalabsorption durch multiple Reflexionen deutlich erhöht. Einzelschicht-LPBF-Versuche mit einem grü-nen Laser und feinem 5 µm Pulver zeigen, dass der erwünschte Wärmeleitungsmodus mit weniger als 70 W Laserleistung erreicht werden kann. Dies ist eine Grössenordnung tiefer als bei der Verarbeitung mit konventionellen 45 µm Pulver und IR-Laser.

Contents

Acknowledgements **i**

Abstract (English/Deutsch) **iii**

List of Figures **xi**

List of Tables **xiii**

1 Introduction **1**

2 State of the art **5**
2.1 Additive manufacturing 6
2.2 The physics of Laser Powder Bed Fusion 8
2.2.1 Heat transfer 8
2.2.2 Momentum transfer 12
2.2.3 Laser-material interaction 13
2.3 Defects in Laser Powder Bed Fusion 16
2.3.1 Porosity 16
2.3.2 Cracks 18
2.3.3 Other defects 19
2.4 Laser powder bed fusion of group 11 metals and alloys 20
2.4.1 Laser powder bed fusion of gold, silver, and their alloys 20
2.4.2 Laser powder bed fusion of copper and copper alloys 22
2.5 Simulation and modeling of LPBF processes 23
2.5.1 Micro-scale modeling 23
2.5.2 Meso-scale modeling 24
2.5.3 Macro-scale modeling 26
2.6 Aim of thesis 26

3 Fluid dynamics simulation of LPBF **29**
3.1 Phase field and momentum equation 29
3.2 Temperature field 30
3.3 Temperature and phase dependence of physical properties 32
3.4 Physical parameters and numerical schemes 33

4 Materials and methods 39
4.1 Laser processing setups 39
4.1.1 Laser powder bed fusion 39
4.1.2 Combined IR and green laser welding 40
4.1.3 Single LPBF line tracks with green laser 41
4.1.4 Single LPBF line tracks with IR laser 42
4.2 Analysis of LPBF parts 42
4.3 Coating of powder using immersion deposition 43

5 The balling phenomenon 45
5.1 A model for the balling phenomenon 45
5.1.1 The substrate temperature field 47
5.1.2 The shape of the cap in balling mode 49
5.1.3 A criterion for balling 51
5.1.4 The balling criterion in terms of the normalized enthalpy 52
5.2 LPBF of copper and copper alloys at low power 52
5.2.1 The role of oxygen for balling in copper based alloys 53
5.2.2 The porosity and melt pool width as a function of the balling number . . 54
5.3 Simulation of the balling phenomenon 55
5.4 Conclusions 58

6 Powder coating as an alloying strategy for pore reduction 61
6.1 Immersion depositions for powder coating 61
6.1.1 Coating of powder 63
6.2 LPBF of coated powders 67
6.2.1 Characteristics of powders used for laser powder bed fusion 67
6.2.2 Comparison of LPBF of coated powders with powder mixtures 69
6.2.3 Pore morphology 72
6.2.4 Occurance of cracks 73
6.2.5 Conclusions 73

7 Processing of copper with green laser 77
7.1 Laser welding of copper 78
7.1.1 Theoretical laser welding processing maps 78
7.1.2 Combined IR and green laser welding of copper 83
7.2 LPBF with green laser 86
7.2.1 Simulation of LPBF of copper with green and IR laser 86
7.2.2 Back reflection measurement of single LPBF tracks 88
7.2.3 Single LPBF tracks of copper with green laser 90
7.3 Conclusions 90

8 Conclusion and outlook 93

A Detailed derivations **97**
A.1 Derivation of equation 5.5 on dimensionless form 97
A.2 Width to depth ratio in balling mode 98

Bibliography **101**

Curriculum Vitae **115**

List of Figures

1.1 Reflectivity and conductivity of the elements at room temperature 3

2.1 The business case for AM 7
2.2 Schematic and picture of a typical LPBF machine 8
2.3 Gaussian beam profile and the reflection of a laser beam. 14
2.4 The reflectivity at normal incidence for copper 16
2.5 The melting mode and nomenclature of LPBF melt tracks 17
2.6 Pores occuring in LPBF 19

3.1 Illustration of the laser tracing algorithm 31

4.1 Sample placement on the build plate and scanning strategies used 40
4.2 Schematic of combined green and IR laser welding setup 41
4.3 Schematic of IR laser processing setup for back-reflection measurements. . . . 42

5.1 The heat flow in balling and conduction mode 46
5.2 Geometry of a cap in LPBF 49
5.3 The parameters of a LPBF cap as a function of the wetting radius 50
5.4 The normalized temperature field of a single LPBF track 51
5.5 Relative density for pure copper samples at different chamber oxygen concentrations 53
5.6 Metallographic cross-sections of LPBF bronze samples processed at different power 55
5.7 The transition from balling to conduction mode expressed in terms of the balling number for the processed materials 56
5.8 CFD simulation showing the cap shape around the balling threshold 58
5.9 CFD simulation showing fluctuations in balling mode 59

6.1 The steps of the powder coating process. 64
6.2 The morphology of Sn-coated copper powder and the corresponding reflection spectra for powders produced at different concentrations of Sn_2^+ 65
6.3 The coating morphology of nickel-coated copper powders with different thiourea concentrations 65
6.4 The composition and reflectivity of coated powders used for LPBF-processing . 68

6.5 Comparison of the absorptivity predicted by Boley et al. with the measured values of the coated powders 68
6.6 Morphology of coated powders used for LPBF processing 69
6.7 Relative density of coated and non-coated powders processed by LPBF 71
6.8 Pore morphology of samples made from the coated and non-coated powders in section 6.2.2 72
6.9 X-ray tomography of sample made from pure copper and coated copper powder. 73
6.10 Crack morphology in samples madefrom coated powders 74
6.11 Sample manufactured with a high total heat input to reduce cracking 74

7.1 Two hypothetical situations for the absorption of laser light in LPBF processing. 78
7.2 Computational domain used for CFD simulations of laser welding 79
7.3 CFD simulations showing the different melting modes in laser welding 80
7.4 Simulated processing maps for laser welding with green and IR laser 82
7.5 Simulated melt pool width at for laser welding at 100 mm s^{-1} with green and IR-laser. 82
7.6 Melt pools from the pulsed green Q-switched laser 84
7.7 Threshold for melt initiation in dual laser welding of copper 85
7.8 Simulation of time-dependence of reflectivity for LPBF processing of copper. . 87
7.9 Absorptivity as a function of laser power in LPBF of copper 88
7.10 Back-reflection measurements single LPBF tracks of bronze powder 89
7.11 Confocal microscope height map of LPBF line scans of copper with green laser 91

A.1 Depth-to-width ratio of melt pools in etched 316L samples 99

List of Tables

2.1 Summary of the most common AM technologies 7

3.1 CFD model parameters used for simulating bronze. 35
3.2 CFD model parameters used for simulating copper 36
3.3 Boundary conditions used for simulations 37

5.1 The scanning speed (v) and the corresponding Peclet number (Pe) calculated from the room temperature thermal diffusivity (D) for the different materials at the experimental conditions 54
5.2 Physical model parameters and the corresponding balling threshold. 54

6.1 The half cell reactions for the coating reactions with their standard potential . . 63
6.2 Detailed recipes for coating of copper powders 66

7.1 Model parameters for the reflectivity model 79

1 Introduction

Additive manufacturing (AM) is a relatively new class of manufacturing techniques characterized by the repeated addition of material. This approach has several advantages compared to classical machining and casting techniques as it allows a fast development cycle, a high degree of part customization, as well as the possibility to create complex shapes. Of particular interest is the use of shapes like lattice structures and internal channels which are often impossible, or very difficult, to manufacture using the more conventional approaches. The incorporation of such geometries in industrial parts can add a significant advantage by reducing weight, allowing operation at higher temperatures, and reducing material waste in the production.

Several approaches are possible for AM of metals, differing in how the raw material is supplied and consolidated. One of the most widely adapted technology is laser powder bed fusion (LPBF), which operates by coating a substrate with a feedstock powder and using a laser to melt a pattern which quickly resolidifies. After the pattern has been made the substrate is lowered and the process repeated layer by layer until the desired three-dimensional shape is ready. This technique allows the production of parts with details on the order of 100 µm and, depending on the specific machine used, a part size on the order of decimeters.

Copper is, together with gold and silver, special in having a very high electrical and thermal conductivity, almost $400\,\mathrm{W\,m^{-1}\,K^{-1}}$ at room temperature, making it useful in thermal and electrical applications. In these applications there is large potential benefit to gain by complex designs, allowing optimal flow of heat and current, as well as possible weight savings, which is interesting both due to the high density and metal cost. Because of this LPBF of copper and copper alloys has attracted industrial attention. Laser processing of copper is however challenging, not only due to the high thermal conductivity but also the high reflectivity in the near infrared spectrum (c:a 99 %) which is used in most LPBF laser sources. The extreme values of these two properties separate copper and the similar metals gold and silver from the rest of the elements, as shown in figure 1.1, and as a result these materials are susceptible to so called balling and lack-of-fusion defects. These defects occur when the heat input into the material is too low and lead to varying degrees of porosity, which adversely influence mechanical properties. It is known that these defects can be alleviated by increasing the laser power or absorptivity, alloying to increase thermal conductivity, lowering the scanning speed, preheating the substrate, as well as other changes of the parameters. How the different approaches relate to each other and the specific mechanisms of pore formation and reduction is however not well understood, making it difficult to choose the optimal strategy for different situations.

In this thesis the formation of balling defects is studied through experiment, numerical simulations and analytical models for the heat transfer. A simple numerical criterion for the presence of balling defects is found, and is used to propose a dimensionless number which can be used to predict the porosity independent on the material. Based on this criterion two approaches for alleviating balling defects are proposed and investigated: alloying by coating the powder with a thin layer of the alloying element, and increasing the absorptivity by processing with a green laser source. The coating of the powder is shown to reduce the porosity more than can be expected by the addition of alloying elements alone, something which is attributed to reflected light shining on the powder in front of the melt pool. The use of a green laser is also shown to be a feasible method to process copper at low power, and it is shown that balling can be avoided at power as low as 70 W using such a laser in combination with fine powder sizes.

The work presented in this thesis adds to the understanding of how the process parameters influence the formation of defects. This knowledge is important for further development of strategies for improving the quality of LPBF parts made from not only copper, but also other metals which are prone to balling defects, like gold, silver, and aluminum. Improved processing strategies can lead to a wider implementation of LPBF of these metals, allowing increased thermal efficiency, cheaper manufacture of complex parts, and a reducing the need for keeping spare parts in stock.

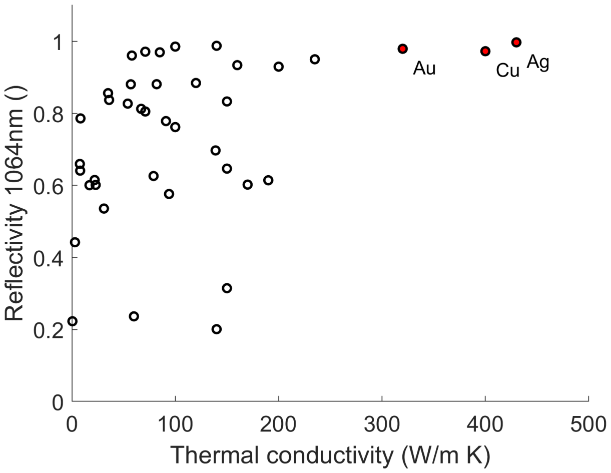

Figure 1.1 – The metals of group 11 of the periodic table are unique with high IR-reflectivity and thermal conductivity, here shown together with a selection of the pure elements. Data compiled from a selection of sources [93, 128, 19, 68, 105].

2 State of the art

In this chapter the state of the art of Laser Powder Bed fusion (LPBF), also known as Selective Laser Melting (SLM), of copper and the similar metals from the same group of of the periodical table, gold, and silver, is presented together with a summary of the physical processes most important for LPBF processing. The chapter is to large parts based on review articles and journal publications. Section 2.2 is based on standard textbooks like *Fundamentals of Mass, Heat, and Momentum Transfer* [143] for the transport equations of heat and momentum, *Solid State Physics* [68] for the thermophysical behavior of metals, *Laser Processing and Chemistry* [5] for the section on laser-material interaction, and *Introduction to Computational Fluid Dynamics* [137] for how the momentum equations can be solved using the finite volume method (FVM).

The following notation is used for vector equations:

Scalar	s	$\mathbb{R}$
Vector	$\vec{a} = (a_x, a_y, a_z)$	$\mathbb{R}^3$
Matrix	$M = \begin{bmatrix} M_{xx} & M_{xy} & M_{xz} \\ M_{yx} & M_{yy} & M_{yz} \\ M_{zx} & M_{zy} & M_{zz} \end{bmatrix}$	$\mathbb{R}^3 \otimes \mathbb{R}^3$
Inner product	$\vec{a} \cdot \vec{b} = a_x b_x + \dots$	$\mathbb{R}^3 \to \mathbb{R}$
Outer product	$\vec{a}\vec{b} = \begin{bmatrix} \vec{a}_x\vec{b}_x & \vec{a}_x\vec{b}_y & \vec{a}_x\vec{b}_z \\ \vec{a}_y\vec{b}_x & \vec{a}_y\vec{b}_y & \vec{a}_y\vec{b}_z \\ \vec{a}_z\vec{b}_x & \vec{a}_z\vec{b}_y & \vec{a}_z\vec{b}_z \end{bmatrix}$	$\mathbb{R}^3 \to \mathbb{R}^3 \otimes \mathbb{R}^3$
Scalar gradient	$\nabla s = (\partial s/\partial x, \partial s/\partial y, \partial s/\partial z)$	$\mathbb{R} \to \mathbb{R}^3$
Vector gradient	$\nabla \vec{a} = \begin{bmatrix} \partial a_x/\partial x & \partial a_y/\partial x & \partial a_z/\partial x \\ \partial a_x/\partial y & \partial a_y/\partial y & \partial a_z/\partial y \\ \partial a_x/\partial z & \partial a_y/\partial z & \partial a_z/\partial z \end{bmatrix}$	$\mathbb{R}^3 \to \mathbb{R}^3 \otimes \mathbb{R}^3$
Vector divergence	$\nabla \cdot \vec{a} = \partial a_x/\partial x + \dots$	$\mathbb{R}^3 \to \mathbb{R}$
Matrix divergence	$\nabla \cdot M = \begin{bmatrix} \partial M_{xx}/\partial x + \partial M_{xy}/\partial y + \partial M_{xz}/\partial z \\ \partial M_{yx}/\partial x + \partial M_{yy}/\partial y + \partial M_{yz}/\partial z \\ \partial M_{zx}/\partial x + \partial M_{zy}/\partial y + \partial M_{zz}/\partial z \end{bmatrix}$	$\mathbb{R}^3 \otimes \mathbb{R}^3 \to \mathbb{R}^3$

2.1 Additive manufacturing

Additive manufacturing (AM) is a group of manufacturing technologies where parts are manufactured by addition of material in a layer by layer fashion, rather than as in conventional technologies where material is removed (machining) or added all at once (for example casting). In the 1980's stereolithography, where an UV-laser is used to cure a polymer resin [49], was the first AM technology to be developed [104]. Since then a plethora of technologies have been developed, not only for polymer parts, but also for production of metallic parts, ceramics, and concrete [104], as summarized in table 2.1. These technologies differ by the method in which the material is supplied and how the material is bonded together. A group of technologies important for processing of metal is powder bed fusion (PBF), where the raw material is supplied through a bed of powder. The powder is melted or sintered either using a laser beam, called laser powder bed fusion, or with an electron beam, called electron beam powder bed fusion (EPBF) [79]. Another popular method for AM of metals is direct energy deposition, (DED) where either powder is focused through a nozzle or a metal wire is fed into the laser beam where it melts and deposits the molten metal on the substrate. DED it is popular not only for part fabrication, but also for repairing expensive and heat sensitive parts like turbine blades [90].

Although AM started out as a technology for rapid prototyping [144] the areas of use have been expanded and it is now a standard manufacturing method for production parts [2]. One of the key benefits of AM is that it gives a large design freedom, compared to traditional manufacturing methods. Examples include shapes like lattices, allowing significant weight savings [150], and internal cooling structures, which can increase thermal efficiancy. Meta-structures can also be manufactured, allowing parts as a whole to exhibit properties which are impossible for regular materials. This can be for example a phononic band-gap which prevents vibrations of certain wavelength to pass, which is of interest for applications like seismic or acoustic dampening [102], or structures with negative Poisson ratios [14].

Another benefit of AM is the quick turnover from idea to the finished product. Apart from prototyping this is of high added value where individualized parts are wanted, for example in jewelry [21] and medical implants [75]. Furthermore it allows keeping a smaller inventory, or the delocalized manufacture of parts, which can significantly reduce costs [118]. Other benefits include the possibility to manufacture multi-material structures as one part, resulting in simpler and more effective designs [47].

The main downside of AM processing in general is that the processing, especially of simple parts, can be slow compared to conventional technologies. Scaling the output of AM processing also does not improve the efficiancy significantly, meaning that the parts do not get much cheaper if produced in large series. This is illustrated by the schematic illustration in figure 2.1 where the unit cost is plotted against units produced. Because of this the target applications will tend to be small series or complex structures where the low investment costs still make the product cheaper [113].

Table 2.1 – Summary of the most common AM technologies

Technology	**Materials**	**Material delivery method**	**Bonding mechanism**
Laser Powder Bed Fusion	Metals	Powder bed	Melting with laser beam
Electron Powder Bed Fusion	Metals	Sintered powder bed	Melting with electron beam
Direct Energy Deposition	Metals	Powder stream or wire feed	Melting with laser beam
Binder jetting	Metals	Powder bed	Deposition of binder and sintering
Laminated Object Manufacturing	Metals, Polymers, Paper	Sheets	Cutting and bonding
Stereolithography	Polymer	Polymer resin	Curing with UV-laser
Fused Deposition	Polymer	Deposition of molten material	Solidification
Inkjet printing	Ceramics	Ink deposition	Evaporation of solvent

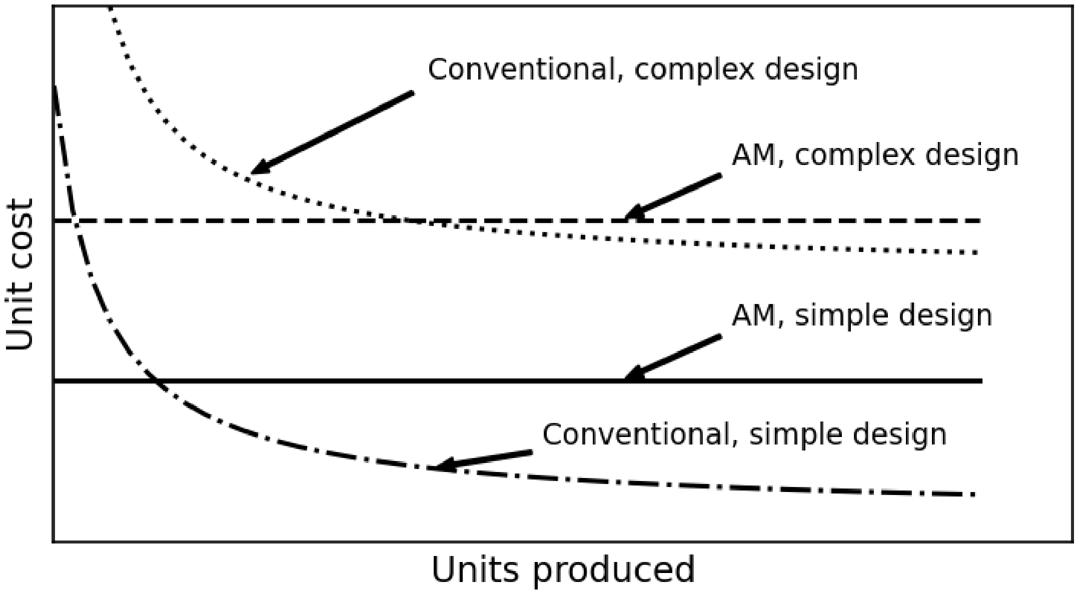

Figure 2.1 – The business case for additive manufacturing is the strongest for small series of complex parts. Here the unit cost is schematically shown plotted against the number of parts produced for a simple and complex geometry. The more complex the part the larger production volume is profitable to produce using AM. Adapted from [113].

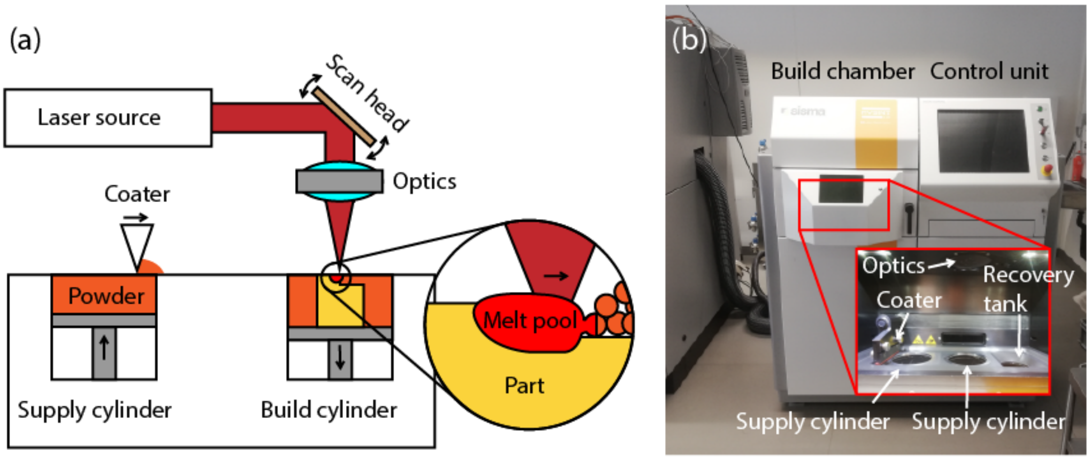
(a)
Laser source
Scan head
Optics
Coater
Powder
Supply cylinder
Build cylinder
Melt pool
Part
(b)
Build chamber
Control unit
Optics
Recovery tank
Coater
Supply cylinder
Supply cylinder

Figure 2.2 – (a) Schematic of a typical LPBF machine. (b) Photograph of a SISMA MySint 100 commercial LPBF machine.

LPBF was developed in U.S.A. in the 1980's, then named *selective laser sintering* [25]. A typical LPBF machine is illustrated in figure2.2, the coater applies powder (diameter typically 20 µm to 50 µm) from the supply chamber in a thin (20 µm to 60 µm) layer to a substrate, also called base plate in the build chamber. To form the part a laser (typically < 300 W but occasionally higher) melts a pattern in the powder. After the melting the substrate is lowered and re-coated, followed by a new laser track. This process is repeated step-by-step until the part is complete, whereafter the part is mechanically cut from the build plate. LPBF is very similar to *electron powder bed fusion* (EPBF), which works in a similar way but using an electron beam as a heat source. The powder and laser beam used in LPBF are smaller than the powder and electron beam in EPBF, allowing the production of finer details. EPBF can on the other hand process material faster and is suitable for larger parts.

2.2 The physics of Laser Powder Bed Fusion

This section contains a summary to the most important physics for LPBF. This includes heat transfer, momentum transfer, and the laser-material interaction. For a complete coverage of these topics the reader is referred to the standard textbooks on the topic mentioned above.

2.2.1 Heat transfer

The advective-diffusive equation for heat

Heat is transported by two mechanisms, conduction and advection. Conduction is analogous to diffusion in mass transfer and is described by Fourier's law:

$$\frac{\partial(\rho C_p T)}{\partial t} = \nabla \cdot k \nabla T \tag{2.1}$$

Where ρ denotes density, C_p specific heat capacity, T temperature, and k thermal conductivity. Advection[1] on the other hand is the heat which is transported by the movement of the material relative to the reference frame. This is given by the advection equation:

$$\frac{\partial(\rho C_p T)}{\partial t} = -\vec{u} \cdot \nabla T \tag{2.2}$$

where $\vec{u}$ is the velocity vector of the medium.

In the presence of conduction, advection, and some arbitrary heat source, S, the full convective-diffusive heat transfer equation is governing the system:

$$\frac{\partial(\rho C_p T)}{\partial t} = -\vec{u} \cdot \nabla \rho C_p T + \nabla \cdot k \nabla T + S \tag{2.3}$$

which in some specific cases can be solved for analytically. Of particular interest is the so called Rosenthal problem of a semi-infinite substrate with the top surface thermally isolated and heat supplied as a point source of power P and a surface absorptivity α fixed at the origin: $S = \delta(0,0,0)\alpha P$. The velocity, u_x, is in this problem the speed of the substrate moving in the x-direction, is in the reference frame of a stationary substrate equivalent to the speed of the heat source. With temperature independent physical properties the solution at steady-state, known as Rosenthal's equation, is given by [145]:

$$T_{\text{Rosenthal}}(x, y, z) = T_0 + \frac{\alpha P}{2\pi k} \frac{\exp -\frac{u_x}{2D}(\sqrt{r} + x)}{r} \tag{2.4}$$

where the thermal diffusivity is $D = \frac{k}{\rho C_p}$ and $r = \sqrt{x^2 + y^2}$ the radius at the surface. This solution is diverging at the origin and is not useful for finding the peak temperature of the melt pool and as most other useful analytical treatments ignores the liquid movement and latent heat of the phase transitions. Despite this it has been shown to yield reasonable agreement for the width and length of the melt pool [101].

Rosenthal's equation is the Green's function of equation 2.3. This means that the temperature field of any arbitrary distribution of the heat source, $f(\vec{r})$, can be found from [33]:

$$T_{\text{arbitrary}}(\vec{r}) = \int T_{\text{Rosenthal}}(\vec{r} - \vec{R}) f(\vec{R}) dR \tag{2.5}$$

which is in general not possible to express on closed form. From equation 2.5 it is also possible to approximate effects from fluid movement and phase transition by the addition of heat sources and sinks [107].

One way of simplifying differential equations is to write it on dimensionless form. For a case relevant for LPBF we consider a semi-infinite slab in steady-state irradiated by a Gaussian heat source moving with the speed u_x in the x-direction on the top surface. For this system the temperature of the system is, assuming temperature independent physical material properties, governed by the equation:

---

[1] Sometimes the term convection is used interchangeably.

$$0 = -u\rho C_p \frac{\partial T}{\partial x} + k\nabla^2 T \tag{2.6}$$

with the boundary conditions:

$$-k\frac{\partial(T)}{\partial z}|_{z=0} = \frac{P\alpha}{\pi a^2}\exp(-\frac{(x^2 - y^2)}{a^2}) \tag{2.7}$$

$$T_{r\to\infty} = T(t=0) = 0 \tag{2.8}$$

Doing the variable transformations:

$$(X, Y, Z) = (x/a, y/a, z/\sqrt{Da/u}) \tag{2.9}$$

$$\Theta = T/T_s \tag{2.10}$$

where the characteristic surface temperature is given by $T_S = T_M\frac{\Delta H}{h_s}$. The normalized enthalpy is given by $\frac{\Delta H}{h_s} = \frac{\alpha P 2^{3/4}}{h_s\sqrt{\pi D u a^3}}$, with $h_s = \rho T_M \bar{c_p} = \rho T_M(c_p + h_f/T_M)$, the enthalpy of melting, including the contribution from the latent heat of fusion (h_f). The temperatures are given relative to the initial temperature.

Using these relations we reach the following equation in dimensionless form [114]:

$$0 = -\frac{\partial\Theta}{\partial X} + \frac{1}{Pe}\nabla^2\Theta \tag{2.11}$$

with the boundary condition

$$-\frac{\partial(\Theta)}{\partial Z}|_{Z=0} = \exp\left(-(X^2 - Y^2)\right) \tag{2.12}$$

The Péclet number, $Pe = ua\rho C_p/k$, is a dimensionless quantity which relates the advective heat transport to the conductive heat transport.

One consequence of equation 2.11 is that the dimensionless temperature Θ is a function of the Péclet number only. This means that the melt pool dimensions (defined by the condition $T/T_M = 1$) will be a function of the normalized enthalpy and Péclet number only. The Péclet number determines the shape of the melt pool, whereas the normalized enthalpy scales the isotherms.

Another normalized scaling, useful at low scan speeds, is given by [114]:

$$(X, Y, Z) = (x/a, y/a, z/a) \tag{2.13}$$

$$\Theta = T/T_s' \tag{2.14}$$

Where the characteristic surface temperature is, instead of the expression above, given by $T'_s = \frac{\alpha P}{\pi \bar{c}_p D a}$. It can be shown that the melt pool dimensions at low Péclet numbers is determined only by the value of the modified normalized enthalp, B'y:

$$B' = \frac{\Delta H}{h_s} \times \sqrt{\frac{Pe}{\pi}} \tag{2.15}$$

an expression which is independent of the scanning speed.

Thermal conductivity

There are two primary mechanisms for the transfer of heat inside a condensed metallic phase, electronic heat transfer and phononic heat transfer. As electrons and phonons travel through the material they will encounter scattering points, which impedes the electronic/phononic motion. These scattering points can be of several different types:

- An electron interacting with another electron (e-e)
- An electron interacting with a phonon (e-p)
- A phonon interacting with another phonon (p-p)
- A phonon interacting with an electron (p-e)
- A phonon or an electron interacting with an impurity (e-i, p-i)
- A phonon or electron interacting with a grain boundary (e-g, p-g)

The the thermal resistivity, the inverse of the conductivity $R = \frac{1}{k}$, arising from each of these processes can be added according to Matthiessen's rule:

$$R = R_{\text{e-e}} + R_{\text{e-p}} + R_{\text{p-p}} + R_{\text{p-e}} + R_{\text{e-i}} + R_{\text{e-g}} + R_{\text{p-i}} + R_{\text{p-i}} \tag{2.16}$$

For metals the heat is primarily transported by electrons, with the electron-phonon and electron-impurity scattering being the dominant scattering mechanisms leading to a simpler equation:

$$R = R_{\text{e-p}} + R_{\text{e-i}} \tag{2.17}$$

The mechanims for electron scattering in thermal transport are the same as for electron transport due to electrical currents, leading to a relationship between the electrical (σ) and thermal conductivity called Wiedemann-Franz's law:

$$k = L\sigma T \tag{2.18}$$

The Lorenz number L has a theoretical value of $2.45 \times 10^{-8}\ \mathrm{W\Omega/K^2}$.

The electrical resistivity, $\eta = 1/\sigma$, due to impurity scattering, $\eta_{\text{e-i}}$, for exampe from an alloying constituent, c_i, is largely temperature independent. The impurity concentration behaviour is governed by Nordheim's law:

$$\eta_{\text{e-i}} = C_N c_i (1 - c_i) \tag{2.19}$$

The Nordheim coeficcient ,C_N, is dependent on the impurity.

The electron-phonon contribution to electrical resistivity on the other hand has a strong temperature dependence. According to the Debye model it is given by [135]:

$$\eta_{\text{e-p}} = \kappa T^5 \int_0^{T_D/T} \frac{z^4}{e^z - 1} dz \tag{2.20}$$

where κ is a proportionality constant, and T_D the Debye temperature. Above the Debye temperature, which for copper is around 300 K [68], this expression becomes linear.

Combining the electrical resisitivity from equation 2.19 and 2.20 with Matthiesen's rule (which is also valid for electrical resistivity) and Wiedeman-Franz's law thus gives the temperature dependence of thermal conductivity, which is generally expected to decrease with increasing temperature. It can further be seen that the temperature dependence becomes weaker the more dominant impurity scattering is.

2.2.2 Momentum transfer

The liquid and gaseous phases are free to move. The movement is described by the momentum equation, which is Newton's second law expressed in differential form. If the fluid is incompressible, which it will be in all cases considered in this thesis, the momentum equation is given by:

$$\frac{\partial \rho \vec{u}}{\partial t} + \nabla \cdot (\rho \vec{u} \vec{u}) = \nabla \cdot \mu \nabla \vec{u} + \nabla + \rho \vec{g} + \vec{S} \tag{2.21}$$

$\vec{u}$ is the fluid velocity, μ the viscosity of the fluid, p the pressure, $\vec{g}$ the gravity, and $\vec{S}$ any external force acting on the fluid. The flow is furthermore constrained by the continuity equation, equivalent to conservation of mass. For an incompressible fluid it is given by:

$$\nabla \cdot \vec{u} = 0 \tag{2.22}$$

An important contribution to the momentum source term in LPBF conditions is the surface tension:

$$\vec{S}_{\text{surface tension}} = \delta(r \in \text{surface}) \left(\vec{S}_{\parallel} + \vec{S}_{\perp} \right) \tag{2.23}$$

Where the surface normal term is given by:

$$\vec{S}_{\perp} = \sigma \kappa \vec{n} \tag{2.24}$$

and the tangential term:

$$\vec{S}_{\parallel} = \frac{\partial \sigma}{\partial T} (\nabla T - \vec{n}(\vec{n} \cdot \nabla T)) \tag{2.25}$$

where $\vec{n}$ the surface normal direction, $\kappa = -\nabla \cdot \vec{n}$ the surface curvature, and σ the surface tension. The tangential copmponent gives rise to so called Marangoni flow, due to the temperature dependence of the surface tension. Marangoni flow is usually directed from a hot area to a cold area due to the typical decrease of surface tension with increasing temperature [82, 30]. The presence of surface active elements, like sulfur or oxygen, can in some cases reverse the sign [30] leading to a flow towards the warm area [130].

At high temperatures another important source term is the recoil pressure from evaporation of liquid [120]. This force is responsible for the formation of so called keyholes, an effect which has profound impact on the shape and behavior of the melt pool (discussed further in section 2.3.1). This pressure can be calculated from the Clausius-Clapeyron equation [81] to be:

$$\vec{S}_R = -0.54 P_0 \exp \frac{L_{\mathrm{vap}} M (T - T_{\mathrm{B}})}{R T T_{\mathrm{B}}} \vec{n} \delta (r \in \mathrm{surface}) \tag{2.26}$$

where P_0 is the atmospheric pressure, L_{vap} latent heat of vaporization, M molar mass, T_{B} the boiling temperature, R the universal gas constant, ρ_{g} the gas phase density, and ρ_{m} the metal density.

2.2.3 Laser-material interaction

The term laser, short for *light amplification by stimulated emisson*, refers to a light source which creates a collimated and coherent beam. What distinguishes a laser from other sources of light is primarily the high coherence and narrow frequency range. The high coherence allows the beam to be focused very narrowly, achieving very high power densities.

Most lasers have beam with a Gaussian intensity profile, which in the ideal case is given at in radial coordinates by:

$$I(r) = I_0^{1/e} \exp\left(-\frac{r^2}{\omega_{1/e}^2}\right) \tag{2.27}$$

or equivalently

$$I(r) = I_0^{1/e^2} \exp\left(-2\frac{r^2}{\omega_{1/e^2}^2}\right) \tag{2.28}$$

with total power of such a beam given by:

$$P = \pi \omega_{1/e}^2 I_0^{1/e} \tag{2.29}$$

and

$$P = 2\pi \omega_{1/e^2}^2 I_0^{1/e^2} \tag{2.30}$$

In the first case the $1/e$-beam waist ($\omega_{1/e}$) is used, which is the radius within 63 % of the energy is delivered, and in the second case the $1/e^2$-beam waist ($\omega_{1/e^2} = \sqrt{2}\omega_{1/e}$) is the radius where 86 % is delivered, as shown in figure 2.3 a). From this point on the laser radius will be given by the $1/e^2$ radius: $r_l = \omega_{1/e^2}$.

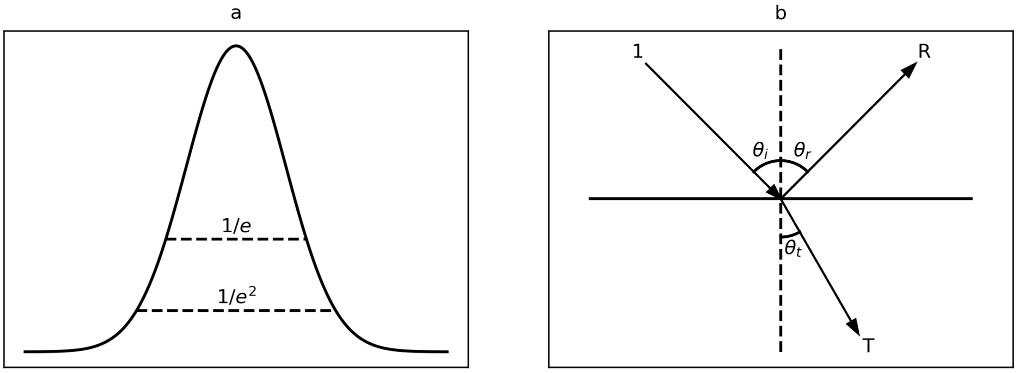

Figure 2.3 – (a) Gaussian beam profile with the $1/e$ and $1/e^2$ radii marked. (b) Reflection and transmission of a laser beam on a surface, $\theta_i = \theta_r$.

As a laser beam hits a surface a part of the light will be transmitted (T), a part will be absorbed A, and a part will be reflected R. These fractions sum to unity:

$$1 = T + A + R \tag{2.31}$$

For metals the transmitted fraction can be neglected, except for thin films on the nanometer scale, leading to the expression:

$$1 = A + R \tag{2.32}$$

The direction of the reflected light is given by the law of reflection, stating that the angle of incidence, θ_i is equal to the angle of reflection, θ_r, which on vector form is given by:

$$\vec{d}_r = 2(\vec{d}_n \cdot \vec{d}_i)\vec{d}_n - \vec{d}_i \tag{2.33}$$

where $\vec{d}_r$, $\vec{d}_n$, and $\vec{d}_i$ is the vector of reflection, surface normal vector, and vector of incidence respectively.

The room temperature reflectivity of copper is shown in figure 2.4 a. In the violet (400 nm) to green(550 nm) range of the visible spectrum the metal is absorbing, giving rise to the characteristic red color. In in the IR-parts of the spectrum the reflectivity is very high, above 99 % at the wavelength of Nd:YAG lasers (1064 nm) commonly used for LPBF-processing. This value is given for a polished pure plate, the reflectivity is in many realistic situatuations decreased by the presence of copper oxides on the surface.

The reflectivity depends on the complex dielectric constant of the material, ε according to the

Fresnel equations, for s-polarized, and p-polarized light respectively:

$$R_S = \left|\frac{\cos\theta_i - \sqrt{\epsilon - \sin^2\theta_i}}{\cos\theta_i + \sqrt{\epsilon - \sin^2\theta_i}}\right|^2 \tag{2.34}$$

$$R_P = \left|\frac{\epsilon\cos\theta_i + \sqrt{\epsilon - \sin^2\theta_i}}{\epsilon\cos\theta_i + \sqrt{\epsilon - \sin^2\theta_i}}\right|^2 \tag{2.35}$$

where θ_i is the angle between the normal plane and the incident ray.

For metals at wavelengths where interband absorption is negligible the dielectric constant is to a good approximation described by the Drude model [20]:

$$\varepsilon = \left(1 - \frac{n_{\text{eff}}e^2\tau^2}{\varepsilon_0 m_e(1+\omega^2\tau^2)}\right) + i\left(\frac{n_{\text{eff}}e^2\tau}{\varepsilon_0 m_e\omega(1+\omega^2\tau^2)}\right) = \left(1 - \frac{\omega_p^2}{(\omega^2+\omega_c^2)}\right) + i\left(\frac{\omega_p^2\omega_c}{\omega(\omega^2+\omega_c^2)}\right) \tag{2.36}$$

where τ is a relaxation time for electron collisions, m_e the electron mass, ε_0 the vacuum permittivity, n carrier density, ω the frequency of the light, e the electron charge, and ω_c the electron collision frequency.

The relaxation time is the average time between electron scattering (the same mechanisms as for thermal and electrical resisitivity), and is temperature dependent. Several models have been developed for calculating the value of τ: One method, used for example by Comins [20], is to calculate the value from the electrical DC-conductivity: $\sigma = ne^2\tau/m_e$. Another method, used by Ujihara [135] is to use the room temperature optical constant to fit the pre-factor, κ', in the Drude electron-phonon interaction term, $\omega_c = \kappa' T^5 \int_0^{T_D/T} \frac{z^4}{e^z-1}dz$, and from this calculate the temperature dependence. A third option is to evaluate the pre-factor directly, something which has been done by for example Siegel [125].

For the case of pure copper the predictions of these models for 1064 nm light is shown in figure 2.4 b). The resistivities for Comins' model are evaluated from resistivity data for both liquid and solid[2]. The Ujihara model is shown using the original data, but since the value used for the room temperature reference disagrees with the correct room temperature values, the model calculated from more recent values of the room temperature dielectric constant of copper is also shown[3] The values for Siegel's model is shown as published. Comin's model agrees well with Ujihara's model, if modern data is used for calculating the model parameters. Unfortunately there is a lack of modern high temperature reflectivity data for copper which could be used for verification of the models, but experiments using fluencies on the same order of magnitude as encountered in LPBF show values around 60 %[148], significantly higher than other reported values. The low reflectivity in these experiments have been attributed to surface deformation, plasma formation, and nonlinear optical processes [139].

---

[2] See chapter 3 and table 7.1 in chapter 7 for further details.

[3] Fitted to the room temperature values of Babar [3], yielding the model parameters $\kappa' = 93.3\,\text{Hz/K}^5$, $\omega_p = 1.26 \times 10^{16}\,\text{Hz}$, and $T_D = 310\,\text{K}$.

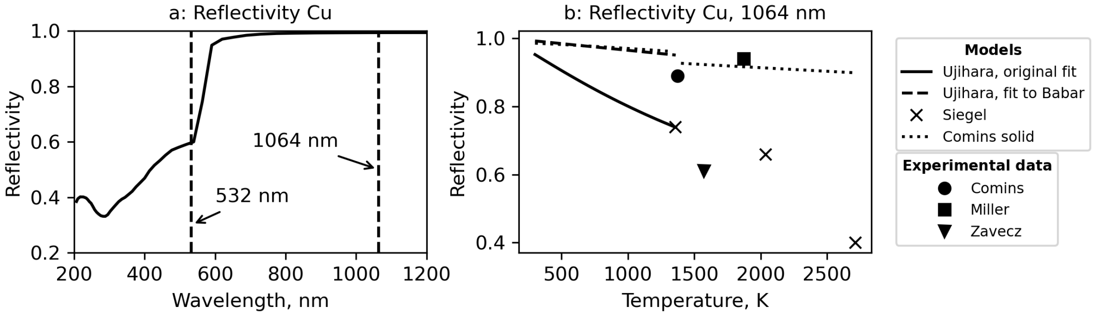

Figure 2.4 – The reflectivity at normal incidence for copper. (a) The spectrum calculated from the dielectric function given by Babar [3] with the wavelengths 532 nm (green) and 1064 nm (IR) marked. (b) Temperature dependence of the reflectivity according to different models and experimental data: Ujihara [135],Comins [20], Siegel [125], Miller [100], and Zavecz [148].

The Drude model is only valid for absorption through free electrons. The absorptivity of copper in the visible range has a large contribution from interband transitions, giving rise to its characteristic color. These absorptions are only weakly dependent on temperature and also more well studied than the IR-spectrum. Of particular interest for this thesis is the absorptivity of green light at the wavelength 532 nm, which have reported values of the perpendicular absorbtivity in the range 25 % to 45 % [110, 60, 20, 3].

2.3 Defects in Laser Powder Bed Fusion

During LPBF processing there are many possible defects which can occur, including pores, cracks, warping, and various types of surface defects. Of these defects there are many different sub-types which often have different origins and mechanisms. In many cases changing parameters to minimize one type of defect will lead to a higher amount of another type. Understanding the influence of the different processes and materials parameters is therefore key to finding defect free process regions, which is needed for reliably producing usable parts.

2.3.1 Porosity

The formation of pores is a common and highly undesirable defect in LPBF-processing, leading to drastically worsened mechanical properties [17]. Different types of pores have different origins, and thus require different strategies to be removed or mitigated. Within this work pores linked to the melting mode of the melt track are of high relevance. These melting modes, illustrated in figure 2.5, are *balling mode*, *conduction mode*, and *keyhole mode*. The pores typically encountered in these modes are correspondingly called *balling pores*, *lack-of-fusion pores*, and *keyhole pores* respectively. Sometimes balling and lack-of-fusion pores are lumped together in the same category as they both occur at low power processing conditions. As will be shown in chapter 5 there are fundamental differences between the pore formation in

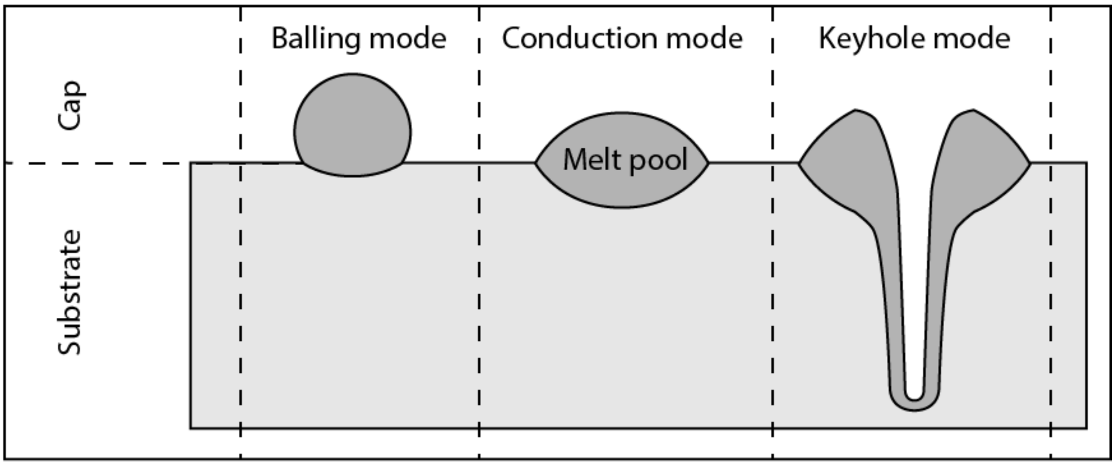

Figure 2.5 – The melting modes of LPBF; Balling mode defined by a contact angle >90°, conduction mode defined by a contact angle <90°, and keyhole mode defined by the formation of a depression in the melt center. The names of the different parts of the melt track; the cap, substrate, and melt pool are marked as well.

conduction mode and balling mode, and therefore the distinction between lack-of-fusion and balling pores is maintained in this work.

In balling mode the cap is not wetting the substrate, leading to ball-like features forming on the top of the substrate, with so called *balling pores* in between them [40]. Mechanisms proposed for the formation of these include oxidation preventing the wetting [84], hydrodynamic instabilities [146], and a too short interaction time for the liquid to spread [69]. These mechanisms are correct in some situations, but are unlikely the reason in the processing of copper. Oxidation does occur in copper, but the oxides dissolve just above the melting point of copper making the oxides unlikely to survive the very high surface temperatures achieved during LPBF. Balling defects can furthermore be seen in processing of the chemically and physically similar metal gold [67] where the oxides dissociate at 160 °C. Hydrodynamic instabilities require a very elongated melt to be able to form [146], which is not the case in the typically chosen low Péclet number processing parameters of the group 11 metals and their alloys. It has further been shown that the amount of porosity forming is only weakly influenced by the scanning speed of the laser [95], excluding the time needed to spread the liquid as a key factor in the formation of balling pores. It has been shown that balling pores are correlated to a low depth to length ratio of the melt pool [101], but the exact mechanism is so far relatively unstudied.

In conduction mode, the generally desired mode for LPBF processing, the cap is wetting the substrate. The pores forming in this situation are typically named, after the welding term [13], *lack-of-fusion porosities.* The pores have been shown to be well predicted by the gaps forming in-between the melt tracks [132]. Thus, these pores can be reduced by tuning process parameters like hatch distance, layer thickness, and scanning strategy. Often good process conditions are found by operating close to the threshold to keyhole mode [36]. Examples of balling and lack-of-fusion porosity are shown in figure 2.6.

At high power the temperature of the melt becomes close to boiling and the recoil pressure from the melt pool is enough to form a depression in the melt [16]. This depression increases the absorptivity of the melt as the reflected laser light gets directed into the depression itself [16, 152, 80]. The positive feedback between the depth of the depression and absorptivity causes the depth of the melt to rapidly increase, forming a deep and unstable tube, called a keyhole, into the substrate. This mode of melting is called keyhole mode. The tube is inherently unstable and will collapse if it is deep enough, entrapping gas inside and form a pore [152].

To avoid the pores mentioned above one typically tries to find a processing region where neither keyhole pores nor low-power porosity occur. This in many cases requires an experimental parameter sweep. Such a sweep can be made simpler by dimensionless scaling, which has been proven useful for transferring parameters from one material to another [36]. Such approaches, however, entail large simplifications of reality and are limited in that pore formation, to some degree, is stochastic. Because of this, in-situ process monitoring combined with machine learning has emerged as an interesting approach to detect the formation of defects [123].

Other types of pores include *evaporation pores*, which occur when a volatile compound in the alloy evaporates, forming bubbles which get frozen in as the melt pool solidifies. A similar situation occurs when pores are present in the feedstock powder. These pores, called *gas porosities* might not have enough bouyancy to escape before solidification, making them difficult to remove during processing.

It is possible to reduce porosity after manufacture of parts by *hot isostatic pressing* (HIP). This is achieved by placing the manufactured part under high pressure at elevated temperature. The high pressure causes the pores to close, leading to a near complete removal of porosity [96]. Pores which are close to the surface have however been shown to be difficult to remove, and the pores can after further heat treatment open themselves [29].

2.3.2 Cracks

Several different mechanisms are responsible for the formation of cracks in LPBF, but in general the mechanisms are the same, or similar, to cracks occurring in welding. Of particular interest are *solidification cracking* and *hot cracking*, occurring due to segregation of solute or impurities as the molten material solidifies, leading to depression of the melting point and decrease of ductility of the solidified material [13]. Solidification cracking occurs when the concentrated liquid, with depressed melting point, gets trapped between solidified material pulling the liquid apart due to thermal strain from the cooling of the material [38]. Hot cracking on the other hand occurs when the ductility of the concentrated and re-solidified material is depressed so much that it cannot resist the strain from the thermal stresses [13].

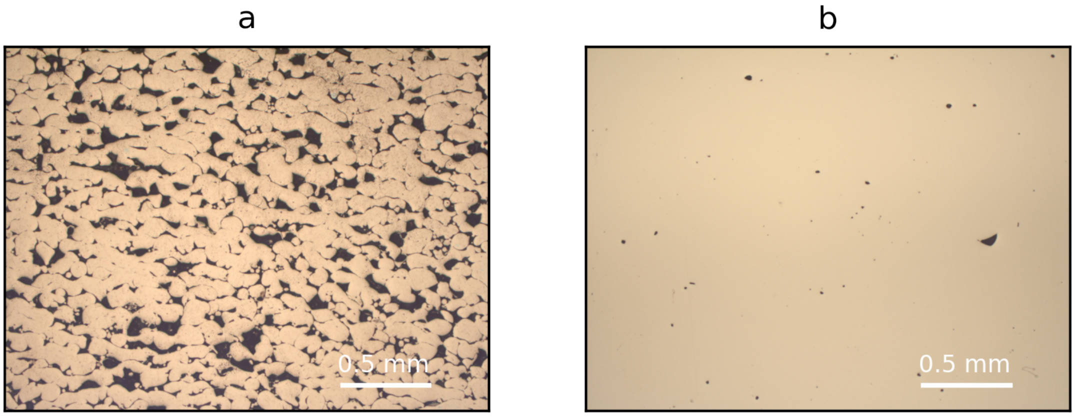

Figure 2.6 – Two pore types of high relevance for this thesis: (a) Balling porosity, and (b) Lack-of-Fusion porosity

Experimentally determining which of these mechanisms occur can be challenging, where solidification cracking can typically be distinguished by the formation of dendritic structures on the crack surface [140].

These types of cracks are seen in many different types of materials: Nickel based superalloys [42, 18, 38], stainless steels [122], aluminum alloys [89, 44, 64], gold alloys [71], amongst others. Reduction of such cracks can be done by reducing the presence of segregating elements [42, 38], or by increasing them enough to allow backfilling [140]. Reduction of cracks can also be achieved by changing processing parameters to minimize the thermal stresses which occur during processing. Examples of this include pre-heating the base-plate [44], changing the shape of the laser beam [18], or wobbling the laser [64]. One interesting approach is to relieve stress with laser-peening which if it is applied in-situ can not only prevent, but also heal, cracks [63]. Cracks can also, like pores, be removed by post-treatments like HIPing [153].

Segregation can also occur in the heat affected zone, for example by impuritities that locally lower the melting point, or by solid state diffusion. This can lead to reduced ductility or the formation of brittle intermetallics, which when leading to cracks are refered to as *liquation cracking* [13]. Brittle intermetallics can also form when processing multi-material parts [151, 22], typcially at the interface between the different materials. Multi-material processing is currently not very common with LPBF, but is often used in DMD processing.

2.3.3 Other defects

Other defects which can occur during LPBF processing include warping, formation of slags, and surface irregularities. *Warping* is the bending of a part due to residual stresses. Due to the layered approach of LPBF this typically causes compressive stresses on the upper portion of the part, and tensile stress in the bottom, sometimes large enough to break the support structures [91]. To reduce the stresses one can segment the part into shorter lines [91], or in other ways modifying the laser scan pattern [59]. Residual stresses can also be reduced by heat treatments. Heat treatments can for example be done in situ by heating the baseplate [98, 10] or by re-scanning with the laser [98]. Generally better results are achieved with the former method as it counteracts the top-down heat input of the process [98]. Post processing is another option which can significantly reduce residual stresses. Options include thermal treatment [154] or shot-peening [136].

In some materials prone to oxidation *slags* can form during the processing, leading to poor mechanical properties. The slags often form as a result of spatter ejection [35], and can lead to lack-of-fusion-like porosity [131]. The formation of slag can be controlled by reducing the amount of oxygen, but also through control of scanning speed and power [131, 23].

Surface irregularities are inherent in LPBF processing, most typically by the adhesion of satellite powder particles on the surfaces of the part [24]. These satellites significantly worsen the mechanical properties but can be removed by machining or sand blasting [115]. The surface quality of the upper surfaces can be improved by remelting of the top layer [147]. This is difficult to do on inclined surfaces, but techniques have been developed to use pulsed lasers to remove powder from these surfaces, allowing remelting to be done [99].

2.4 Laser powder bed fusion of group 11 metals and alloys

The group 11 metals, copper, silver, and gold, have properties which are chemically and physically similar to each other: high thermal and electrical conductivity, low hardness, and good corrosion resistance. Despite this there is a large difference in price, with copper at the time of writing costing $8\,\mathrm{CHF\,kg^{-1}}$, silver $800\,\mathrm{CHF\,kg^{-1}}$, and gold $54\,000\,\mathrm{CHF\,kg^{-1}}$. This price difference naturally influences which types of parts are considered for LPBF production with the different metals. For gold and silver the target applications are typically luxury items like jewellry and high end watches, whereas copper is used in more everyday and industrial items. This has also influenced the research on LPBF of these metals. For gold much focus has been on properties like: high surface quality [58, 157, 71] and color fidelity [70, 155] whereas the study of copper has focused on processability [112, 149, 134]. LPBF of silver has been significantly less studied than the gold and copper, but tends to focus on similar issues as gold alloys [157, 32].

2.4.1 Laser powder bed fusion of gold, silver, and their alloys

The first directly printed precious metal pieces were produced in the early 2000s when Towe Norlén used a selective laser sintering device optimized for steel to produce gold jewelry [106]. The process was patented in 2003 [61] and although the process got much attention on several different industry conferences, the topic was not explored much further at the time. In 2010, two studies reporting LPBF processing of gold were published. Khan and Dickens [67] studied melt tracks in 24K gold, varying the scanning speed and power of the laser beam. They found a narrow processing window where the melt remained stable and continuous. Using the parameters that yielded a stable melt track they built cubes which where tested for porosity. The porosity was at best 10 vol.% with pores occurring between the layers of the build. The surface exhibits a high roughness which although not quantified was clearly pronounced. In the other study Jhabvala et al. [57] processed the 18K 3N gold alloy[4] using different scanning strategies. They found cracks occurring at the edges of the built parts, especially pronounced when using a parallel scanning strategy[5]. These cracks were attributed to overheating on the edges in combination with high thermal gradients orthogonal to the scanning direction. Similar overheating issues caused large porosities in the center of the part when using a spiral scanning strategy[6], showing that for decreasing the amount of defects it is of high importance to control the spatial and temporal energy input. The parts exhibit porosities which were not quantified. It is worth pointing out that even if the porosity is quantified one cannot necessarily compare different studies, since the sample preparation method can make a big difference in the result. This is due to the softness of gold, which means that smearing during polishing can completely cover porosities [70].

After these pioneering studies several aspects of AM of gold and other precious metals have been studied. Much of this research has been focused on reducing the porosity of the builds. One of the early studies showed that increasing the power and lowering the scanning speed decreased the porosity [32] and another study showed that porosity could be decreased by including powder fractions less than 5 microns in diameter in the feedstock powder, or by employing re-scanning techniques [157].

In 2012 it was reported that alloying 925 silver with small amounts of undisclosed elements could drastically decrease porosity in LPBF-parts [32]. Alloying with 2% gallium in 18K gold was tried soon thereafter by Zito et al. [157], which increased the porosity, surface roughness and amount of cracks in the parts, as compared to the 18K alloy. In the following year Zito et. al. presented studies where they built parts using 18K gold alloyed with small amounts of p shell elements: silicon, germanium and boron [156]. A clear decrease of porosity and surface roughness was observed, especially for the Ge-doped alloy. This improvement was speculated to arise from decreased thermal conductivity, and/or the formation of thin oxide layers on the surface of the powders.

Further studies on alloying 18K gold was performed by Klotz et al.. Their focus was on alloys which form high thermal resisitivity solid solutions with gold with small additions of alloying elements [70, 71]. After screening bulk materials prepared by induction melting the most promising candidates Au-13Cu-11.3Ag-0.7Fe and Au-12.8Cu-11.8Ag-0.4Ge were synthesized using gas atomization. Visibly both alloys only had a minor color difference to 3N-gold. Furthermore the porosity was, in combination with a slight oxidation of the feedstock powder, reduced considerably for these alloys: from 3 % for 3N-gold to 0.45 % and 0.1 % respectively. Cracks were found in both alloys: aligned horizontally for the Fe-containing alloy and vertically for the Ge-containing alloy. The latter alloy seems to crack due to solidification cracking along the vertically elongated grains. This elongation, which has been previously noted in several other materials processed by AM, arise from the remelting of the layers which allows epitaxial growth on top of the underlying grains [71]. The cause of the horizontal cracks in the Fe-containing alloy were not fully determined. It is likely that they come from thermal stress, but no explanation to why this was more pronounced for the Ge-containing alloy is given.

---

[4] By weight 75% Au, 12.5% Ag and 12.5% Cu

[5] Scans running alternating left and right covering the whole part

[6] Scans running from the outside to the inside of the build layer in a spiraling fashion

2.4.2 Laser powder bed fusion of copper and copper alloys

LPBF of copper was reported in 2003 by Pogson, Fox, Sutcliffe and O'Neill [112], who performed a parameter study of power, scan speed, pulse frequency and beam overlap. Even though the study was thorough the built parts were suffering from porosities and more complicated parts proved difficult to process. The authors discussed the possibility of using green lasers to improve the process, but no such attempts were published. More recent much focus has been put on decreasing porosity by operating at much higher power, and dense parts have been shown to be achievable operating at around 1 kW of laser power [54, 52, 126, 92]. Operating at this power has, however, been shown to lead to large wear on the optical components [54].

A lower level of porosity can also be achieved by alloying, which both decrease thermal conductivity and increase thermal conductivity. Alloy systems which have been processed by LPBF include precipitation hardening alloys like CuNiSi[133] and chromium based alloys [134, 149]. These alloys retain a high thermal conductivity, making them interesting for many applications, this however at the same time makes them more prone to porosity formation than for example alloys in solid solution. Another alloy class which has been under investigation are bronzes. Copper-tin bronzes have been studied at several compositions, ranging from 4 wt.% to 15 wt.% [95, 119, 94, 32]. CuSnTi-diamond composites have also been investigated, where crack free and dense process conditions could be found [85]. Even though these studies are to a large degree focused on the microstructure it is clear that it is easier to achieve dense parts with increasing alloying.

Lately much interest has been shown in decreasing the porosity by increasing the optical absorptivity of the process. Such attempts have included oxidation of the feedstock powder [54], blending with nanoparticles, and coating of the feedstock powder with metallic coatings[7] [55]. From these studies it is clear that this is beneficial for the processing, but the mechanism has not been explained, especially regarding the relative influence of the alloying component with respect to the absorptivity increase. The scientific literature on processing with a green laser source is as of now lacking, even though commercial LPBF machines equipped with one are available on the market. Some laser welding studies show that the combination of green and IR-lasers can stabilize the weld process [45, 31, 129].

---

[7] Independently of the work published in chapter 6 and the corresponding article [88]

The use of ultra-short pulsed lasers for LPBF has been tested with the motivation of being able to reach extremely high surface temperatures [62]. No clear benefit could, however, be found by this approach, and the surface is very rough. Furthermore the powders seem to be sintered rather than fused by melting, which is consistent with the very low power of 20 W, one to two orders of magnitude lower than the typically needed value.

2.5 Simulation and modeling of LPBF processes

Due to the complexity and wide range of length scales of the physics involved in LPBF there is not one single technique which is appropriate for simulating the whole process. The methods used are typically characterized as micro-scale (on the order of micrometer and below), meso-scale (up to millimeters in size) and macro-scale (anything larger).

2.5.1 Micro-scale modeling

On the micro-scale one is often interested in the formation of different phases and microstructures, which strongly influence the mechanical properties of LPBF parts. Much understanding of the phases formed can be gained by studying the phase diagram of the material in question, but the high cooling rates can give rise to metastable species. These metastable phases can to some degree be predicted by combining the one-dimensional Scheil-Gulliver equation with CALPHAD tools, but the assumptions of the model (one-dimensionality, no solid diffusion in the solid, perfect mixing of the liquid and equilibrium at the interface) are not always fulfilled. Furthermore this gives no information on the microstructure shape and texture.

Several numerical methods exist to solve more generalized situations, the most important ones being *the phase field model* and *cellular automata* [73]. The phase field model is based on an order parameter, ϕ, which represents the phase fraction of the phase of interest. Given an expression for the free energy, $F(\phi)$ one can the calculate the evolution of the phase field from the Allen-Cahn equation[8]:

$$\frac{\partial \phi}{\partial t} = \mathfrak{M} \frac{\partial F}{\partial \phi} \tag{2.37}$$

with $\mathfrak{M}$ being a mobility constant. This approach is particularly useful for simulating features on the size-order of dendrites, but for the simulation of larger features the cellular automata method is generally preferred [73]. In the cellular automata method the domain is divided into cells, which develop in time depending on the state of the cell and its neighbors. For simulation of AM one typically takes the local undercooling into account, typically via a polynomial to predict the solidification velocity. This is applied to an envelope describing the modeled crystals which is is allowed to develop with time [72].

---

[8] Somewhat simplified, ignoring concentration and temperature fields. For a full explanation see for example the review article by Korner et al. [73]

2.5.2 Meso-scale modeling

On the meso-scale one is often interested in predicting the temperature and shape of the melt pool, either for using as an input for micro and macro-scale simulations, understanding the formation of varoius defects, or to find good parameters for processing. There are many different techniques with different computational costs and precision available. On the simplest level we have purely analytical methods, where typically simplified cases of the advective-conductive heat equation (equation 2.6) like the Rosenthal solution [4] or more complex functions [101] are considered. Other methods include the use of scaling relations derived from 2.3, like for example normalized enthalpy, to predict properties [114] and to transfer parameters to different materials [36]. This approach has been shown, despite neglecting much of the physics, to have good agreement with experiment, and can often be used as a first approximation for explaining secondary effects, predicting widths of melt tracks, or in combination with geometrical models for the melt pool shape to predict porosity level [132]. The downside of such approaches is that for example the powder is treated with effective parameters for the physical properties, which often means that parameters need to be fitted to experiments.

Slightly more complex is the numerical solution of the advective-conductive heat equation (2.3), which allows more complex and general situations (latent heat, temperature dependence of physical parameters, arbitrary heat sources, etc.) to be treated [36]. Here one neglects the flow of liquid, and the powder is typically also treated as an effective medium. The thermal fields can be used to calculate residual stresses [86], which is useful for prediction of defects like warping and cracks. Typically the partial differential equations are solved using the finite element method (FEM), which excels for solving linear differential equations, and lead to low computational costs. A thorough discussion of FEM is out of scope for this short summary, but is discussed in standard text books like *Finite Elements: Theory, Fast Solvers, and Applications in Solid Mechanics* by Braess [8].

A combined numerical solution of the equations of fluid flow (eq. 2.21 and eq. 2.22), together with the advective-conductive heat equation and Maxwells equations, allows the treatment of all aspects of the LPBF process, but is generally very computationally costly due to the nonlinear momentum equation. In principle one can use most differential equation solving methods for solving these equations: the finite difference method (FDM), FEM [15], or the finite volume method (FVM). Typically however one uses FVM as it guarantuees the conservation of mass, is simple to implement, and is good at handling non-linear equations.

In the last years an alternative method called Smooth Particle Hydrodynamics (SPH) has been developed for simulations of LPBF [141, 34]. This method works by mapping the differential system on a domain with discrete particles, allowing efficient calculation in parallel both on CPUs and GPUs [1]. The method is not yet widely used in the LPBF-community, but the high resolution and computational effort will likely lead to it being used more important in the future.

Of particular interest has been the simulation of keyhole mode, both for welding [16] and LPBF [41, 66, 80], which is very well represented by FVM simulations. Conduction mode has also been studied, particularly for welding [130], but is for LPBF a bit more complicated to study as the powder-melt interaction becomes increasingly influential. One approach to get a realistic treatment of the powder to is the Discrete Element Method [83].

The finite volume method for multi-phase flows

FVM, which is used extensively in this thesis, is a so called integral scheme for solving partial differential equations (PDE). Here it is explained in a somewhat simplified way, as a complete coverage would be out of scope for the thesis, for further details the reader is referred to standard textbooks on the topic. The basic premise of the method is that the differential equation is put on integral form, integrated over a control volume and discretized.

How this is done is exemplified below for a steady-state 1D diffusion system with an arbitrary source term:

$$S(x) = \frac{\partial}{\partial x} k \frac{\partial}{\partial x} T \tag{2.38}$$

which integrated over a control volume, $\Omega \in (x_i - \Delta x/2, x_i + \Delta x/2) = (x_w, x_e)$, becomes:

$$\int_\Omega dx\, S(x) = \int_\Omega dx \frac{\partial}{\partial x} k \frac{\partial}{\partial x} T \tag{2.39}$$

which according to Gauss' theorem can be written in terms of the fluxes over the control volume surfaces:

$$\bar{S}\Delta x = \left(k \frac{\partial T}{\partial x}\right)_e - \left(k \frac{\partial T}{\partial x}\right)_w \tag{2.40}$$

This equation can now be discretized by a suitable discretization scheme. One simple way is by averaging the value of the diffusion coefficient and using central differences ($p = x$, $w = x - \Delta X$ and $w = x + \Delta X$):

$$0 = S_p + \left(\frac{k_p + k_e}{2} \frac{T_e - T_p}{2\Delta X}\right) - \left(\frac{k_w + k_p}{2} \frac{T_p - T_w}{2\Delta X}\right) \tag{2.41}$$

which can be rearranged as the linear equation:

$$a_{i,p} T_{i,p} = a_{i,w} T_{i,w} + a_{i,e} T_{i,e} + S_{i,p} \tag{2.42}$$

which over the whole solution domain becomes the linear equation system for every cell i:

$$\begin{bmatrix} a_{1,p} & a_{1,e} & 0 & \dots & 0 \\ a_{2,w} & a_{2,p} & a_{2,e} & \dots & 0 \\ \dots & \dots & \dots & \dots & \dots \\ 0 & 0 & 0 & \dots & a_{n,p} \end{bmatrix} \begin{bmatrix} T_1 \\ T_2 \\ \dots \\ T_n \end{bmatrix} = \begin{bmatrix} S_1 \\ S_2 \\ \dots \\ S_n \end{bmatrix} \tag{2.43}$$

For more complex equations the same process is performed on all terms of the differential equation, often using more complicated discretization schemes, leading to a diffrent linear system. Slighly more complicated is the solution of the momentum equation, where the pressure is general not known. To calculate the pressure one use the continuity equation as a constraint, iteratively updating the pressure terms until it is fulfilled. There are several algorithms for this, most popular being the SIMPLE, PISO, and PIMPLE [108] algorithms.

There are several approaches for treating multiphase flows. Of particular interest for LPBF is the volume of fluid (VOF) method [46], where the metal and shielding gas are treated as a phase fraction, $\phi = \phi_{\text{metal}} = 1 - \phi_{\text{gas}}$. This phase fraction is evolved as a passive scalar:

$$\frac{\partial \phi}{\partial t} = -\vec{u} \cdot \nabla T \tag{2.44}$$

The physical properties are then updated as a funtion of ϕ. From ϕ important surface properties like the surface normal, $\vec{n} = \frac{\nabla\phi}{|\nabla\phi|}$, and the curvature, $\kappa = -\nabla \cdot \vec{n}$, can be calculated.

In the VOF method all forces are treated as volumetric sources. This is done by replacing the delta function in the surface forces: $\delta(\vec{r} \in \text{surface}) = |\nabla \cdot \phi|$. If one phase is significantly heavier (the metal) than the other (the shielding gas) this however introduces spurious flow in the lighter (gas) phase, and the following identity is used to smear the forces to the heavier phase [7]:

$$\delta(\vec{r} \in \text{surface}) = |\nabla \cdot \phi| \frac{2\rho}{\rho_M + \rho_G} \tag{2.45}$$

ρ_M and ρ_G are the metal and gas densities respectively.

2.5.3 Macro-scale modeling

Simulating distortion and residual stresses in complete parts requires the whole geometry to be modeled , including the complex heat transfer and non-linear mechanical deformation [86]. Solving this problem directly is computationally costly due to the long process times and fine detail needed to be resolved [26, 86]. To make the problem more computationally manageable there are two main paths taken [121]: Improving the computational efficiency through for example dynamic mesh refinement [111] and through the application of physical approximations. One such physical approximation which has proven very useful is the inherent strain method, which allows the thermo-mechanical deformation to be reduced to an elastic-linear problem [121] with stresses imposed by meso-scale thermo-mechanical models [86] or evaluated from experiment [121].

2.6 Aim of thesis

Several approaches have been proven successful in reducing balling and lack-of-fusion defects in LPBF of copper and similar metals and alloys. These approaches include alloying, where the effect is typically ascribed to the decreased thermal conductivity, increasing the power or increasing absorptivity of the melt pool or powder. However, the relative impact of these approaches have not been fully understood, which makes it difficult to choose the right strategy for decreasing porosity in different situations.

Furthermore the mechanisms that occur during balling and close to the threshold between balling and conduction mode are not very well studied, and several important questions remain open. These questions include to which degree the laser light is illuminating the solid material, and how far this illumination is contributing to the energy balance of the melt pool, especially in highly reflective metals like copper, where the temperature and phase dependence strongly influence the total absorptivity. It is also not well understood how the shape of the melt pool, and the coagulation mechanism of the powder influence the absorptivity of the system. These questions are very important for developing effective pore mitigation strategies, especially for methods which influence the absorptivity.

With this in mind, the aims of the thesis are:

- To propose a mechanism for the formation of balling defects in copper and similar metals.
- To explain the dependence of the process and materials properties for on the formation of balling defects.
- To study the relevance of optical absorption in the solid phase close to the balling-conduction mode transition.
- To propose and develop efficient strategies for mitigation of balling defects in copper and similar metals and alloys.

3 Fluid dynamics simulation of LPBF

To simulate the melt pool shape and temperature fields of single LPBF tracks, the laser distribution, and the coagulation of powder during LPBF processing CFD simulations were performed using a custom FVM-VOF solver based on the OpenFOAM [142] solver InterFoam [27]. The solver first solves for the two phase fluid flow, then the temperature fields. After the solution for all fields the physical properties are updated for the next time step.

3.1 Phase field and momentum equation

The two phases of the system, metal and shielding gas, are described by the field ϕ, which is scalar value between 0 and 1, representing the volume fraction of the metallic phase. This field is evolved in time as a passive scalar:

$$\frac{\partial \phi}{\partial t} = -\vec{u} \cdot \nabla \phi \tag{3.1}$$

Where the velocity field, $\vec{u}$ is calculated for both phases from the momentum equation (see below). To avoid diffusion the so called TVD/MULES algorithm[43], which is already implemented in interFoam, is used.

The velocity field is solved from the momentum and continuity equations with the PIMPLE algorithm [108] as implemented in interFoam, with the following source terms added:

- The tangential component of the surface tension due to temperature gradients, $\vec{S}_{\parallel}$.
- Recoil pressure, $\vec{S}_R$
- A Darcy term to stabilize the solid part of the metal phase, $\vec{S}_D$

The surface tension is implemented on volumetric form with smearing towards the heavier phase:

$$\vec{S} = (\vec{S}_{\parallel} + \vec{S}_{\perp})|\nabla \phi| \frac{2\rho}{\rho_g + \rho_m} \tag{3.2}$$

with $\vec{S}_{\parallel}$ and $\vec{S}_{\perp}$ given by equation 2.25 and 2.24 respectively. Recoil pressure was evaluated as a simple source term, without directly considering the evaporating species [80]:

$$\vec{S}_R = -0.54 P_0 \exp \frac{L_{vap} M (T - T_v)}{R T T_v} \vec{n} |\nabla \phi| \frac{2\rho}{\rho_g + \rho_m} \tag{3.3}$$

where P_0 atmospheric pressure, L_{vap} is the enthalpy of vaporization, M the molar mass, and T_v boiling temperature.

A fictional force, a so called Darcy term, was added to constrain the solid metal from moving [130]:

$$\vec{S}_D = \begin{cases} -10^6 \frac{(1-\gamma)^2}{\gamma^3 + \varepsilon} & T \leq T_m \\ 0 & T > T_m \end{cases} \tag{3.4}$$

with $\gamma = \min(1, \max(0, \frac{T - T_s}{T_l - T_s}))$, where T_s, T_l, and T_m are solidus, liquidus, and melting temperature respectively. ε is a small coefficient to avoid division by 0.

3.2 Temperature field

The evolution of the temperature field, T, was implemented as a diffusive and advective scalar with source terms corresponding to evaporative cooling, S_E, and the laser, S_L:

$$\frac{\partial(\rho C_p T)}{\partial t} = -\vec{u} \cdot \nabla T + \nabla k \nabla T + S_E + S_L \tag{3.5}$$

The evaporation is corresponding to the recoil pressure in equation 3.3 [80]:

$$S_E = 0.82 \frac{L_{vap} P_0 M}{\sqrt{2\pi R T T_v}} \exp\left(L_{vap} \frac{M (T - T_v)}{R T T_v} \right) |\nabla \phi| \frac{2\rho}{\rho_g + \rho_m} \tag{3.6}$$

The laser was simulated by generation of discrete particles on every cell, i, of the domain boundary. For every time step all the particles are traced throughout the domain in discrete steps, reflecting on the gas-metal interfaces it encounters, shown in figure 3.1. The particle is described by a power, P_i^j, position $\vec{r}_i^{\,j}$, and direction, $\vec{d}_i^{\,j}$, where i indicating the cell of origin and j the current iteration. Each particle has an initial power described by a Gaussian distribution:

$$P_i^0 = \frac{2}{\pi r_l^2} A_i \exp\left(- \frac{2\left((x_i - x_0)^2 + (y_i - y_0)^2 \right)}{r_l^2} \right) \tag{3.7}$$

Where r_l is the laser radius, A_i the face area of the initial boundary cell, (x_i, y_i) the in plane coordinates of the cell. (x_0^t, y_0^t) is the position of the beam center at time t, which is updated for every time step: $(x_0^{t+\Delta t}, y_0^{t+\Delta t}) = (x_0^t, y_0^t) + \Delta t (v_x, v_y)$, where (v_x, v_y) is the laser velocity. The initial position is given by the center of the initial cell $\vec{r}_i^{\,0} = (x_i, y_i, z_i)$, and the initial direction by the laser direction: $d^0 = (0, 0, -1)$.

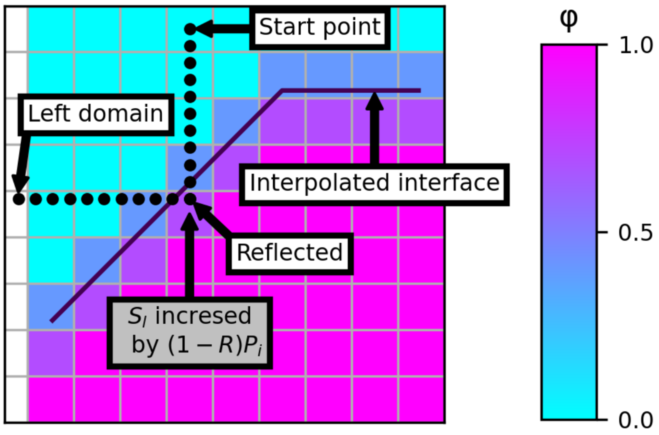

Figure 3.1 – Illustration of the laser tracing algorithm.

This particle is traced throughout the domain, by iteratively moving the particle:

$$\vec{r}_i^{\,j+1} = \Delta x_{\text{laser particle}} \vec{d}_i^{\,j} + \vec{r}_i^{\,j} \tag{3.8}$$

Where $\Delta x_{\text{laser particle}}$ is a step distance smaller than the domain grid size.

If the particle hits the interface between gas and metal, defined as it being in a cell where $\phi(\vec{r}_i^{\,j}) > 0.6$ three things happen:

- A new direction is calculated from equation 2.33: $\vec{d}_i^{\,j+1} = \vec{d}_i^{\,j} - 2(\vec{d}_i^{\,j} \cdot \vec{n})\vec{n}$.
- The laser heat source term S_L is incremented by $(1-R)P_i^j$ in the cell of reflection. R is the metal reflectivity (discussed below).
- The particle power is updated $P_i^{j+1} = RP_i^j$.

This process is only performed if the reflection directs the particle into a region of lower ϕ. Why this restriction is necessary is shown in figure 3.1, where in the step after the reflection the value of ϕ is still less than 0.6.

The process is repeated until one of the following situations are encountered:

- The particle leaves the domain, in which case the particle is killed.
- The power of the particle is less than $0.01P$, in which case the particle is killed.
- A domain boundary with a symmetry boundary condition is encountered, in which case the particle is reflected around the boundary normal.

3.3 Temperature and phase dependence of physical properties

To treat the difference in properties of the solid metal, liquid metal and gas the physical properties were evaluated at every time step according to the value of the phase field and the temperature. The temperature regimes are divided into three regimes by the value of $\gamma = \min 1, \max(0, \frac{T-T_s}{T_l-T_s})$. γ is 0 below the solidus temperature of the metal, 1 above the liquidus temperature of the metal, and linearly increasing from 0 to 1 in the mushy zone in-between. The phase fraction of the three phases is then given by:

$$\phi_\mathrm{s} = \phi(1-\gamma) \tag{3.9}$$

$$\phi_\mathrm{l} = \phi\gamma \tag{3.10}$$

$$\phi_\mathrm{g} = 1-\phi \tag{3.11}$$

The viscosity is within each phase temperature independent and is interpolated from the solidus to the melting point from the value of the solid:

$$\mu = \begin{cases} (1-\phi)\mu_g + \phi\mu_s & , T \leq T_s \\ (1-\phi)\mu_g + \phi\mu_l & , T_m \leq T \\ (1-\phi)\mu_g + \phi\left(\mu_s + \frac{\mu_l-\mu_s}{T_m-T_s}(T-T_s)\right) & , T_s < T < T_m \end{cases} \tag{3.12}$$

which allows the solid phase to be modeled by a high viscosity term instead of the Darcy's term. This approach is not however not used in this work as it tends to make the simulations numerically unstable, and $\mu_s = \mu_l$ for all cases presented. To avoid diffused metal phase making the gas phase artificially viscous, equation 3.12 above was only used if $\phi > 0.01$, and otherwise evaluated as μ_g.

The specific heat is also considered constant per phase, with an increased value in the mushy zone to account for the latent heat of melting:

$$C_p = \begin{cases} (1-\phi)C_p^g + \phi C_p^s & , T \leq T_s \\ (1-\phi)C_p^g + \phi C_p^l & , T_l \leq T \\ (1-\phi)C_p^g + \phi C_p^m & , T_s < T < T_m \end{cases} \tag{3.13}$$

with $C_p^m = \frac{L_f}{T_l-T_s} + \frac{C_p^s+C_p^l}{2}$.

The thermal conductivity within each of the phases is also temperature dependent:

$$C_p = \begin{cases} (1-\phi)k_g + \phi k_s(T) & , T \leq T_s \\ (1-\phi)k_g + \phi k_l(T) & , T_l \leq T \\ (1-\phi)k_g + \phi_s k_s(T) + \phi_l K_L(T) & , T_s < T < T_m \end{cases} \tag{3.14}$$

where the temperature dependence is linear:

$$k_g(T) = k_g^{ref} + (T - T_{ref,g})k_g' \tag{3.15}$$

$$k_s(T) = k_s^{ref} + (T - T_{ref,l})k_l' \tag{3.16}$$

$$k_l(T) = k_l^{ref} + (T - T_{ref,s})k_s' \tag{3.17}$$

The reflectivity is incorporated in three different models, the simplest being a constant value:

$$R = \text{constant} \tag{3.18}$$

It can also be selected constant per phase:

$$R = \begin{cases} R_l & , T_M \leq T \\ R_s & , T < T_S \end{cases} \tag{3.19}$$

It can also be calculated from the value complex dielectric constant, ϵ of the material according to Fresnels law:

$$R = \frac{\left|\frac{\cos\theta_i - \sqrt{\epsilon - \sin^2\theta_i}}{\cos\theta_i + \sqrt{\epsilon - \sin^2\theta_i}}\right|^2 + \left|\frac{\epsilon\cos\theta_i + \sqrt{\epsilon - \sin^2\theta_i}}{\epsilon\cos\theta_i + \sqrt{\epsilon - \sin^2\theta_i}}\right|^2}{2} \tag{3.20}$$

Finally Comin's model [20] for the temperature dependence of the dielectric function of metals was implemented. In this model the collision frequency is calculated from the electrical conductivity, $\sigma(T)$:

$$\tau(T) = \frac{\sigma_0(T) m_e}{n_{\text{eff}} e^2} \tag{3.21}$$

Where $\sigma_0(T) = \sigma_{\text{corr}} \times \sigma(T)$ is the corrected DC electrical conductivity, $n_{\text{eff}} = Z^* \rho N_A / M$ is the a corrected electron density based on the effective valency Z^*, density ρ, Avogadros number N_A, and molar mass M, m_e is the electron mass, and e the electron charge $\sigma(T) = 1/(\eta(T) + \eta_0)$ is calculated from a second order polynomial for the electrical resistivity of each phase ($\eta(T)$) plus a contribution from impurities (η_0). From the calculated value of τ the dielectric function is calculated by equation 2.36 with the modified electron density:

$$\varepsilon = \left(1 - \frac{n_{\text{eff}} e^2 \tau^2}{m_e \varepsilon_0 (1 + \omega^2 \tau^2)}\right) + i\left(\frac{n_{\text{eff}} e^2 \tau}{\varepsilon_0 m_e \omega (1 + \omega^2 \tau^2)}\right) \tag{3.22}$$

The reflectivity is then calculated from 3.20.

3.4 Physical parameters and numerical schemes

The physical properties for simulation of bronze is given in table 3.1, and the corresponding values for the simulation of copper in table 3.1. The boundary conditions for the non-symmetry plane (which had a symmetry plane BC) are shown in table 3.3 and the following numerical schemes where used:

- $\frac{\partial}{\partial t}$, Euler
- ∇, Gauss linear
- $\nabla\cdot$, defaults to Gauss linear if not one of the following:
  - $\nabla\cdot(\rho\vec{u}\vec{u})$, Gaussian linear upwind
  - $\nabla\cdot(\vec{u}\phi)$, Gaussian vanLeer
  - $\nabla\cdot(\vec{u}T)$, Gaussian upwind
- ∇^2, corrected Gaussian linear

Table 3.1 – CFD model parameters used for simulating bronze.

	Property	Value	Notes
T_s	Solidus temperature	1153 K	Calculated for Cu-7Sn using Thermo-Calc TCAL7
T_l	Liquidus temperature	1306 K	Calculated for Cu-7Sn using Thermo-Calc TCAL7
T_v	Boiling temperature	2800 K	Value of copper
$k_{s,l}$	Thermal conductivity	$77\,\mathrm{W\,m^{-1}\,K^{-1}}$	Estimated from Nordheim's and Franz-Wiedeman's laws
$k'_{s,l}$	Temp dep. of th. cond.	$0\,\mathrm{W\,m^{-1}\,K^{-2}}$	No temperature dep.
k_g	Thermal conductivity, gas	$2 \times 10^{-2}\,\mathrm{W\,m^{-1}\,K^{-1}}$	Standard value
k'_g	Temp dep. of th. cond., gas	$0\,\mathrm{W\,m^{-1}\,K^{-2}}$	Neglected
M	Molar mass	$65.5\,\mathrm{g\,mol^{-1}}$	Standard value for Cu-6.7Sn-0.3Ni
C_p^s	Specific heat capacity, solid	$426\,\mathrm{J\,kg^{-1}\,K^{-1}}$	Calculated for Cu-7Sn using Thermo-Calc TCAL7
C_p^l	Specific heat capacity, liquid	$475.9\,\mathrm{J\,kg^{-1}\,K^{-1}}$	Calculated for Cu-7Sn using Thermo-Calc TCAL7
C_p^g	Specific heat capacity, air	$1000\,\mathrm{J\,kg^{-1}\,K^{-1}}$	Standard value
L_f	Latent heat of fusion	$175.3\,\mathrm{kJ\,kg^{-1}}$	Calculated for Cu-7Sn using Thermo-Calc TCAL7
L_v	Latent heat of vaporization	$4510\,\mathrm{kJ\,kg^{-1}}$	Calculated as simple mixture from standard data
σ	Surface tension	$1.4\,\mathrm{N\,m^{-1}}$	For Cu-7Sn, [82]
σ'	Temperature coefficient for surface tension	$-0.16\,\mathrm{N\,m^{-1}\,K^{-1}}$	For Cu-7Sn, [82]
R	Reflectivity	0.6	Free parameter
P_0	Surrounding pressure	$1 \times 10^5\,\mathrm{Pa}$	Atmospheric pressure
ρ_l	Metal density	$8000\,\mathrm{kg\,m^{-3}}$	Value of copper at 1700 K
ρ_g	Gas density	$1\,\mathrm{kg\,m^{-3}}$	

Table 3.2 – CFD model parameters used for simulating copper.

	Property	Value	Notes
T_s	Solidus temperature	1338 K	Standard value 1338 K - 20 K
T_l	Liquidus temperature	1378 K	Standard value 1338 K + 20 K
T_v	Boiling temperature	2800 K	Standard value
k_s	Thermal conductivity, solid	$370\,\mathrm{W\,m^{-1}\,K^{-1}}$	[11]
k_s'	Temp dep. of th. cond., solid	$-7.88\times10^{-2}\,\mathrm{W\,m^{-1}\,K^{-2}}$	[11]
k_l	Thermal conductivity, solid	$370\,\mathrm{W\,m^{-1}\,K^{-1}}$	[11]
k_l'	Temp dep. of th. cond., liquid	$4.97\times10^{-2}\,\mathrm{W\,m^{-1}\,K^{-2}}$	[11]
k_g	Thermal conductivity, gas	$2\times10^{-2}\,\mathrm{W\,m^{-1}\,K^{-1}}$	Standard value
k_g'	Temp dep. of th. cond., gas	$0\,\mathrm{W\,m^{-1}\,K^{-2}}$	Neglected
M	Molar mass	$63.5\,\mathrm{g\,mol^{-1}}$	Standard value for Cu-6.7Sn-0.3Ni
C_p^s	Specific heat capacity, solid	$481\,\mathrm{J\,kg^{-1}\,K^{-1}}$	[11]
C_p^l	Specific heat capacity, liquid	$531\,\mathrm{J\,kg^{-1}\,K^{-1}}$	[11]
C_p^g	Specific heat capacity, air	$1000\,\mathrm{J\,kg^{-1}\,K^{-1}}$	Standard value
L_f	Latent heat of fusion	$208\,\mathrm{kJ\,kg^{-1}}$	[11]
L_v	Latent heat of vaporization	$4700\,\mathrm{kJ\,kg^{-1}}$	Standard value
σ	Surface tension	$1.3\,\mathrm{N\,m^{-1}}$	
σ'	Temperature coefficient for surface tension	$-0.211\,\mathrm{N\,m^{-1}\,K^{-1}}$	
R_S	Reflectivity, solid	0.9	
R_L	Reflectivity, liquid	0.75	
P_0	Surrounding pressure	$1\times10^{5}\,\mathrm{Pa}$	Atmospheric pressure
ρ_l	Metal density	$8000\,\mathrm{kg\,m^{-3}}$	Value of copper at 1700 K
ρ_g	Gas density	$1\,\mathrm{kg\,m^{-3}}$	

Table 3.3 – The boundary conditions used in the simulations.

Field	**Boundary**	**Boundary condition**	**Value**
T	Top	Fixed value	300 K or 600 K
	Bottom	Fixed value	300 K or 600 K
	Sides	Fixed value	300 K or 600 K
$\vec{u}$	Top	Pressure inlet and outlet with fixed velocity	$(0,0,0)\,\mathrm{m\,s^{-1}}$
	Bottom	No slip	
	Sides	No slip	
α	Top	Zero gradient	
	Bottom	Zero gradient	
	Sides	Zero gradient	
$\rho + \rho g h$	Top	Total pressure	0 Pa
	Bottom	Fixed flux pressure	$0\,\mathrm{Pa\,m^{-1}}$
	Sides	Fixed flux pressure	$0\,\mathrm{Pa\,m^{-1}}$

4 Materials and methods

4.1 Laser processing setups

Several different laser systems were used for the experiments in this thesis. The functionality of these systems and the experimental setups are described below. Specific parameters are shown together with the experimental results in their respective chapters.

4.1.1 Laser powder bed fusion

The LPBF experiments were made on a commercial MySint 100 (Sisma, IT) LPBF machine[1] equipped with a 200 W 1064 nm fiber laser with a Gaussian beam of $1/e^2$-spot size of 55 µm. The build chamber is during operation filled with argon (Ar96, 99.996 %, AirLiquide, FR). The oxygen content is monitored with an oxygen sensor and was typically kept at 0.1 %. The flow of the shielding gas was for all experiments set to $2\,\mathrm{m\,s^{-1}}$. The substrate has a diameter of 33 mm and was made from a phosphorous bronze or stainless steel.

Most of the LPBF samples produced for this thesis are in the shape of cubes, typically dimensioned 5 mm × 5 mm × 5 mm. For some experiments, cylinders of diameter and height 5 mm were used to produce samples suitable for computer X-ray tomography analysis. For the majority of the experiments, multiple samples where made at the same substrate. To ensure that the coating blade did not get caught on the sample edge they were turned 45° with respect to the coater, as illustrated in figure 4.1. The scanning pattern was either unidirectional, or unidirectional with alternating layers at 90° angle to each other, also illustrated in 4.1. To be able to keep track of the samples after production, sample number 1 was often displaced by a small amount. The samples were separated from the substrate by electric discharge machining (EDM), which removed up to 500 µm of the sample.

The powders used were:

---

[1] Shown in figure 2.2.

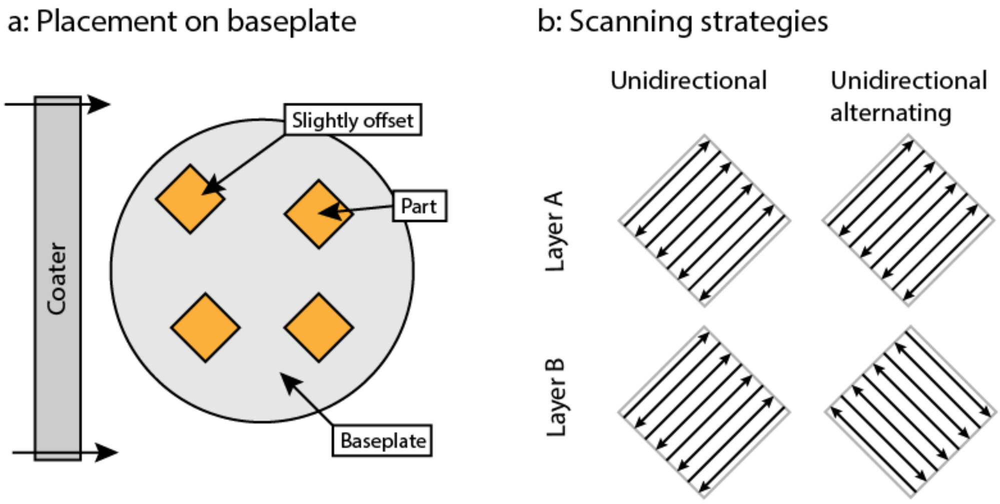

Figure 4.1 – (a) The positioning of the samples on the substrate exemplified by a build job with four parts. (b) The hatch vectors for the two scanning strategies which were used in this work.

- Oxygen free high conductivity copper (Sandvik Osprey, GB). Minimum diameter 22 µm, max diameter 45 µm.
- 316L Stainless steel (Oerlikon Metco, CH). Mean diameter 29.3 µm, max diameter 45 µm.
- Cu-6.7 wt.%Sn-0.3 wt.%Ni (unknown producer). Minimum diameter 22 µm, max diameter 45 µm.

4.1.2 Combined IR and green laser welding

Laser welding of copper was performed using a laser system consisting of two lasers focused on the same spot on a moving substrate, as shown in figure 4.2. The main laser is a pulsed 1070 nm fiber laser (LFS-150, Coherent, CH) with a maximum power of 275 W focused on a spot of diameter 50 µm. The laser fires pulses, see 4.2 a), of variable length and constant power, at 10 Hz. The green laser is a q-switched frequency doubled ND:YAG laser which fires pulses synchronized with the IR-laser, see figure 4.2 b). The pulses are around 50 ns long and delivers up to 30 mW averaged over a pulse, resulting in a peak instantaneous power of around 150 kW. The profile of both the green and the IR lasers are somewhat irregular, see figure 4.2 c).

The stage is movable in the horizontal direction at around 85° relative to the incoming laser beam such that the laser light is not reflected back into the optics. A laminar flow shielding gas nozzle was mounted by the stage, providing shielding with N_2-gas for the experiments. A high speed camera was mounted from the side of the stage, and was used to capture images at a rate of 30 000 Hz with a resolution of 128 px × 128 px.

High conductivity, oxygen-free, copper plates (99.95 % , Goodfellow) were carefully polished

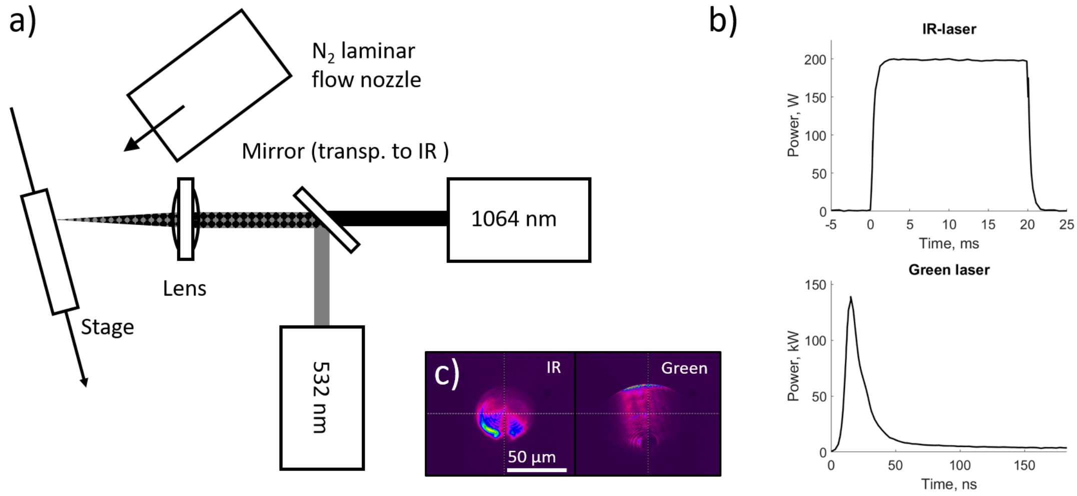

Figure 4.2 – a) Schematic of the laser system used. b) Normalized intensity of the pulses from the lasers at 200 W pulse power for the IR laser and 3 mJ pulse energy for the green laser. Note that the scale is in milliseconds and Watt for the IR-laser and nanoseconds and Kilowatt for the green laser. The time axis is from the start of the respective pulse, which can be adjusted relative to each other. Unless noted the green laser fires on the left shoulder of the IR pulse. c) Measured beam profile of the IR and green laser.

with 50 nm Silica and Alumina particles. The plates were deoxidized in 2 % HCl solution and placed on the stage at an angle ensuring the samples stay in focus during the whole experiment. Some of the samples were cross-sectioned and imaged using a Helios 660 FIB (ThermoFisher, US).

4.1.3 Single LPBF line tracks with green laser

Single laser passes of copper powder on a copper substrate were performed. The laser system consists of a 532 nm GLR-100 continuous wave green laser (IPG Photonics, US). Behind the modulator the beam is expanded in a 12 mm AL1512-A lens (Thorlabs, US) and then focused through two 200 mm AL100200-A lenses (Thorlabs, US) on the target. The nominal power is 100 W, which after losses amount to around 66 W behind the optics. The target is placed on a moving stage, capable of moving at speeds of 8 mm s^{-1}. The laser spot is Gaussian with an estimated size 15 µm.

Two 25 mm × 25 mm × 0.8 mm copper plates (99.9 %, oxygen free, Goodfellow, U.K.) were machined flat. Grooves 5 and 10 µm (±2 µm) deep were machined on the top surface. Copper powder (< 5 µm, 99.9 %, oxygen free, Goodfellow, U.K.) was mixed with isopropanol and the paste was smeared in the grooves. After letting the isopropanol evaporate the plate was placed on a movable stage and single line tracks were made in the groove. The line tracks were imaged in a confocal microscope (Keyence VK-X8700) before and after powder removal, and with SEM (Nova NanoSEM 230, FEI, USA) after powder removal.

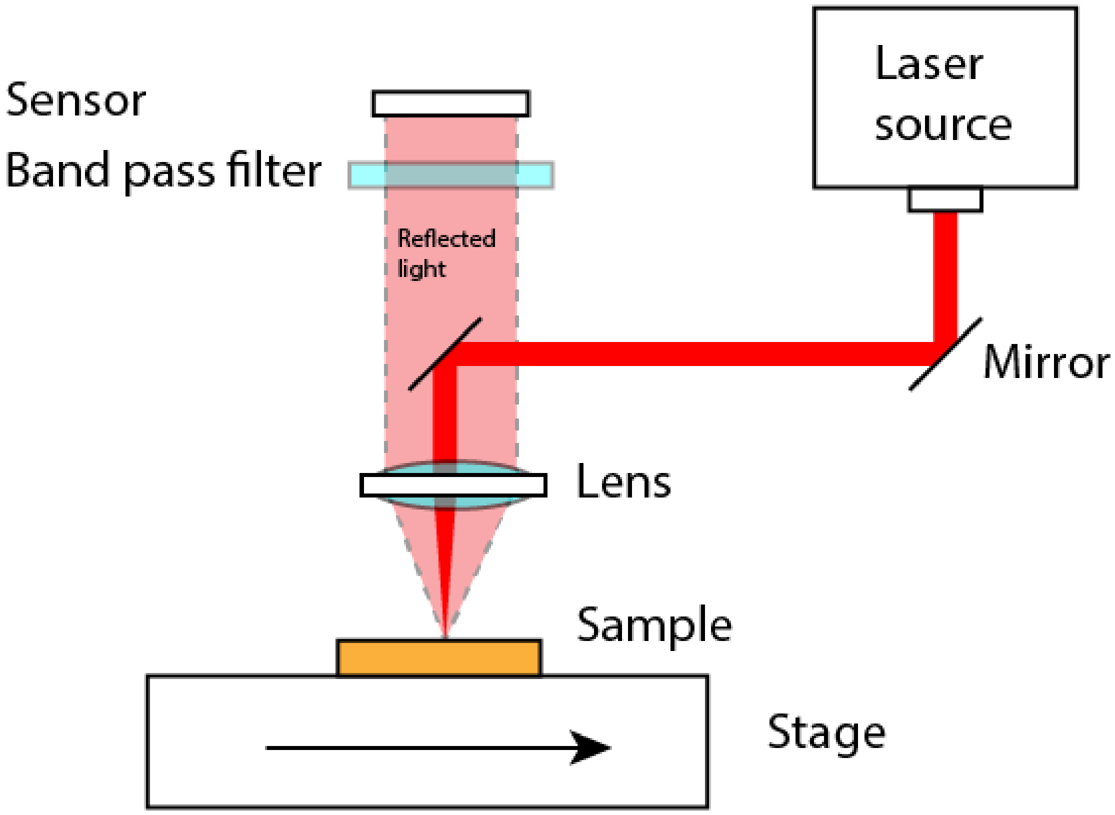

Figure 4.3 – Schematic of IR laser processing setup for back-reflection measurements.

4.1.4 Single LPBF line tracks with IR laser

Single laser passes were made using an IR laser setup with a sensor for measuring back reflections from the work piece, the setup is described in detail in a paper by Schevchik et al. [124]. The system consists of a 1070 nm StarFiber150 P fiber laser (Coherent, CH), focused through a 170 mm focal length. The laser is focused with a spot diameter of 30 µm on a M-663.5U moving stage (Physik Instrumente, DE) capable of moving at up to 100 mm s^{-1}. A Ge-sensor was placed according to figure 4.3 behind a 1070 nm band pass filter, allowing the sensing of the back reflections. Other sensors were connected through a multispectral splitter, but they were not used for these experiments, see the paper mentioned above for details.

4.2 Analysis of LPBF parts

In order to study the quality of the manufactured samples several analysis methods were used. Metallographic cross-sections were prepared by cutting the samples along the middle with an aluminum oxide blade, followed by hand grinding and automatic polishing. Typically the order of grinding was: P180, P240, P600, P800, P1200, P2400, and P4000, followed by polishing with 3 µm diamond suspension, 50 nm silica suspension, and finally vibrapolishing with 50 nm alumina suspension. A worry when preparing soft samples is that pores can easily get smeared over, because of this a small (around 2 N to 4 N) force was used. Furthermore the porous samples were ultrasonically cleaned in a heated bath in-between the grinding and polishing steps to release any material trapped in the pores.

The cut samples were imaged in an optical microscope (Leica Axiovert 100, Leica, DE) and by SEM (Nova NanoSEM 230, FEI, USA). Cross-sectional density was measured from the images using the automatic thresholding function of FIJI [117], and the composition was in relevant cases measured by X-ray Fluorescence Spectroscopy (XRF, Fischerscope X-Ray XDV-SDD , Fisher Technology, US) of the cut and polished samples.

X-ray micro computer tomography (EasyTom XL Ultra, RX Systems, FR) was, with the assistance of Dr. Kai Zweiacker, performed on cylindrical samples. This setup works in a cone beam setup using two sources (160 and 230 kW). Imaging was done using a 3 Mpx detector (Varian PaxScan, US). The reconstructed image was binarized and filtered using a 2 px × 2 px × 2 px median filter followed by thresholding in FIJI using the Huang's method [48] or the max entropy method [65] based on inspection of which gave better results. The relative density was calculated by counting pixels of a cube cut out from the center of the images.

4.3 Coating of powder using immersion deposition

Gas atomized oxygen free high conductivity copper powder (Sandvik Osprey, GB) was coated with thin layers of tin or nickel using an immersion deposition method. These depositions work by having a metal salt in aqueous solution react with the copper, reducing the metal ion and oxidizing the copper: $2\,\mathrm{Me}^{n+}_{(\mathrm{aq})} + n\mathrm{Cu} \rightleftharpoons n\mathrm{Cu}^{2+}_{(\mathrm{aq})} + 2\,\mathrm{Me}$. In order to shift the equilibrium to the right a lixiviant is added, in this case thiourea (CH_4N_2S, 99% Alfa Aesar, USA), which forms a strong complex with copper ions, was used. The salts used where tin(II) chloride ($SnCl_2$, anhydrous, 99%, EMD Millipore, USA) and Nickel(II)Chloride ($NiCl_2$, anhydrous, 99%, AlfaAesar, USA).

The general recipe for the procedure is as follows, with the exact conditions are specified in table 6.2.

1. A solution (solution 1) was prepared by deoxidizing ionized water by boiling, after which thiourea was dissolved.

2. Another solution (solution 2) was prepared with the salt dissolved in deoxidized and deionized water, with hydrochloric acid (HCl, Sigma Aldrich, US) added to avoid oxidation of the salt.

3. Solution 1 was allowed to cool down to the desired reaction temperature. Under magnetic stirring the copper powder was added, and hydrochloric acid was added to deoxidize the powder. The copper powder was stirred so that the powder remained suspended in the solution.

4. Solution 2 was added to solution 1, and the reaction was let proceeding for the desired time, after which the solution was decanted and the powder repeatedly washed with deionized water, ethanol, and isopropanol. The powders were air dried, after which they where sieved.

A second set of powders were manufactured by Serhii Derevianko and Vladyslav Morozovych at Cherkasy National University. These powders were treated in a reaction bath that additionally contained $80\,\mathrm{g\,L^{-1}}$ NaCl. One batch was processed with sulfuric acid (H_2SO_4) instead of HCl.

The manufactured powders were imaged using Scanning Electron Microscopy (SEM). A selection of the powders were also, with the help of Dr. Oleksii Liashenko, cross-sectioned using ion beam milling to allow the study of the coating layer. The diffuse reflectance spectrum of the powders was measured by Dr. Yevhen Shynkarenko in a Jasco V770 spectrophotometer (Jasco, US) using a powder holder (PSH-002, Jasco) in the back of an ISN-923 integrating sphere ISN-923 (Jasco). A reflectance measurement adapter was applied during the measurement to remove specularly reflected light component. The double reference method was used to recalculate the powder reflectivity. $BaSO_4$ powder was used for a baseline correction and acetylene carbon black powder as a dark reference. All the signal corrections was made automatically in the Jasco software.

5 The balling phenomenon

In this chapter, the balling phenomenon, and how it is related to the formation of balling porosity is studied. Although there are many studies with different approaches for decreasing the porosity of group 11 metals, for example by changing process parameters, surface treatments, and alloying, it is not clear how effective these approaches are in relation to each other. In this chapter a simple analytical criterion for when balling occurs is developed and experimentally validated. Although this model is simple it gives much insight into the mechanism of balling and acts as a starting point for developing and comparing pore-mitigation strategies.

The work of this chapter is mainly based on the paper *Modeling and simulation of balling defect formation during laser powder bed fusion* [87], which at the point of writing is in submission for publication.

5.1 A model for the balling phenomenon

Analytical models for predicting melt pool properties are typically based on solving equation 2.6 for a slab with a heat source term distributed as the laser source or an approximation thereof. This approach, well known from the field of welding [107], predict the size of conduction mode melt pools well, and is therefore useful for prediction of lack-of-fusion defects [132]. Balling mode, however, is not necessarily well approximated by these models, as the heat gets diffused through the cap, decreasing the influence of the laser distribution. This is shown schematically in figure 5.1, where the quasi-one-dimensionality of the balling cap create a uniform heat source into the substrate, whereas the thin conduction weld does not significantly distort the laser distribution. This type of heat source term is in this section used to predict the melt pool dimensions and cap shape, allowing the prediction of balling defects based on geometrical arguments.

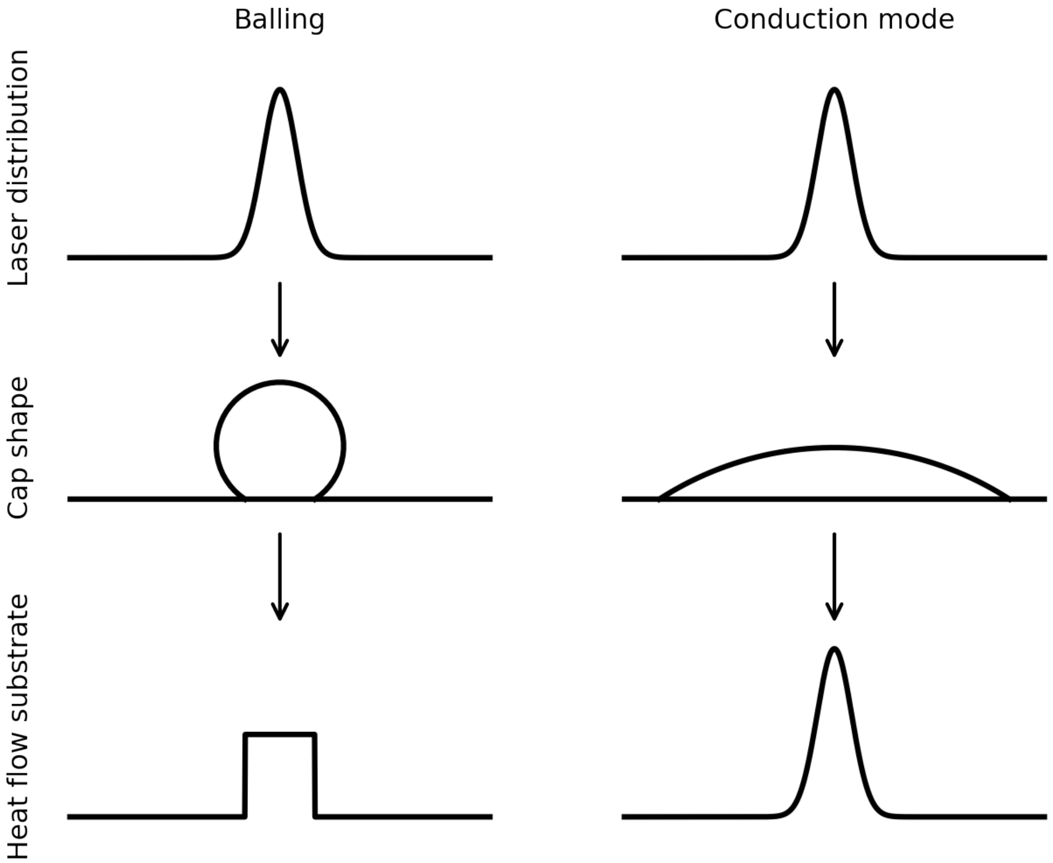
Balling
Conduction mode
Laser distribution
Cap shape
Heat flow substrate

Figure 5.1 – The heat flow into the substrate is distributed differently in balling and conduction mode.

5.1.1 The substrate temperature field

As the laser spot travels over the powder bed, it will induce melting of one or more powder particles. Heat accumulates inside the powder particles because it releases to the substrate slowly through a narrow point contact, leading to temperatures well above the melting temperature of the material. The molten particles will, as shown by numerical simulations [66], start wetting their neighbors, which will start melting as well and agglomerate into one cohesive melt due to the surface tension of the liquid metal. Once the molten powder starts wetting the surface of the previously consolidated layer the heat transfer to the substrate will gradually increase.

Balling mode

In balling mode, that is when the contact angle $\theta > 90°$, the heat transfer across the cap-substrate interface is assumed approximately uniform over the contact area. This corresponds to the thermal boundary condition of the substrate:

$$\left.\frac{\partial T}{\partial z}\right|_{z=0} = \begin{cases} -\frac{\alpha P}{k A_{wetted}} & \text{, wetted surface} \\ 0 & \text{, non-wetted surface} \end{cases} \tag{5.1}$$

where T is the temperature in the substrate, z the depth in the substrate, A_{wetted} the wetted area, P the laser power, α the optical absorptivity and k the thermal conductivity. The temperature field in the substrate is, neglecting the liquid flow and temperature dependence of the metal properties, at steady-state governed by equation 2.6:

$$0 = -u\rho C_p \frac{\partial T}{\partial x} + k\nabla^2 T \tag{5.2}$$

In some situations the scanning speed, u, is low compared to the thermal diffusivity, as indicated by a Péclet number, $Pe = (u\rho C_p a)/k < 1$, where a is the characteristic length scale usually chosen to be the $1/e^2$ laser radius. If this is the case, equation 5.2 is reduced to Laplace's equation:

$$0 = \nabla^2 T \tag{5.3}$$

This is realistic for metals like copper, gold, and silver, where the Péclet number is around 0.2 for a scanning speed of 300 mm/s.

Assuming a circular contact area of radius r_w (the wetting radius) between the molten cap and the substrate, the boundary condition of the substrate becomes:

$$\left.\frac{\partial T}{\partial z}\right|_{z=0} = \begin{cases} -\frac{\alpha P}{2\pi r_w^2 k} & r < r_w \\ 0 & r > r_w \end{cases} \tag{5.4}$$

According to Carslaw and Jaeger [12] Laplaces's equation with these boundary conditions has an analytical solution in cylindrical coordinates given by:

$$T(r,z) = T_0 + \frac{\alpha P}{2\pi r_w K}\int_0^\infty d\lambda \exp(-\lambda|z|)\frac{J_0(\lambda r)J_1(\lambda r_w)}{\lambda} \tag{5.5}$$

where J_0 and J_1 are the zeroth and first Bessel functions of the first kind, r is the radial distance from the center and T_0 the initial temperature of the substrate. Note that λ is an index variable, which disappears upon calculation of the integral.

As the liquid spreads over the solid surface, heat dissipation increase due to the increased contact area. The wetting of a liquid metal on its own substrate is near perfect, so the molten powder would in principle be able to spread over the complete substrate. However, at some point the temperature in the melt close to the triple line separating the liquid, solid and gas phase, $T(r_w,0)$, will reach the melting temperature, T_m and solidification of the cap will begin, thereby hindering any further spreading of the melt.

To find the point where spreading is halted we set $T_m = T(r_w,0)$ in equation 5.5, which with the substitution $\lambda' = \lambda r_w$ leads to:

$$T_m = T(r_w,0) = \frac{\alpha P}{2\pi r_w K}\int_0^\infty d\lambda' \frac{J_0(\lambda')J_1(\lambda')}{\lambda'} \tag{5.6}$$

The numerical value of the integral, I, is approximately 0.64. Setting $\Delta T_m = T_m - T_0$ we get the equilibrium wetting radius:

$$r_w = \frac{I}{2\pi}\frac{\alpha P}{\Delta T_m K} \tag{5.7}$$

Thin cap

As the molten powder spreads over the substrate, the contact angle and the height of the cap decrease. If it becomes thin enough the thermal boundary condition will no longer be well approximated by equation 5.4, as shown in figure 5.1,. Instead, the boundary condition will begin to approximate the laser intensity distribution. As a first approximation, it is assumed that the heat transfer to the substrate is then described by:

$$\left.\frac{\partial T}{\partial z}\right|_{z=0} = \begin{cases} -\frac{\alpha P}{2\pi r_l^2 k} & r < r_l \\ 0 & r > r_l \end{cases} \tag{5.8}$$

Which is the same as equation 5.4, but with the radius of the laser spot, r_l, instead of the wetting radius. The thermal field is thus given by:

$$T(r,z) = T_0 + \frac{\alpha P}{2\pi r_l k}\int_0^\infty d\lambda \exp(-\lambda|z|)\frac{J_0(\lambda r)J_1(\lambda r_l)}{\lambda} d\lambda \tag{5.9}$$

And the wetting radius by solving the following equation for r_w:

$$T_m = T(r_w, 0) = T_0 + \frac{\alpha P}{2\pi r_l k}\int_0^\infty d\lambda \frac{J_0(\lambda r_w) J_1(\lambda r_l)}{\lambda} d\lambda \tag{5.10}$$

5.1.2 The shape of the cap in balling mode

Since the cap will be constrained by the size of the melt pool, its can be predicted geometrically from the wetting radius given by equation 5.7 and the volume of molten metal along the track. For the sake of simplicity, it is assumed that the powder layer consists only of spherical powder grains with one well-defined powder radius, r_p, and that the powder is densely packed. For a melt track of along a symmetry axis of the powder layer the powder particle line density will be $1+2n$ powder grains per powder diameter. n is the number of nearest neighbor lines that have been coagulated into the melt , shown in figure 5.2 a). It is assumed that the melt has the form of an elongated circle segment, shown in figure 5.2 b). The relevant dimensions of the cap cross section are the cap height h, wetting radius r_w, circle segment radius R, and contact angle θ, as specified in figure 5.2 c).

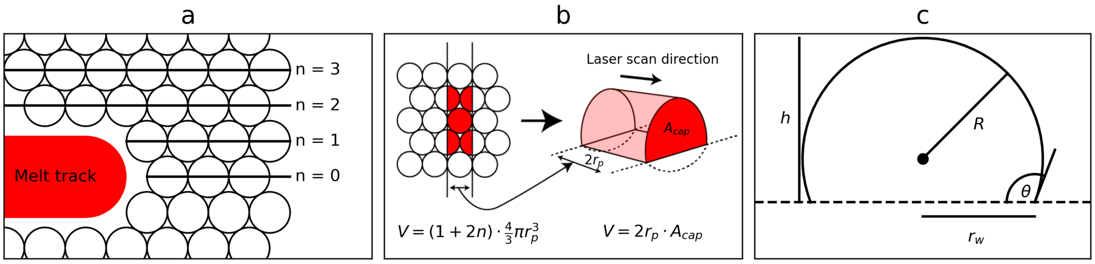

Figure 5.2 – (a) Melting of densely packed powder and wetting on a substrate. The number of wetted neighbor lines, n, is 1. (b) The volume of the molten powder is equivalent to the volume of the cap. (c) Schematic cross-section of the cap with the relevant parameters.

The volume of the melt track is given by the cross-sectional area, A_{cap}, multiplied by the track length. According to figure 5.2 b), the volume along a sement with the length of the powder diameter must be equal to the volume of the coagulated particles along the axis perpendicular to the melt track:

$$V = 2r_p A_{\text{cap}} = (1+2n)\frac{4}{3}\pi r_p^3 \tag{5.11}$$

The resulting equation for the cross-sectional area is thus:

$$A_{\text{cap}} = (1+2n)\frac{2\pi}{3} r_p^2 \tag{5.12}$$

The cross sectional area is that of a circular section:

$$A_{\text{cap}} = \frac{R^2}{2}(2\theta - \sin(2\theta)) \tag{5.13}$$

where R and θ can be calculated from the following two equations:

$$r_w = R \sin\theta \tag{5.14}$$

$$R = \frac{h}{2} + \frac{r_w^2}{8h} \tag{5.15}$$

The contact angle and height for a given wetting radius are obtained by numerically solving equations 5.12-5.15 for a given value of n. The solution of equation 5.12-5.15 is illustrated in figure 5.4 where the values of θ and h are shown as a function of r_w for $n = 1, 2$ and 3, with the distances normalized by r_p. Balling pores will form if $\Theta > 90°$ due to the formation of voids between the individual caps. For $n = 1$, the criterion is fulfilled when $r_w \approx 2r_p$. A slight fluctuation of the wetting width would however cause the cap to touch the powder particles in the next line ($n = 2$), causing them to coagulate into the melt (see figure 5.4)). This would cause the volume of molten material to increase, which in turn would lead to $\theta > 90°$. For $n = 2$ the fluctuation would have to be significantly larger to touch the powder belonging to line $n = 3$.

As a consequence balling pores will be avoided when $\theta < 90°$, with n=2. As can be seen in figure 5.4 a) this corresponds to $r_w \approx 2.6r_p$, or larger. When this occurs the height of the cap will still be higher than the original powder layer (see figure 5.4 b)). This could possibly lead to pores forming due to the uneven shape of the layer. Thus processing parameters should probably be chosen so that the wetting width is larger than $3.7r_p$. It is important to note that the expressions above the relevant powder radius is the largest powder radius in the distribution since the stochastic nature of the powder delivery will at some point bring a cluster of these close together, possibly leading to the formation of a pore.

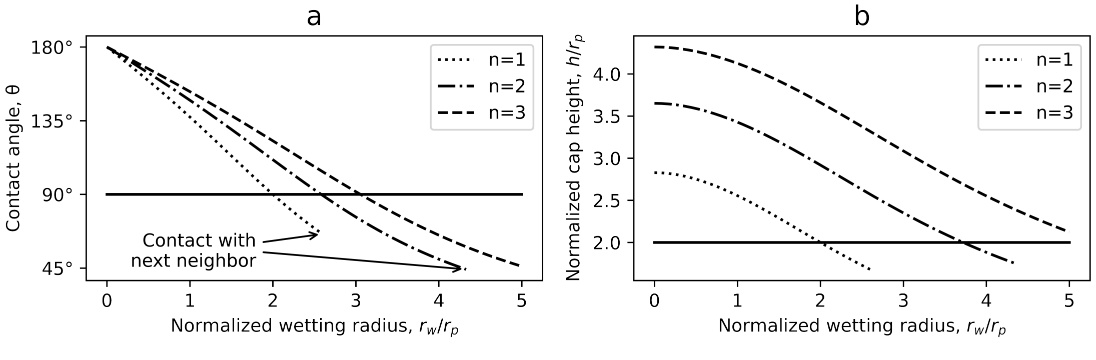

Figure 5.3 – The parameters of the cap as a function of the wetting radius calculated from equation 5.12-5.15 with $n = 1, 2, 3$. a) Contact angle, θ, with the balling criterion θ = 90ř marked. b) Cap height, h, with the solid line marking the point when the cap height is lower than the powder diameter. All distances are normalized by the powder radius.

5.1.3 A criterion for balling

Combining the criterion for balling, $r_w < 2.6 r_p$ with equation 5.7 results in the laser power required to avoid balling porosities:

$$P_{balling} = \frac{2\pi \cdot 2.6}{I} \frac{K \Delta T_m r_p}{\alpha} \approx 25.5 \frac{K \Delta T_m r_p}{\alpha} \tag{5.16}$$

A convenient way of expressing the power in dimensionless form is thus as a dimensionless number, from here on referred to as the balling number:

$$Ba = P / P_{\text{Balling}} \tag{5.17}$$

This number expresses how close the processing parameters are to the balling threshold.

The temperature field can be rearranged on dimensionless form (for a detailed derivation see appendix A):

$$\Theta(\mathfrak{R}, \mathfrak{Z}) = I^{-1} \int_0^\infty d\lambda' \frac{\exp\left(-\lambda' |\mathfrak{Z}|\right) J_0\left(\lambda' \mathfrak{R}\right) J_1\left(2.6 Ba \lambda'\right)}{\lambda'} \tag{5.18}$$

where the normalized temperature is given by $\Theta(\mathfrak{R}, \mathfrak{Z}) = (T(\mathfrak{R}, \mathfrak{Z}) - T_0)/(T_m - T_0)$ at the normalized coordinates $\mathfrak{R} = r/r_p$ and $\mathfrak{Z} = z/r_p$. From this expression it can be shown (see appendix A) the depth-to-width-ratio is constant, with a numerical value of 0.23 and that the peak substrate temperature is $\Theta = 1/I$. In figure 5.4 the normalized temperature field is shown below, at, and above the balling threshold. The cap shape calculated from equation 5.12-5.15 for $n = 1$ and $n = 2$ is included in the figure for reference.

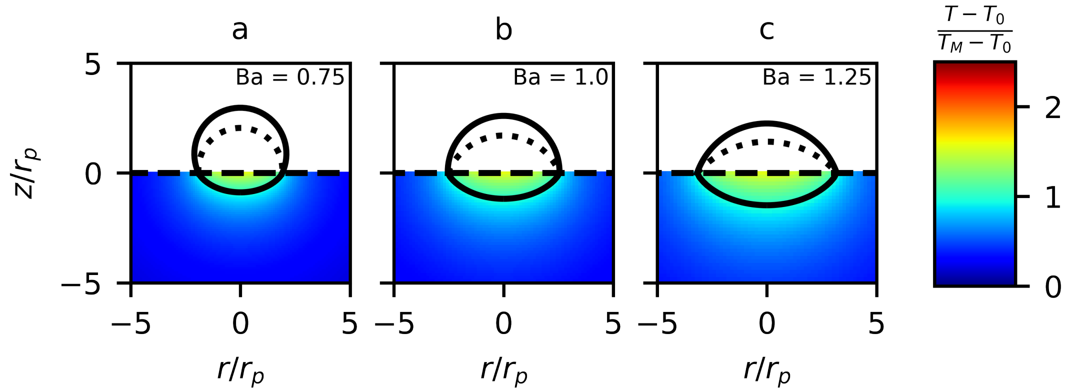

Figure 5.4 – The normalized temperature field of a single track calculated from equation 5.18 and the corresponding cap with $n = 1$ (dotted line) and $n = 2$ (solid line). a) Below the balling threshold, $Ba = 0.75$. b) At the balling threshold, $Ba = 1.0$. c) Above the balling threshold, $Ba = 1.25$.

5.1.4 The balling criterion in terms of the normalized enthalpy

The normalized enthalpy has been shown to be useful for predicting the transition from conduction mode to keyhole mode [36], with the transition occurring at around $H/h = 27.5$. If the balling power could be expressed in terms of normalized enthalpy we would therefore get a mathematical expression for the processing window, that is the space of parameters yielding neither balling nor keyholes. For the low scanning speed case outlined here we use the low scanning speed scaling proposed by Rubenchik et al. (equation 2.14) [114]. Using this scaling it is found that the temperature field is given completely by the parameter, B':

$$B' = \frac{\alpha P}{\pi \rho \bar{c}_p \Delta T_m D a} = \sqrt{\frac{Pe}{\pi}} \frac{H}{h} \tag{5.19}$$

with $\bar{c}_p = c_p + \Delta H_l / \Delta T_m$. Combining this expression with the balling power derived above we get the value for B' at the balling threshold, and noting that for metals $c_p >> \Delta H_l / \Delta T_m$:

$$B'_{\text{Balling}} = \frac{\alpha P_{\text{Balling}}}{\pi \rho c_p \Delta T_m D a} = \frac{2 \times 2.6}{I} \times \frac{r_p}{a} = \sqrt{\frac{Pe}{\pi}} \left(\frac{H}{h}\right)_{\text{Balling}} \tag{5.20}$$

The calculation above leads to the balling threshold expressed in terms of the normalized enthalpy:

$$\left(\frac{H}{h}\right)_{\text{Balling}} = 8.4 \sqrt{\frac{\pi}{Pe}} \frac{r_p}{a}. \tag{5.21}$$

This expression shows that at low scanning speeds there are two possibilities for widening the processing window, either operating at higher scanning speed (which requires a correspondingly larger power) or by using a laser spot size which is larger with respect to the powder size:

$$\left(\frac{H}{h}\right)_{\text{Keyhole}} \Bigg/ \left(\frac{H}{h}\right)_{\text{Balling}} \propto \sqrt{Pe} \frac{a}{r_p} \tag{5.22}$$

5.2 LPBF of copper and copper alloys at low power

In this section the balling phenomenon is studied experimentally and compared to the model developed in the previous section. It is seen that the model for the width of the cap wetting in balling conditions (equation 5.7) agrees well with the experiments up until the balling threshold, after which the values fluctuate between the values of this model and the model for thin welds (equation 5.10). Furthermore it is shown that the balling number seems to be a good predictor of relative density, which changes linearly below the balling threshold.

5.2.1 The role of oxygen for balling in copper based alloys

Before validating the model from section 5.1 the influence of oxygen on the balling process will be briefly considered. It is, as mentioned in chapter 2, known that surface oxidation in some cases can be the cause of balling. The oxides of copper are stable until 1230 °C, and exists as a binary liquid until 1345 °C [103], which means that they could play a role, unlike for silver and gold where the oxide decompose at 200 and 160 °C respectively. To investigate this possibility virgin copper powder, never exposed to oxygen, was processed at three different oxygen concentrations; 0.01, 0.1, and 1 % at process conditions which cause balling defects to form: $P = 200\,\mathrm{W}$, $v = 200\,\mathrm{mm\,s^{-1}}$, $l = 40\,\mu\mathrm{m}$, and $h = 100\,\mu\mathrm{m}$.

Four samples were produced per oxygen level and cross-sectioned to measure the density, which based on section 5.1 is used as a proxy for the level of balling. One of the 1 % O_2 samples was lost during separation from the base plate. The relative density was measured from optical images of metalographical cross-sections. The samples were intened to be cross-sectioned through the middle, but the samples processed under 0.01 % oxygen were sectioned closer to the sample edge (roughly 1/4 through).

The measured cross-sectional relative densities, and the average per condition, are shown in figure 5.5. The average densities are close to each other but the variance is relatively high, especially for the 0.01 % O_2 sample. Due to the high variance it cannot be proven that there is no dependence on the oxygen concentration, but if such an effect exists it is small, and rather to increase the density. From this we can presume that the presence of oxygen is most likely a minor factor for the formation of balling, especially considering studies on gold alloys [70] and a recent study on copper power [56] showing improvement when using oxidized powders.

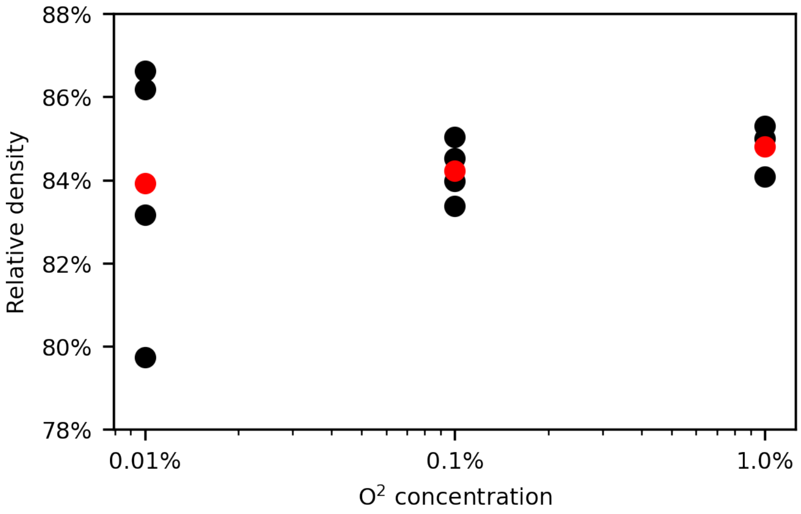

Figure 5.5 – Relative density for pure copper samples from a copper powder never exposed to air, at different chamber oxygen concentrations.

Table 5.1 – The scanning speed (v) and the corresponding Peclet number (Pe) calculated from the room temperature thermal diffusivity (D) for the different materials at the experimental conditions.

Material	$\boldsymbol{v}$	$\boldsymbol{D}$ ($\mathrm{m^2\,s^{-1}}$)	$\boldsymbol{Pe}$
Cu	$300\,\mathrm{mm\,s^{-1}}$	8.9×10^{-5}	0.22
Bronze	$100\,\mathrm{mm\,s^{-1}}$	2.1×10^{-5}	0.26
316L	$20\,\mathrm{mm\,s^{-1}}$	3.1×10^{-6}	0.30

Table 5.2 – Physical model parameters and the corresponding balling threshold.

Material	$\boldsymbol{T_m}$	$\boldsymbol{K}$	$\boldsymbol{\alpha}$	$\boldsymbol{P}_{\mathrm{Balling}}$
Copper	1356 K	$370\,\mathrm{W\,m^{-1}\,K}$	0.27	759 W
Bronze	1306 K	$77\,\mathrm{W\,m^{-1}\,K}$	0.36	121 W
316L	1708 K	$16\,\mathrm{W\,m^{-1}\,K}$	0.50	24 W

5.2.2 The porosity and melt pool width as a function of the balling number

To investigate the validity of the model developed in section 5.1 LPBF samples from pure copper, bronze, and 316L stainless steel were manufactured. The scanning speed was kept constant per material, corresponding to the same Peclet number of around 0.2, as outlined in table 5.1. The layer thickness was selected to produce a single layer of powder, 20 µm[1] , and the hatch was selected to be significantly below the expected wetting diameter at 70 µm. The scanning strategy was selected to be unidirectional to highlight the balling features.

The power was varied, for bronze and steel around the expected balling thresholds, and for copper as high as the laser source allowed (200 W).

In the parts fabricated from bronze and steel, the low-power samples show clear balling, which as the power is increased gradually transitions to lack-of-fusion porosity, and at high power the samples are near pore free. The transition from balling to conduction mode is shown for the bronze samples in figure 5.6, and is accompanied by a widening and flattening of the melt track. For the copper samples, which all had a relative density around 73 % to 75 %, the power was too low to cover the transition. A tightly packed ideal powder bed has a relative density of 74 %, which indicates that the samples are close to being in incomplete melting mode. This hypothesis is further supported by the size of the balling features which are typically around 70 µm. In some cases they are as small as 35 µm, meaning that uncoagulated powder is present.

Expressing the power in terms of the balling number allows the direct comparison of the results for the different materials. As the absorptivity values for the liquid alloys are not well studied and multiple reflections make the laser-material interaction complex, the metal absorptivity was selected as a free parameter. Good agreement with the experiments was found when $\alpha_{Cu} = 0.27$, $\alpha_{Bronze} = 0.36$ and $\alpha_{316L} = 0.50$, as tabulated in Table 5.2.

---

[1] Which is the amount of metal deposited by a tigtly packed single powder layer with 35 µm diameter powder.

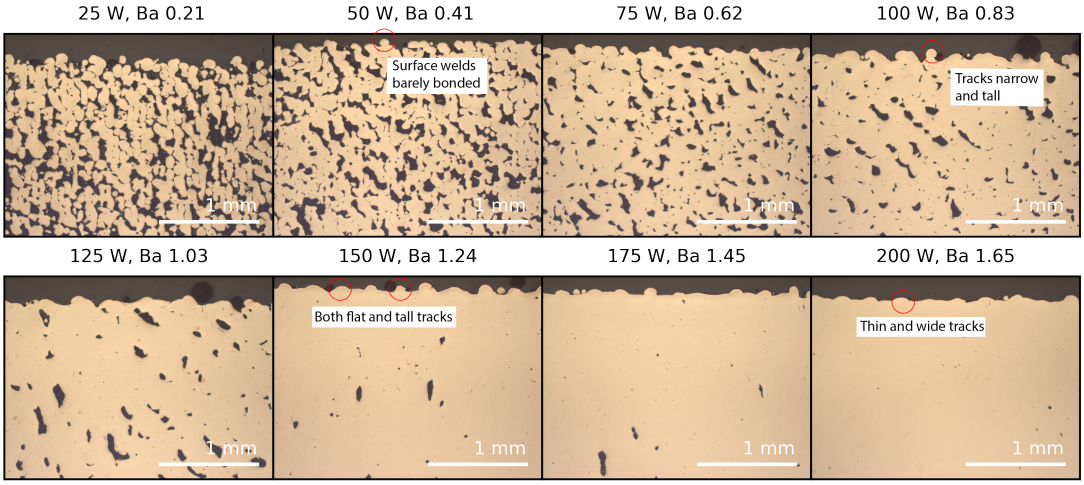

Figure 5.6 – Metallographic cross-sections of bronze samples processed at 100 mm s^{-1} at different power, covering the transition from balling to conduction mode.

The relationship between the balling number, Ba, the relative density, the wetted diameter, and the pore morphology is shown in figure 5.7 where the relative density is plotted as a function of the balling number. Two clear regions can be observed: below the balling threshold ($Ba = 1$) the density is increasing linearly, and above this value a plateau is reached. Least-square fitting of the data points[2] above and below the balling threshold yields two lines which intersect close to Ba=1. Almost completely dense samples (>99.9 %) is achieved above a balling number of 1.5. This corresponds, as shown by the calculation of cap height in 5.4, to the height of the cap being less than the powder diameter.

In figure 5.7, the wetted diameter is plotted as a function of the balling number together with the prediction by equation 5.7 and 5.10. Once the threshold for balling is exceeded, the predicted diameters of the melt tracks are often overestimated. The measured values are, however, in good agreement with the predictions according to equation 5.7. Equation 5.10 is valid when the weld track is wide and narrow, approximating a plate weld. Depending on the local powder density one would expect the wetting diameter to fluctuate as the melt is alternating between including the second and third neighbor lines. A larger variance in the measured wetting widths is indeed observed as around and above the balling threshold.

5.3 Simulation of the balling phenomenon

The model in section 5.1 is, in order to yield results on closed form, dependent on many approximations. For these approximations to be valid several conditions must hold true:

- The coagulation of powder particles into the melt is fast on the timescale of the melt

---

[2] Excluding the bronze samples with $Ba = 1.03$, which do not fit the general trend

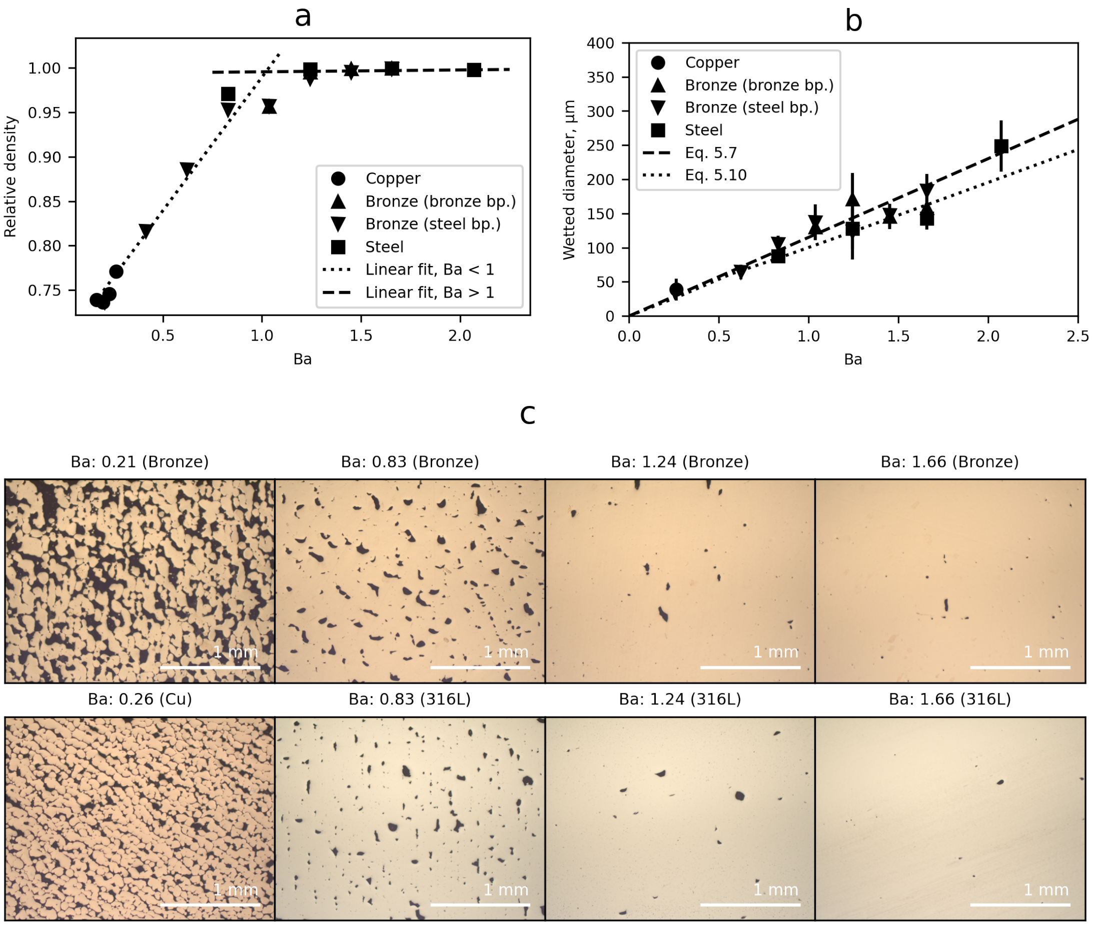

Figure 5.7 – The transition from balling to conduction mode expressed in terms of the balling number for the processed materials. (a) Relative density of the samples plotted against the balling number. The dotted and dashed lines are linear fits of the values below and above the balling threshold respectively. The two bronze data points right at the balling threshold were not included in the fit. (b) Average of the measured wetting diameter versus balling number. The solid line shows the 95 % confidence interval of the mean. The values predicted by equation 5.7 and 5.10 are overlaid. (c) Optical cross-sections showing that the pore morphology for different materials is similar at similar balling numbers.

pool to pass a point.

- The temperature field must rech steady state fast relative to time of the cap spreading on the surface.
- Fluctuations in the size of the melt pool must be large enough for the melt to reach the powder in the second neighbour line.

To verify these assumptions the balling process was simulated for bronze using the CFD model described in chapter 3.

The simulation was performed with a stationary laser illuminating a single layer of 45 µm powder tightly packed with a lattice parameter of 50 µm on a substrate. The powder was chosen to have a diameter smaller than the lattice parameter to ensure that the powder particles remain thermally isolated from each other. For the same reason the powder particles, were raised 5 µm from the substrate, except for the center particle. Due to the cubic voxels and the decreased powder size, the resulting total volume of powder is 27 % lower than a tightly packed bed.

The computational domain was made up of a cube of size $600 \times 600 \times 500\,\mu\mathrm{m}^3$, divided into voxels of $5 \times 5 \times 5\,\mu\mathrm{m}^3$ and reduced by symmetry planes to a quarter of $300 \times 300 \times 500\,\mu\mathrm{m}^3$. The boundary conditions on the non-symmetry faces were a fixed temperature of 300 K, no slip for the velocity field, and zero gradient for phase field. The simulation was performed using laser powers of 50 W, 100 W, 150 W, and 200 W. All simulations ran for a simulated time of 500 ms using dynamic time steps.

At 50 W power the simulations show a melt which is on the border between balling and incomplete melting: the neighbour particles are coagulated into the melt, but the melt pool just touches the substrate. This contradicts the results from section 5.1, where a melt pool in the substrate is predicted for this power. This can be explained by diffusion of the phase field, which is present even using the stable MULES solver. This diffusion increases the thermal conductivity next to the triple line, leading to an overestimation of the heat transport through the interface. At higher power, when the contact angle decreases this effect is much less pronounced, resulting in weld shapes which are more physical.

The coagulation time for the nearest neighbour is at 50 W quite slow, taking around 250 µs from the time when the melt reach the contact point (illustrated in figure 5.8). This time is significantly shorter at higher power, around 100 µs. Assuming a typical balling situation with a ball size of 100 µm we see that the speed needs to be below $400\,\mathrm{mm\,s^{-1}}$ or slower for the coagulation to occur before passing the powder particle. In conduction mode, where the process is much faster the corresponding speed is higher: $1000\,\mathrm{mm\,s^{-1}}$. This gives, together with the requirement that $Pe < 1$, a rough upper bound for at which scanning speeds the model in section 5.1 can be expected to hold.

As is shown in figure 5.9 there are large melt pool fluctuations present. The origin of these fluctuations is the momentum gained from coagulating the neighbor powder particles, leading to pariodic elongation of the melt. This fluctuation is by a good margin large enough to reach the second neighbor, motivating the use of $n = 2$ in the calculation of the cap shape with equation 5.12. Despite the large and fast fluctuations the melt front in the substrate follows the cap (figure 5.9 d), verifying that constraining the cap to the substrate melt edge is a good approximation.

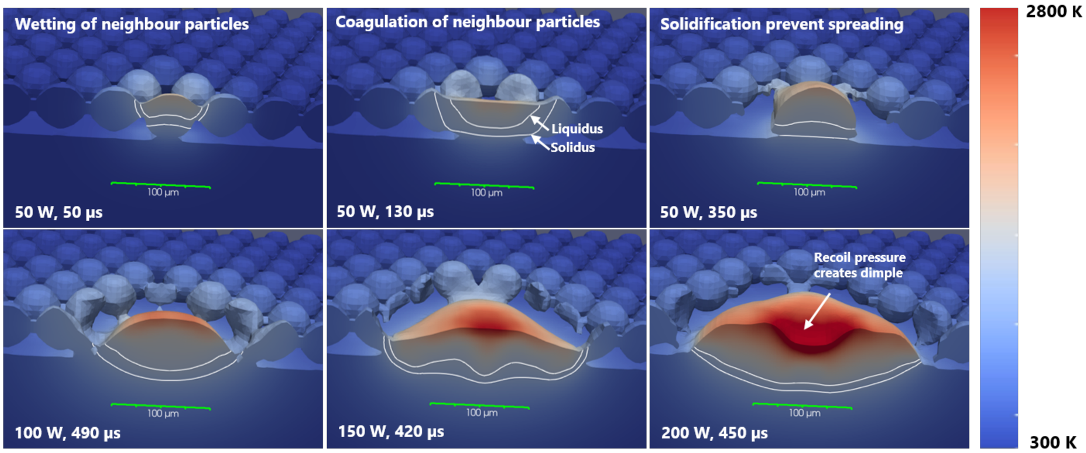
Wetting of neighbour particles
Coagulation of neighbour particles
Solidification prevent spreading
2800 K
Liquidus
Solidus
100 µm
50 W, 50 µs
50 W, 130 µs
50 W, 350 µs
Recoil pressure creates dimple
100 W, 490 µs
150 W, 420 µs
200 W, 450 µs
300 K

Figure 5.8 – Simulation of the balling phenomenon colored by temperature. The upper frames show the process of wetting and coagulation of the neighbor powder particles, and the formation of a ball at 50 W power. The lower frames show the shape at higher power.

5.4 Conclusions

In the previous chapter balling has been investigated. A simple analytical criterion for when balling occurs, valid at low scanning speeds for a single powder layer, was developed. The criterion states that the power needs to exceed the balling threshold of $25.5\frac{r_p K \Delta T_m}{\alpha}$, which is equivalent to a normalized enthaply of $8.4\sqrt{\frac{\pi}{Pe}}\frac{r_p}{a}$. This criterion corresponds to the wetting angle of the cap being 90° in a worst case scenario of a locally perfectly packed powder bed where all the powder particles have a the maximal diameter of the powder distribution, which occurs at a width of the substrate melt pool of 2.6 powder diameters. In case of thicker layers this value will be correspondingly higher.

Experimentally it was shown that below this power the amount of porosity increases rapidly in a linear fashion. Above the balling threshold some porosity is still remaining, but pore free samples are achieved as the melt width is approximately 3.7 powder diameters, which corresponds to the cap height being less than a powder layer. How far this observation correlates to the actual physical origin of these pores was not investigated, but it can be speculated that unevenness of the underlying substrate lead to perturbations which get worse with increasing layers.

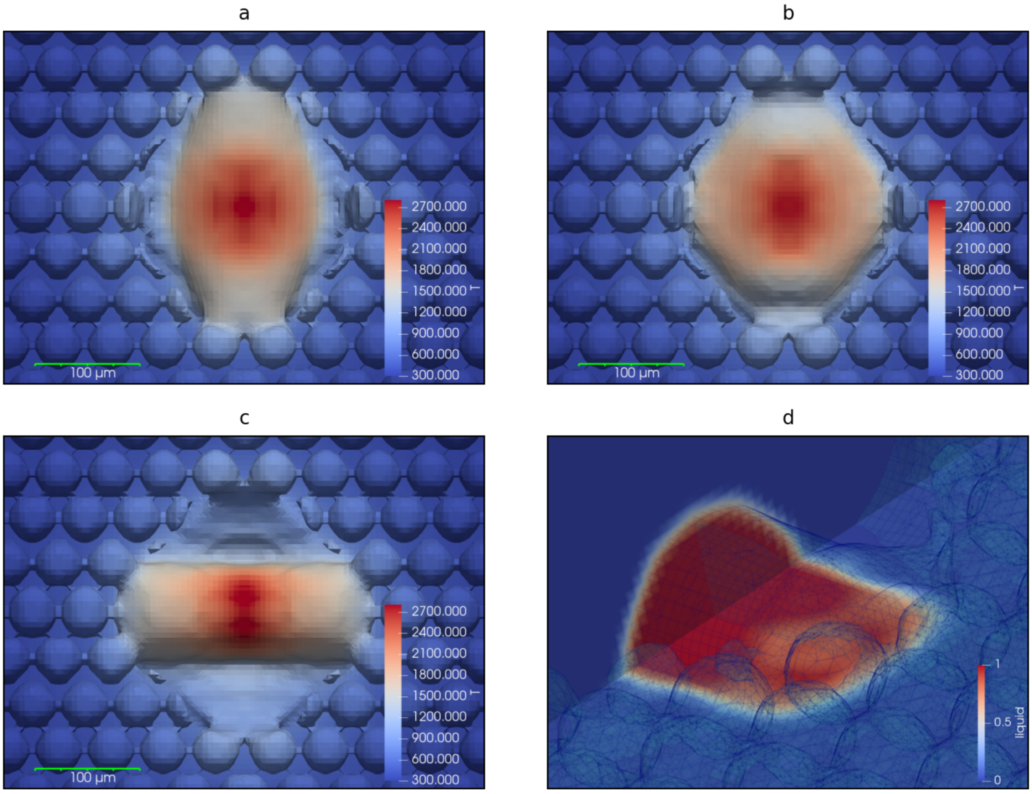
a
b
c
d
100 µm
2700.000
2400.000
2100.000
1800.000
1500.000
1200.000
900.000
600.000
300.000
T
1
0.5
0
liquid

Figure 5.9 – Fluctuations of the melt pool shape at 150 W. (a-c) The shape at different times colored by temperature. (d) The same simulation colored by the liquid phase fraction. The simulation domain is sectioned to show the symmetry plane and the substrate sufrace.

Below the balling threshold the widths of the melt agrees well with a model assuming uniform heat transfer across the cap-substrate interface. This is the type of heat source we expect in balling mode, where the cap is high and having a narrow contact point. In case of this type of heat source we further expect the depth-to-width ratio of the melt in the substrate to be constant at 0.23. Above the balling threshold the melt pool widths tend to fluctuate between values corresponding to uniform heat transport across the surface, and values corresponding to a heat source term approximating the laser heat source. This indicates that there is a physically observable transition in the melting mode occuring there. Taking this together with the sharp change in the relative density occuring at the transition point it can be concluded that it is motivated to distinguish the defects ocuring in balling mode from the defects occuring in conduction mode.

The reduction of balling pores can be achieved by modification of the terms in equation 5.16: Laser power, optical absorptivity, powder size, substrate and melting temperature, and thermal conductivity. The laser power is straightforward to adjust, but in many cases the maximal power of the available machine will already be reached. Substrate temperature can be increased by pre-heating, which is available in some commercial machines, but often limited by the mechanical challenges associated with high temperatures in the moving build piston. The powder size is interesting to decrease, but fine powders have poor flowability and reduction of the powder size requires a quadratic increase in build time as both the hatch distance and layer thickness needs to be scaled with the powder. Increased optical absorptivity is interesting, but in the absence of inter-band optical transitions the absorptivity is strongly correlated with the thermal conductivity, which for most applications related to group 11 metals should be kept as high as possible. In chapter 6 and 7 methods to circumvent this limitation and are explored: the processing of powder coated by more absorbing metallic coatings, and processing with a green laser source.

6 Powder coating as an alloying strategy for pore reduction

In chapter 5 we saw that the variables we can change to decrease the balling threshold are absorptivity, thermal conductivity, melting temperature, substrate temperature, and powder size. As briefly mentioned in chapter 2 the absorptivity and thermal conductivity of a metal are coupled as these processes all arise from transport and scattering of the electrons. In many applications increased thermal conductivity is undesirable, and it is interesting to consider methods of decoupling the absorptivity from thermal conductivity. One such possible strategy is to coat the feed-stock with the alloying element instead of pre-alloying the material. This will, as long as the powder stays solid, increase the absorptivity of the powder bed while keeping the resulting thermal conductivity at a level decided by the thickness of the powder.

The work is primarily based on the paper *Laser Powder Bed Fusion of Metal Coated Copper Powders* [88], but also unpublished related work. The experimental work was performed in close collaboration with Dr. Oleksii Liashenko, who participated in conceptualization of the study, performed SEM-analysis, and preparation of samples. X-ray tomography of samples was performed by Dr. Kai Zweiacker. The powder batches named *Coated Sn3.0* and *Coated Sn8.5* were produced at Cherkasy National University with the by Serhii Derevianko, Vladyslav Morozovych, and Dr. Oleksi Liashenko, under the supervision of Prof. Yurij Lyashenko. Measurement of the powder bed reflectivity was done by Dr. Yevhen Shynkarenko.

6.1 Immersion depositions for powder coating

One method for depositing metal on metal are so called immersion deposition coatings [50], these methods are driven by two reactions, a thermodynamically unfavorable redox reaction and a complexion reaction [74]. The redox reaction is on the form:

$$m\mathrm{A}^{n+}_{\mathrm{(aq)}} + n\mathrm{B} \xrightleftharpoons{\mathrm{K}_1} n\mathrm{B}^{m+}_{\mathrm{(aq)}} + m\mathrm{A} \tag{6.1}$$

where $\mathrm{A}^{n+}_{\mathrm{(aq)}}$ is the coating metal and B the metal being coated. Since the reaction in 6.1 is strongly driven to the left a complexation reaction is used to decrease the concentration of

$B^{m+}_{(aq)}$:

$$pB^{m+} + qC \xrightleftharpoons{K_2} B_p[C]_q{}^{m+} \tag{6.2}$$

The two steps of the reaction allows reaction 6.1 to proceed even when it is thermodynamically unfavorable, as the second reaction acts as a driving force according to Le Chatelier's principle. This makes it particularly suitable for coating of noble metals with less nobler metals, a reaction which per definition is thermodynamically unfavorable. Since there is no external voltage needed these reactions are furthermore suitable for powders, which would be difficult to coat by electroplating.

The copper-tin and copper-nickel systems are well studied and of high industrial interest, and in this work copper powder coated with these metals are investigated. The systems are at lower alloying concentrations forming solid solutions, but whereas nickel is soluble over the whole composition range the tin system is forming several intermetallics. Both nickel and tin have significantly higher optical absorptivity at 1064 nm (Ni 27 %[109], and Sn 19 %[37]) than copper (1 %[3]).

To perform the coating from tin and nickel salts reaction 6.1 becomes:

$$Sn^{2+}_{(aq)} + Cu \xrightleftharpoons{K_{Sn}} Cu^{2+}_{(aq)} + Sn \tag{6.3}$$

$$Ni^{2+}_{(aq)} + Cu \xrightleftharpoons{K_{Ni}} Cu^{2+}_{(aq)} + Ni \tag{6.4}$$

The standard half-cell electrode potentials of these reactions are summarized in table 6.1 together with the equilibrium coefficients calculated from the Nernst equation:

$$\ln K = \frac{zFE^0}{RT} \tag{6.5}$$

where z is the number of electrons transferred in the reaction (2 in the reactions above) and $F = 96485\,\mathrm{C\,mol^{-1}}$ the Faraday constant. The equilibrium constant is extremely small, meaning a very strong complexation reaction is necessary. Traditionally cyanides of various kinds are used [9], but in this work the safer and more environmentally friendly [9] thiourea ($CS(NH_2)_2$), which is known to work well for these types of reactions [74, 50] is chosen.

The complexation reaction of copper with thiourea is complex, consisting of many competing reactions with complicated kinetics [28]. Depending on the reaction conditions one can thus expect different reactions to be dominating, and different mechanisms have been proposed. It is however generally accepted [74, 76, 78, 77] that the following two step reaction takes place:

$$Cu_2{}^+ + 2CS(NH_2)_2 \rightleftharpoons Cu^+ + (SC(NH_2)_2)_2{}^+ \tag{6.6}$$

$$Cu^+ + 4CS(NH_2)_2 \rightleftharpoons Cu[CS(NH_2)_2]_4{}^+ \tag{6.7}$$

The stability constant of this complexation reaction has been reported in the range $1 \times 10^{15.4}$ to $1 \times 10^{18.1}$ [77].

Table 6.1 – The half cell reactions for the coating reactions with their standard potential, E°, and the corresponding equilibrium constants K for the oxidation of copper to copper(II) calculated from the Nernst equation.

Reaction	E°	**K for reduction of Cu**
$Sn_2{}^+ + 2e^- \rightleftarrows Sn$	$-0.13\,V$	1.5×10^{-16}
$Ni_2{}^+ + 2e^- \rightleftarrows Ni$	$-0.25\,V$	5.2×10^{-21}
$Cu_2{}^+ + 2e^- \rightleftarrows Cu$	$+0.34\,V$	-

6.1.1 Coating of powder

Several batches of tin and nickel coated powder were prepared for LPBF processing. These powders are summarized in table 6.2 together with detailed recipes. The smaller batches were not LPBF processed, and are named after the coating and batch number; for example *Coated Ni Test 1* is a small test batch of nickel-coated powder. The larger batches were LPBF processed, and are named after their coating and composition; for example the powder named *Coated Sn0.8* is coated with tin, having a composition of 0.8 wt.% measured after LPBF processing from part cross-sections[1].

The coating procedure, shown in figure 6.1, involves first the deoxidation of the copper powder in solution 1 (which contains Thiourea and hydrochloric acid) turning the powder from red orange to pink. As solution 2 containing the salt of the metallic coating is added the coating process starts immediately and within a minute the powders have become completely coated, as indicated by a darkening of the powder. With a few exceptions the coating procedure is allowed to react for up to a few minutes, leading to the reaction being limited by the availability of uncoated copper. This means that the nucleation mechanism becomes important for the thickness of the coating, with a high nucleation rate with respect to the growth rate, leading to a thin and even surface. In the opposite situation, where the growth is fast with respect to the nucleation rate we can expect a rough, but thicker surface, as shown in studies of immersion deposition of tin where the presence of impurities can cause a rough surface [51]. From the electrodeposition literature it is also known that the concentration of the ions to be deposited affects the nucleation process, with a low concentration leading to a more dominating nucleation [39, 116].

In figure 6.2 a) the surface of powders coated in a low (0.8 mM), medium (11 mM, added dropwise in a solution with limited amounts of $Sn_2{}^+$) and high (76 mM) concentration of $SnCl_2$ is visualized together with their reflectivity spectra. The low concentration solution leads to a very fine pillow like structure, shown cross-sectioned in detail in figure 6.2 b), whereas the high concentration solution yields a uniform and smooth surface. The intermediate sample is not completely covered as there was not enough tin to completely coat the powder, leading to the nucleation sites being clearly visible. The surface roughness has a big influence on the powder reflectivity, with the smooth powder being more reflective and the rougher more absorbing. In

---

[1] The value after processing is chosen as it is both the easiest to measure, and the relevant property for the final parts.

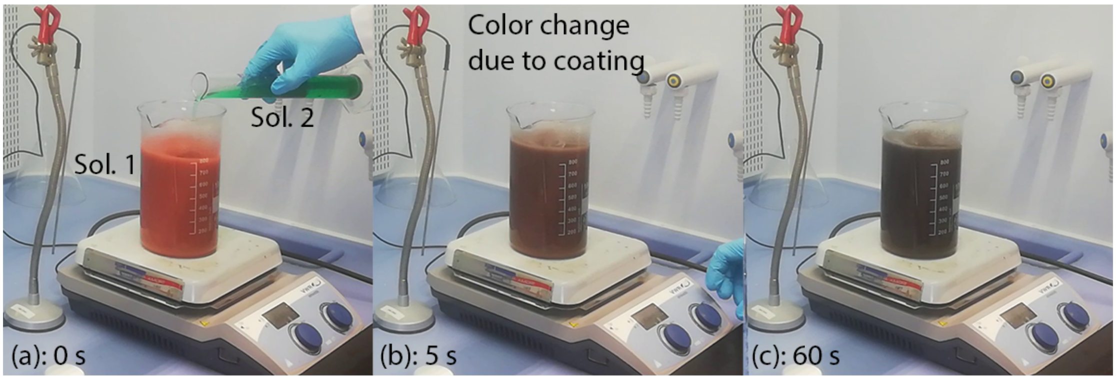

Figure 6.1 – The nickel coating process. (a) Addition of solution 2 to to the mixture of solution 1 and copper powder. The bright orange color indicates that the oxide layer has been dissolved. (b) After 5 s color change indicates that the coating process has started. (c) After 60 s no further color change is seen, and the coating process has finished.

the IR-range the powders are always more absorbing than the bronze, and considerably more absorbing than the copper powder. Since tin has no inter-band transitions in the visible range the smooth sample is more reflective in the visible range. The partially coated powder does show an increased absorptivity in the visible range, which is from the bare copper.

Similarly the morphology is also strongly influenced by the concentration of thiourea. This is particularly important for coating with Nickel, because the much lower chemical equilibria means that a higher thiourea concentration is needed to drive the reaction. In figure 6.3 the powder of the batches *Coated Ni test 1, 2, & 3*, with a thiourea concentration of 5.1 M, 2.5 M, and 1.3 M respectively is shown. It is clearly seen that the powders with high thiourea concentration have large voids forming in the powders. Such voids are undesirable as they could remain in the manufactured part, similar to gas porosities. A similar effect was seen in the tin-coated powder *Coated Sn 8.5*, which was manufactured with a high thiourea concentration. This powder has, as will be shown in the next section, worse surface morphology, but a higher tin concentration than the other tin-coated powders.

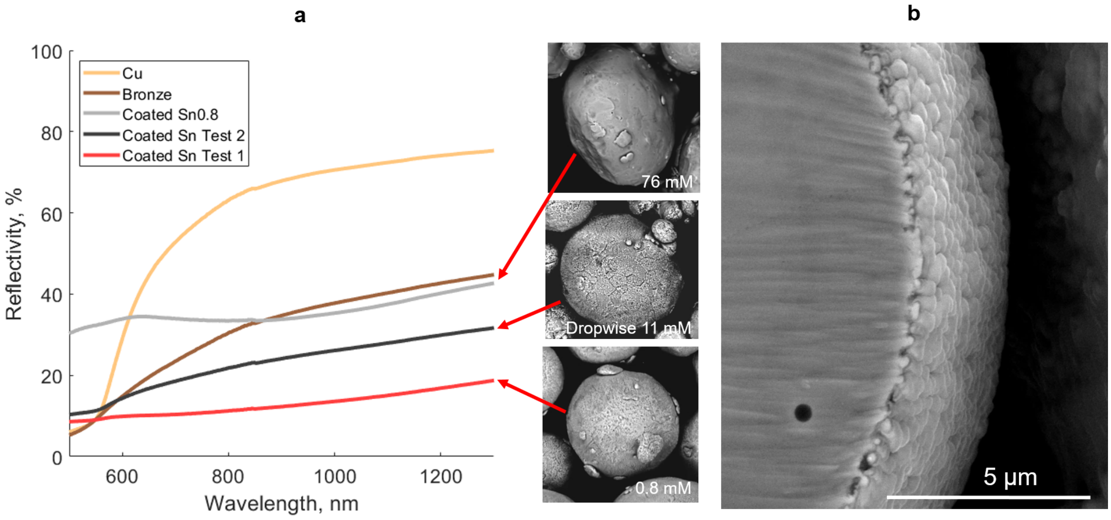

Figure 6.2 – The morphology of Sn-coated copper powder and the corresponding reflection spectra at different concentrations of Sn_2^+. b) Cross-section of the powder coated in a 0.8 mM Sn_2^+-solution.

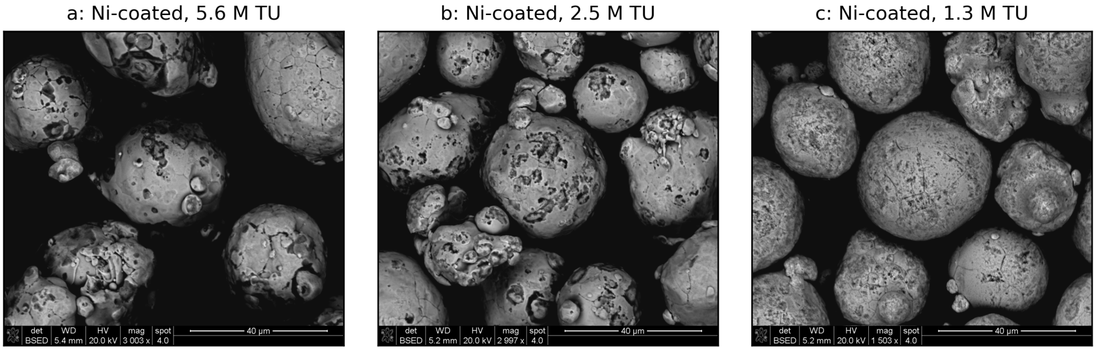
a: Ni-coated, 5.6 M TU

b: Ni-coated, 2.5 M TU

c: Ni-coated, 1.3 M TU

Figure 6.3 – The coating morphology of nickel-coated copper powders with different thiourea concentrations: a) Coated Ni test 1, b) Coated Ni test 2, and c) Coated Ni test 3.

Table 6.2 – Detailed recipes for coating of copper powders. “C” designates the coating, either Sn or Ni, “AS” indicates the method for addition of salt: dropwise (D), or all at once (A). The “P” column indicates where the powder was produced, at Empa (E) or at Cherkasy National Laboratory (C). *) Made in several small batches of 25 g. **) Made using H_2SO_4 instead of HCl.

	C	$\mathbf{m_{powder}}$	$\mathbf{V_{sol}}$	$\mathbf{T_{RXN}}$	$\mathbf{t_{RXN}}$	$\mathbf{c_{TU}}$	$\mathbf{c_{Acid}}$	$\mathbf{c_{Cation}}$	**AS**	**P**
C Sn0.8	Sn	103.86 g	0.8 L	43 °C	1.5 min	0.41 M	0.40 M	76 mM	A	E
C Sn3.0	Sn	100 g	1.0 L	64 °C	20 min	0.66 M	0.3 M**	21 mM	A	C
C Sn8.5	Sn	25 g*	1.0 L	60 °C	20 min	1.1 M	0.3 M	21 mM	A	C
C Ni1.5	Ni	120.44 g	0.8 L	52 °C	2.5 min	1.64 M	0.12 M	70 mM	A	E
C Ni1.9	Ni	120.47 g	0.8 L	50 °C	2.5 min	1.64 M	0.08 M	70 mM	D	E
C Ni2.4	Ni	200.25 g	2.0 L	52 °C	3 min	1.60 M	0.20 M	47 mM	D	E
C Sn Test 1	Sn	9.996 g	0.5 L	40 °C	<1 min	0.34 M	0.42 M	0.8 mM	A	E
C Sn Test 2	Sn	150.04 g	0.8 L	42 °C	3 min	0.40 M	0.40 M	11 mM	D	E
C Ni Test 1	Ni	9.96 g	0.05 L	51 °C	1 min	5.06 M	0.31 M	170 mM	A	E
C Ni Test 2	Ni	10.00 g	0.1 L	50 °C	1 min	2.53 M	0.31 M	85 mM	A	E
C Ni Test 3	Ni	10.00 g	0.2 L	50 °C	1.5 min	1.27 M	0.31 M	43 mM	A	E

6.2 LPBF of coated powders

That the powders increase the absorptivity is no guarantee that the balling threshold will be reduced any further than it would have with a pre-alloyed powder of the same composition. This is dependent on how fast the coating dissolves and mix, if the laser outruns the melt, and if secondary reflections illuminate the coated powders ahead of the melt. To verify if the powders increase the coupling between the laser and the melt pool LPBF samples were manufactured from coated, and uncoated powders, and the results compared.

6.2.1 Characteristics of powders used for laser powder bed fusion

For comparing the coated powders to uncoated powders it was decided to coat the powders in high concentration solutions as this allows the manufacture of amounts of powder in the range 100 g to 200 g in one single batch at small scale laboratory conditions. The flowability of all powders was good, corresponding to between 1 (very good flowability) and 2 (sufficient flowability) on the optical evaluation method proposed by Spierings et al. [127], and a smooth powder layer was achieved upon deposition on the build plate.

The nominal compositions of the samples after L-PBF are shown in 6.4 together with the measured optical reflectivities of the powders at a wavelength 1064 nm. The compositions vary from 0.8 wt.% to 8.5 wt.% but the reflectivity is uniformly around 40 %, similar to that of the bronze powder, but independent of the total composition.

A simple expression for correlating powder absorptivity (α_{powder}) with the flat surface absorptivity (α) has been found by Boley et al. [6] to be:

$$\alpha^{H}_{powder} = 0.0889 + 2.73\alpha - 5.06\alpha^2 + 4.29\alpha^3 \tag{6.8}$$

$$\alpha^{G}_{powder} = 0.0413 + 2.39\alpha - 3.36\alpha^2 + 4.50\alpha^3 \tag{6.9}$$

for hexagonally close packed powder (H) and powder distributed according a Gaussian distribution (G). In figure 6.5 the values predicted by these models are shown together with experimental data provided by Boley et al. and the measured values for the coated powders plotted against literature values for normal reflectivity. The experimental values all show a somewhat higher absorptivity than the values predicted by the model, but the tin-coated samples and the pure copper powder are especially underestimated by the model. In the case of copper the formation of oxides on the surface is a likely source of the difference, but in the case of the tin-coated powder it is more unclear, possibly stemming from surface contamination.

As shown in figure 6.6, the surface of the powders *Coated Sn0.8*, *Coated Ni1.5*, and *Coated Ni1.9* were very smooth, *Coated Sn3.0* had a somewhat rougher surface, and *Coated Sn8.5* had a very rough and uneven surface which was also poorly bonded. The rougher surface, thicker coating, and poor bonding is well explained by the, for tin, high concentration of thiourea as well as a lower concentration of tin ions. It is also noticeable that the *Coated Sn3.0*-powder

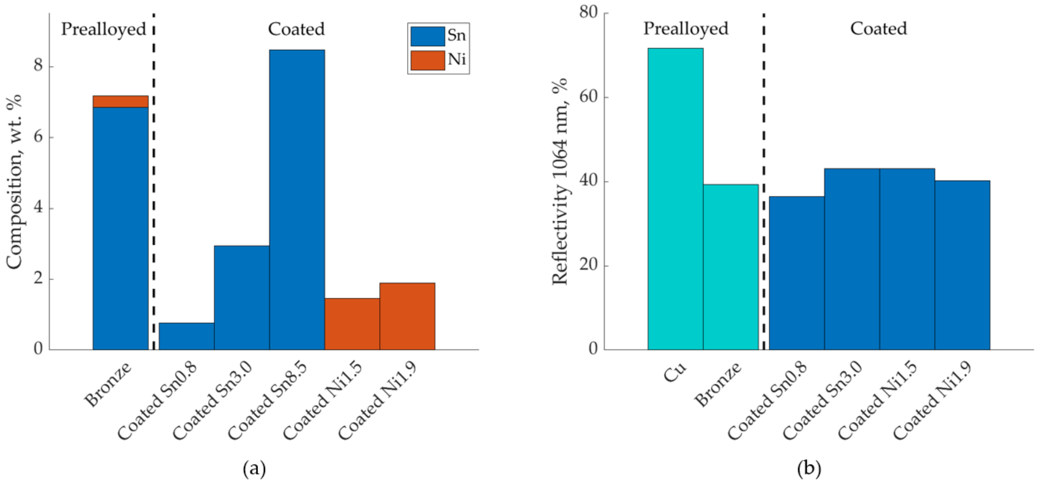

(a)

(b)

Figure 6.4 – . (a) Composition of the coated powders after LPBF processing measured by X-ray fluorescence of cross-sectioned and polished samples and (b) optical reflectivity of the powder bed at 1064 nm for coated and non-coated powders.

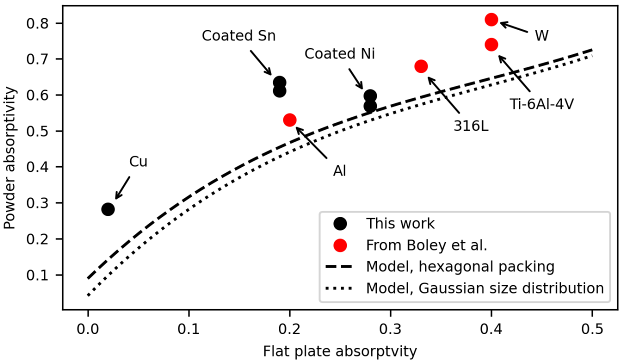

Figure 6.5 – Comparison of the absorptivity predicted by Boley et al. with the measured values of the coated powders.

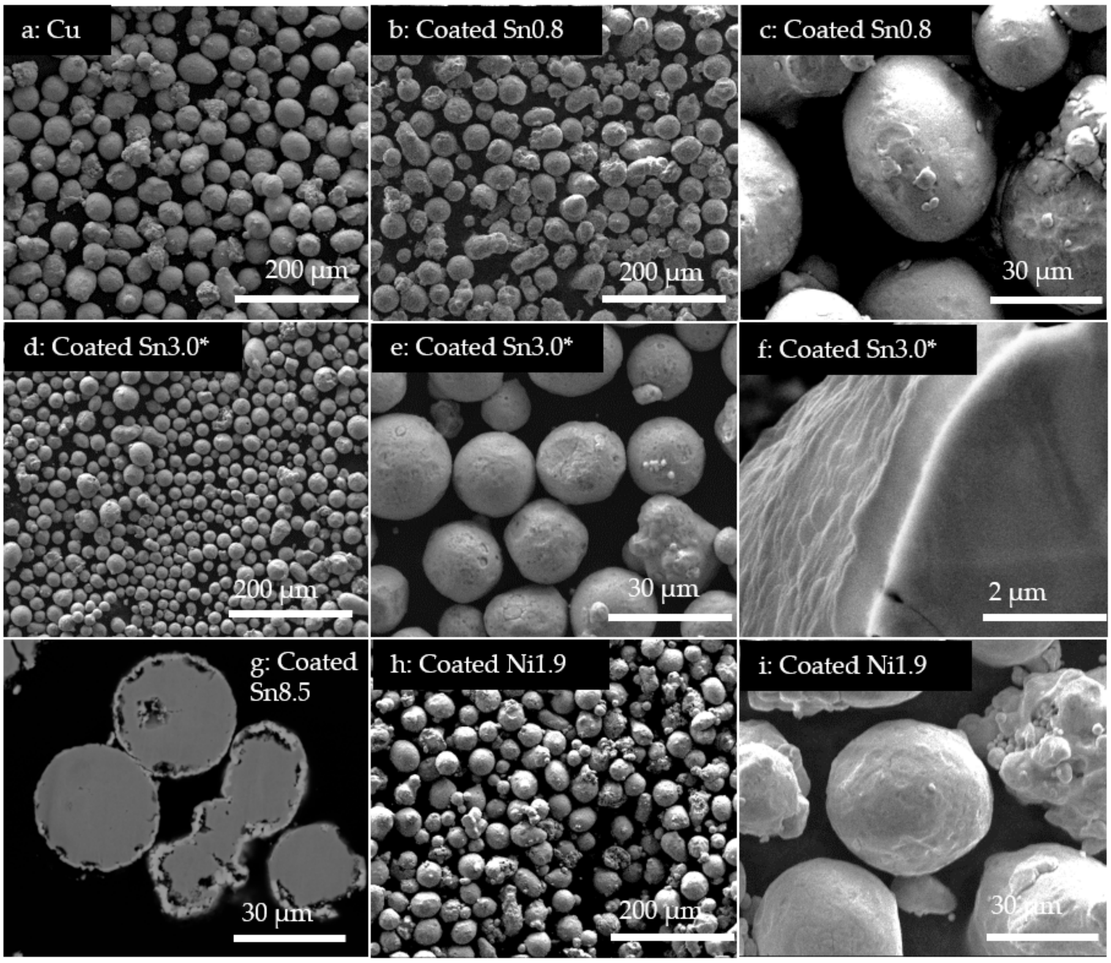
a: Cu
200 µm
b: Coated Sn0.8
200 µm
c: Coated Sn0.8
30 µm
d: Coated Sn3.0*
200 µm
e: Coated Sn3.0*
30 µm
f: Coated Sn3.0*
2 µm
g: Coated Sn8.5
30 µm
h: Coated Ni1.9
200 µm
i: Coated Ni1.9
30 µm

Figure 6.6 – SEM images of the coated powders. (a) Pure Cu powder; (b-c) Coated Sn0.8 and (d-f) Coated Sn 3.0*, a batch of powder produced with the same method as Coated Sn.3.0. The coatings of the two powders are comparable in thickness, and morphology.; (g) cross section of Coated Sn8.5, with pores below the coating and (h-i) Coated Ni1.9.

had a significantly smaller powder diameter than the other powders, something which could not be explained by the reaction conditions.

6.2.2 Comparison of LPBF of coated powders with powder mixtures

As the powder melts, the coating will dissolve and mix with the rest of the powder. When this mixing has occurred there is no real difference between a prealloyed powder, a mixture of powders and a coated powder, as long as the composition is the same. Thus the benefit of the coated powders is dependent on the laser light shining on solid, or recently molten, powder. To test if the powder adds benefit beyond the decreased thermal conductivity contributed by the alloying LPBF of the coated powders were compared to the the copper and bronze powders mentioned above. Mixtures of the copper and bronze powder at ratios 1:1 (with an overall composition of 3.35 % Sn and 0.15 % Ni), and 3:1 (1.68 % Sn and 0.075 % Ni) were also processed. All powders, except for *Coated Sn8.5* which was processed at 200 W, were processed at 175 W, with a layer thickness of 40 µm and a hatch distance of 100 µm. The scanning speed was varied from 25 mm s^{-1} to 900 mm s^{-1}. Two types of samples were produced, cylinders of diameter and height 5 mm and cubes of side 5 mm. The cylinders were analyzed by X-ray tomography, and the cubes by metallographic cross-sections.

The relative densities of the non-coated reference powders of copper, bronze and blends thereof, are plotted in 6.7 a), together with a linear fitting of the relative density serving as a visual guide, without any physical significance. The porosity was decreasing with an increasing amount of tin, as expected from the corresponding decrease of thermal conductivity. The samples made from the bronze powders and the powder mixtures exhibit a low dependence on the scanning speed. This is, as discussed in chapter 5 expected due to the low Péclet number, below 2 for all samples, for these materials at this scanning speed. For the copper samples the relative density is constantly below 70 %, which is lower than a tightly packed powder bed. Above 400 mm s^{-1} the relative density further drops off quickly. This is the same speed predicted by the simulations in section 5.3 at which the laser passes a powder particle before it has time to coagulate with a neighbor.

In figure 6.7 b) and c) the relative densities of the tin and nickel-coated samples are plotted. For easy comparison the linear fitting curves of figure 6.7 a) are added. The same general trends seen in the non-coated powders are present for these samples: increasing alloying increase relative density, and the dependence on scanning speed is relatively low. For the tin-coated powders, which can be directly compared to the non-coated powders, it can be seen that the relative density is much higher than the mixtures, at the same time as the Sn-concentration is lower.

As was shown in chapter 5 the relative density can in balling mode be used as a proxy for the coupling since the relative density is linear as a function of the balling number. Because of this the experiment shown above is a strong indication that coating reflective powders with a more absorbing coating increases the absorptivity, which is in agreement with other recent studies on coated and surface treated copper powders [54, 53, 56, 55]. The mechanism of the increased coupling is, however, not explained by these experiments, but a hypothesis which will be studied further in chapter 7 is that multiple reflections get directed on the surrounding non-molten powder which in turn gets preheated. It can be shown that preheating material is equivalent to increasing the power by a factor [114]:

$$\frac{\Delta T_M}{\Delta T_M - \Delta T_0} \tag{6.10}$$

where ΔT_M is the temperature difference between melting and substrate temperature without preheating, and ΔT_0 the increase in substrate temperature from the preheating.

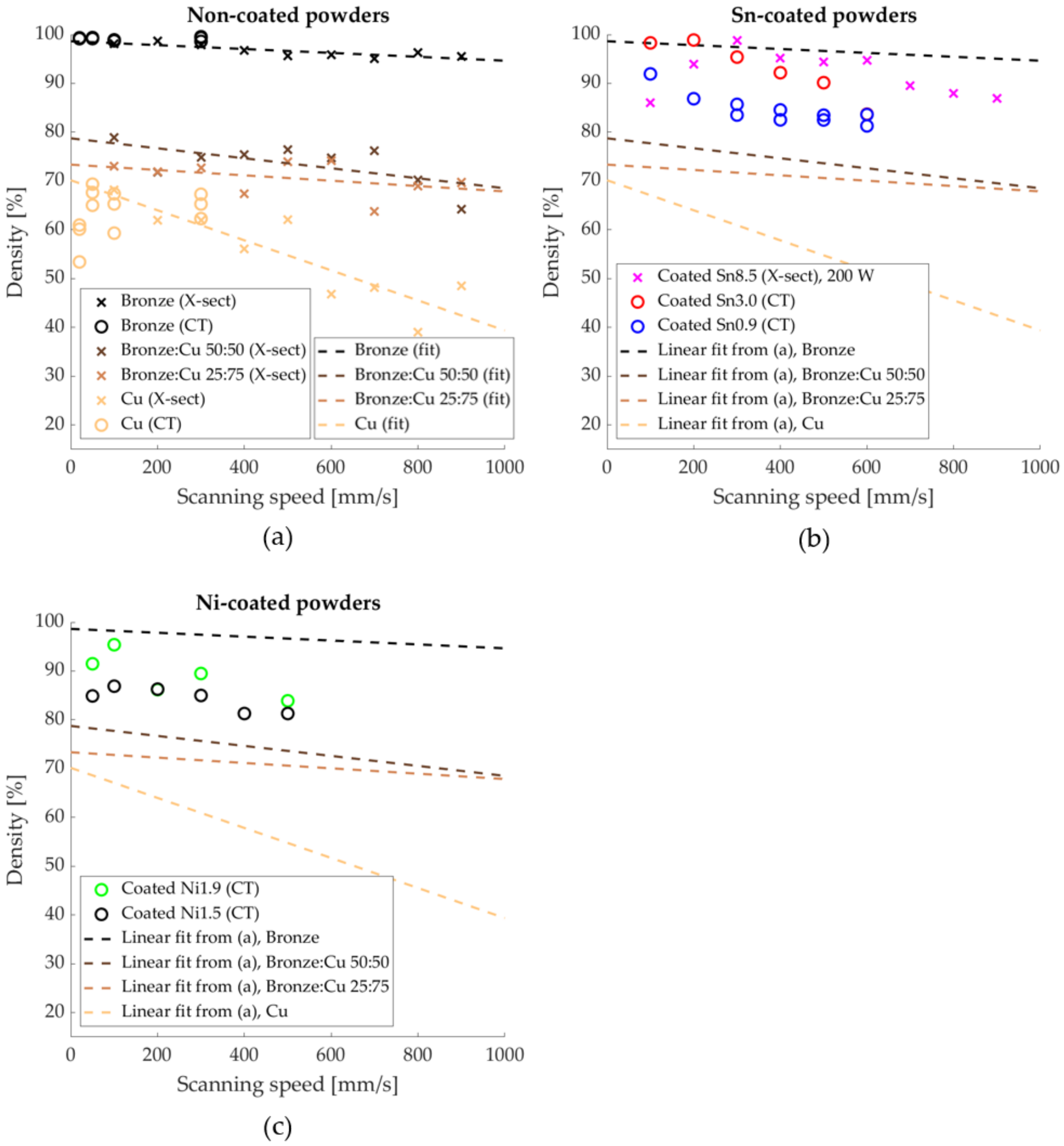

(a) (b) (c)

Figure 6.7 – Relative densities of printed samples as measured by computer tomography (o) and metallographic cross-sections (x). The dashed lines are linear fits of the density of the uncoated powders to serve as a common visual guide in all three graphs, without implying any underlying physics. a) Non-coated and blended powders; b) Sn-coated powders and c) Ni-coated powders. Note that the porosity of Coated Sn8.5 was measured by optical cross-sections, and was processed at a higher power than the other samples.

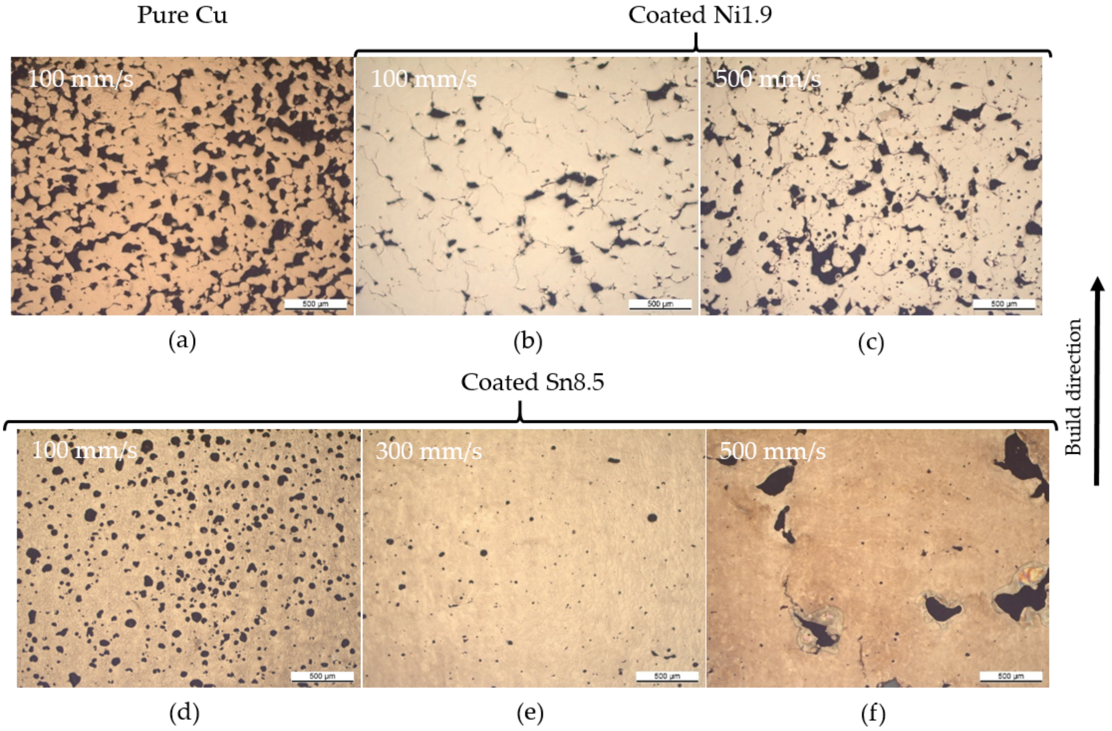

Figure 6.8 – Optical cross-sections of samples produced from coated powders and pure copper. (a) Uncoated pure copper processed at 175 W where the balling type porosities are evident. (b,c) Coated Ni1.9 where the porosity is reduced with respect to pure copper. (d,e) Coated Sn8.5 processed at 200 W, with spherical pores in the high energy density regime, large irregular pores in the low energy density regime and a relatively dense sample in the middle.

6.2.3 Pore morphology

The pores in the samples have varying morphology across the different powders used, as shown in the optical cross-sections in figure 6.8 and the computer tomograms in figure 6.9. The copper samples shown clearly exhibits balling porosity, but there are areas with almost no metal, which would indicate that the powder in those regions were not completely molten, particularly at a scanning speed above 400 $\mathrm{mm\,s^{-1}}$. The tomograms on the other hand show no loose powder in the pores. Since these samples were not cross-sectioned any non-molten powder would be visible, showing that all powder in these samples was molten.

The coated powders exhibit pores of different geometries. For the powder with the thickest coating, Coated Sn8.5, the pore morphology was dependent on the scanning speed, with low scanning speed leading to a high degree of spherical pores, and higher scanning speed leading to the appearance of large irregular pores. In-between these extremes an operating window leading to low porosity levels could be found. The dependence on the scanning speed is much larger than for the bronze sample, which has a similar composition and thus could be expected to behave similarly.

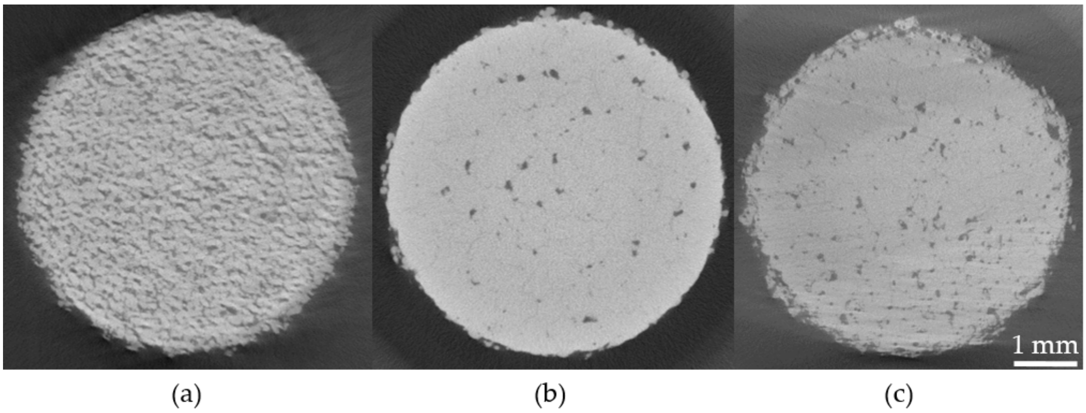

(a) (b) (c)

Figure 6.9 – X-ray computer tomograms of (a) pure copper cylinder, (b) Coated Sn3.0 and (c) Coated Ni1.9. The cracks in the samples made from the coated powders are visible and no loose powder is found in the pores. All tomograms are from samples produced at $100\,\mathrm{mm\,s^{-1}}$ scanning speed.

6.2.4 Occurance of cracks

In the samples manufactured from coated powders large cracks are forming in the build direction. These cracks, which are seen in figure 6.8 and shown in more detail in figure 6.10, go straight through the center line of the weld and have dendrites typical of solidification cracking. Residual sulfur from thiourea has been identified by Jadhav et al. [55] to be the cause of solidification cracking in LPBF of tin coated copper powders, and is a very likely candidate to be the element responsible for the cracks.

To investigate if these cracks can be reduced by changing the process parameters a new batch of coated nickel powder, with 2.4 wt.% Ni, was produced and used to manufacture a part. A steel base plate was chosen instead of the bronze base plates used above, and before processing it was pre-heated using the laser. The delay between the different layers was minimized by making only one sample, and total heat input was increased by re-scanning the sample. These parameters were selected to increase the temperature of the base plate, and thus reducing the residual stresses.

An optical image of the upper and lower part of the sample is shown in figure 6.11. The lower part is almost crack free, whereas the upper part exhibits cracks of similar morphology to the ones in figure 6.8. This is most likely due to a higher temperature as the sample is in the zone of thermal influence of the low thermal conductivity base plate, and shows that the cracking can be reduced by controlling the temperature field of the sample.

6.2.5 Conclusions

The coating method presented above yields a smooth and complete coating of the powder. At the same time, it is simple, cost efficient and scalable. The powders retain good flowability

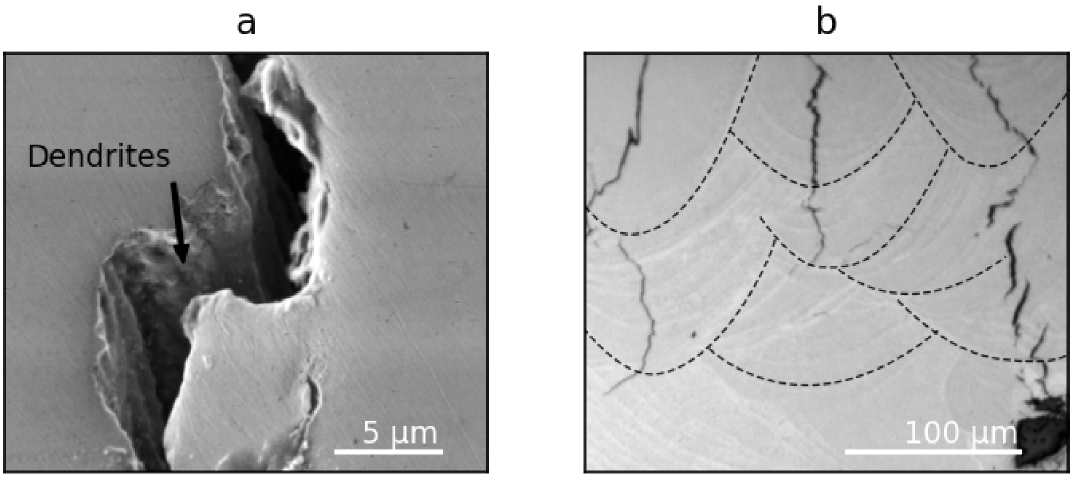

Figure 6.10 – Morphology of the cracks found in the samples made from coated powders. (a) SEM image of *Coated Sn3.0* where the dendrites typical of solidification cracking are seen on the crack surface. (b) Cracks in *Coated Ni1.9* with the melt pools outlined. The cracks pass through the center of the melt pool, which is also typical of solidification cracking.

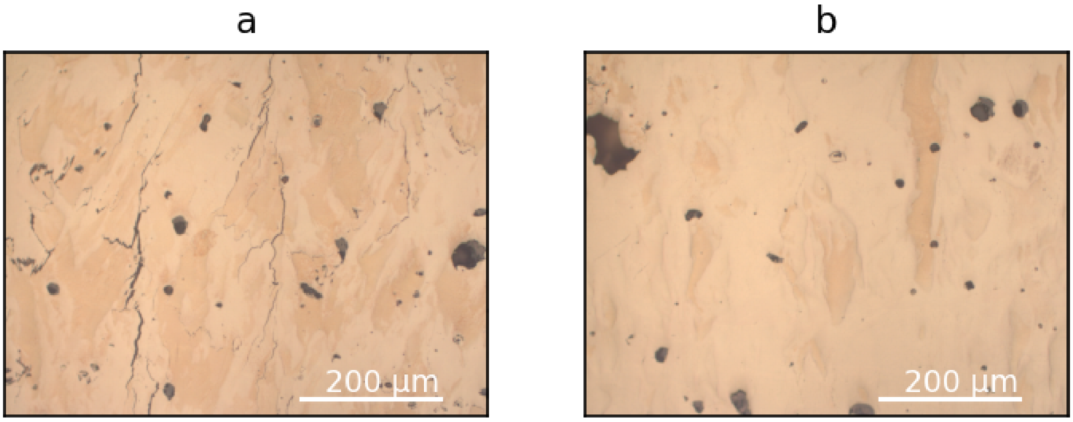

Figure 6.11 – Sample manufactured with a high total heat input to reduce cracking. (a) Upper part, with cracks. (b) Lower part, without cracks.

after the coating, which is important for L-PBF applications. The comparison of the samples fabricated from coated, non-coated powders and the powder blends show that coating powders with a thin metal coating of tin decreases the porosity of the built samples, in comparison with the non-coated powder blends of similar compositions. The nickel-coated copper powders achieve a similar relative density as the tin-coated powders. It can be assumed that the achieved density is also better than what would have been achieved with prealloyed alloys of similar composition since nickel, in copper at the relevant compositions, behaves similarly to tin.

The use of the coated powders however lead to few processing issues. The relative density of the samples is dependent on scanning speed much more than the Cu-6.7 wt.%Sn-0.3 wt.%Ni bronze achieving the same density, meaning that the use of such powders requires a much more careful parameter optimization. There is also a formation of cracks, most likely due to contamination from the coating bath leading to solidification cracking It was however shown that the crack formation can be significantly reduced by process optimization.

The reduced porosity is assumed to be due to the increased surface absorption from the powder. This increased absorptivity will increase the overall heat input, widening the melt pool, leading to the transition from balling to conduction mode melting. The results strongly suggests that the absorption in the solid powder plays an important role for the heat balance of the melt pool. This complex interplay is difficult to capture by simple analytical models and numerical models which do not explicitly treat the coagulation and melting of powder. The interaction of the laser light with the powder is studied further in chapter 7, with a focus on green light which due to its very high absorption in the solid can be expected to behave similarly during LPBF processing to coated powders.

7 Processing of copper with green laser

In the previous chapter, a method for decreasing the amount of balling defects by increasing the optical absorptivity with metallic coatings was presented. This approach is useful when the desired material is an alloy with low concentration of alloying elements, but less useful for applications where high purity copper is needed. In this chapter another approach to increase the absorptivity is explored: Using a green laser source instead of the typical NIR-laser.

The exact absorptivity for both IR and green laser of copper during LPBF conditions is not known. For IR-light, the behavior at elevated temperature is not well studied, and multiple reflections complicates the situation for all wavelengths of the laser source. For the solid material it can however be expected to fall in the range of 4 to 40 times more absorbing, and for the liquid around 2.5 to 4 times more absorbing. The balling threshold can therefore be expected to be lowered significantly with a green laser in all situations. The benefit of the green laser will, as illustrated in figure 7.1 be amplified if the laser is illuminating solid. Simulations of keyhole mode melting have shown that most of the light will get trapped in the keyhole, leading to all energy being absorbed in the liquid phase [81], but other studies and the experiments with coated powders presented in the last chapter indicate that this is not the case in conduction and melting mode.

In this chapter the laser melting of copper is studied numerically and experimentally, both with and without powder. The focus of the studies is to answer where the laser light is shining, on solid or on liquid, in different processing situations. Studying this will help giving guidance to during which situations a green laser is the most useful. The work is partially based on unpublished results and partially on results which were presented at the Materials Science and Engineering Congress 2020 [138]. The experimental work on laser welding using combined IR and green lasers was done in close collaboration with Sayedpayam Vahdati, formerly at EPFL, and with the help Dr. Seth Griffiths, who assisted with FIB and SEM analysis. The single line scans of copper and bronze powder was done with the help of Dr. Tri Le Quang and Dr. Xiao Jia at Empa.

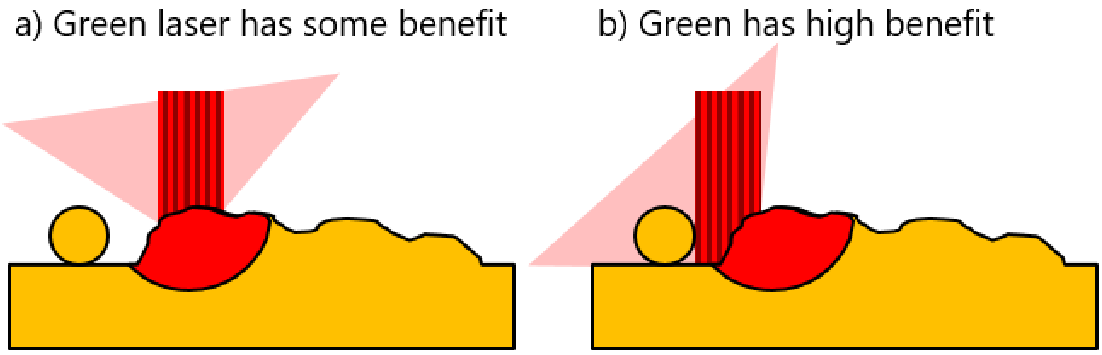

Figure 7.1 – Two hypothetical situations where a) the laser shines on liquid only, and b) where the laser is shining on liquid. In both situations the green laser will increase the heat absorption compared to an IR laser, but the latter case the effect will be much more pronounced because of the high solid absorptivity of the green laser in the solid.

7.1 Laser welding of copper

Before moving on to LPBF, the less complex case of laser welding is investigated. In comparison with laser welding, LPBF exhibits the repeated formation of melt tracks, and the presence of powder. Methods similar to the ones used in this thesis for LPBF have been used for improving the laser-material coupling in laser welding [45, 31, 129], and it is therefore interesting to study the mechanisms of coupling to see which techniques from welding can be used to improve LPBF and vice versa. Laser welding is also very similar to laser re-scanning, which has proven to be an important technique for improving the surface quality, making it possibly very important for high quality LPBF-processing.

In this section laser welding of copper with a green laser instead of an IR-laser is studied using fluid dynamics simulations. Based on the results a method for welding copper at low power with a combined IR and green laser source is presented. The method allows the formation of fine IR-welds of pure copper at a power as low as 150 W, with a 50 µm spot size and a scanning speed of 2.5 $\mathrm{mm\,s^{-1}}$.

7.1.1 Theoretical laser welding processing maps

Initially the laser always shines on solid bulk metal. This means that the melting threshold will be significantly reduced for the green laser compared to the an IR-laser. If IR-laser is powerful enough to induce melting the coupling will increase by a large factor. To verify this, a process map for copper was developed based on CFD simulations.

In the simulations, the scanning speed was varied from 100 $\mathrm{mm\,s^{-1}}$ to 800 $\mathrm{mm\,s^{-1}}$ both for an IR and a green laser source in the power ranges 400 W to 2500 W and 100 W to 600 W respectively. The laser source was modeled as a Gaussian laser with radius 50 µm. The reflectivity was calculated from the dielectric constant according to equation 3.20. For the IR

Table 7.1 – Model parameters for the reflectivity model. The temperatures are given in Kelvin.

Property	Value/Expression	Unit
σ_0	0.7	
Z^*	0.6	
$\rho_S(T)$	$6.229 \times 10^{-10} + 5.158 \times 10^{-11} T + 1.663 \times 10^{-14} T^2$	$\Omega\,\mathrm{m}$
$\rho_L(T)$	$1.103 \times 10^{-7} + 7.831 \times 10^{-11} T$	$\Omega\,\mathrm{m}$
ρ_0	1×10^{-8}	$\Omega\,\mathrm{m}$

laser the dielectric function was calculated according to Comins' model [20]. The relaxation time was derived from the electrical conductivity, which is given by a polynomial fitted to the data of Matula [97]. The model parameters, which are shown in table 7.1, were chosen to have a good agreement with the room temperature reflectivity from Babar [3]. The green laser reflections were calculated from a temperature and phase independent dielectric constant of $-4.88 + i4.69$ [3]. This corresponds to a perpendicular liquid absorptivity of approximately 10 % and 40 % for the IR and green laser respectively.

The simulation domain was a box of sides 1000 µm × 1000 µm × 500 µm. The domain was discretized using a non-uniform mesh, as shown in figure 7.2, with a minimal voxel size of 10 µm. The laser track was 400 µm long, with the run-time adjusted to match the track length for each speed.

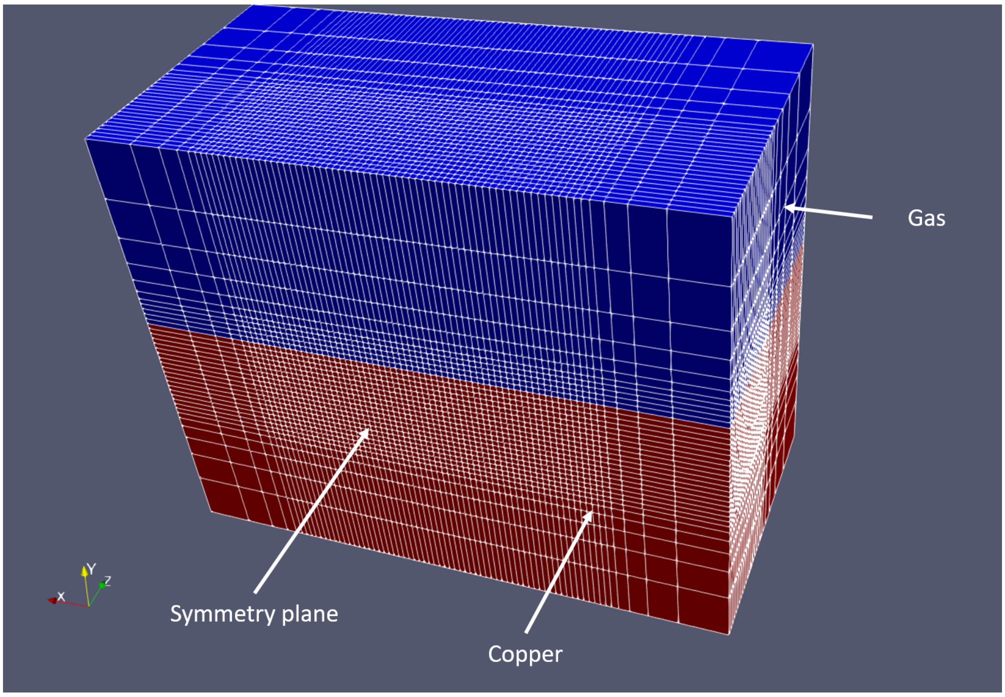

Figure 7.2 – Computational domain used for CFD simulations of laser welding. The total domain size is 1000 µm × 1000 µm × 500 µm, and the finest voxels have a side of 10 µm

Three different melting modes were distinguished: no melting, conduction mode, transition mode, and keyhole mode. The conduction mode is achieved when the weld surface does not show any recoil pressure depression on the top surface, the keyhole mode is reached when the depression is deeper than the radius, and the transition mode in-between. The melting modes are illustrated in figure 7.3.

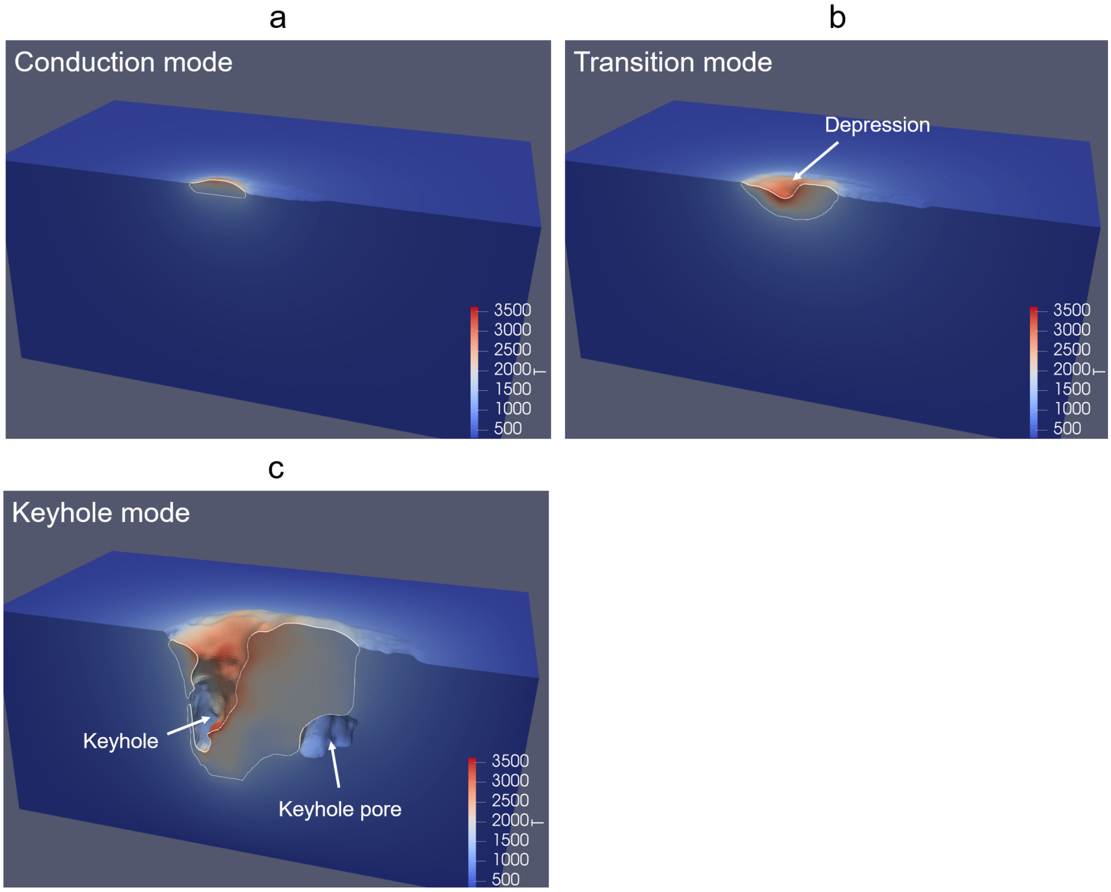

Figure 7.3 – CFD simulations showing the different melting modes in welding of a polished copper plate illuminated by an IR laser at different power. The color is indicating the temperature of the metal, and the white line is marking the liquid phase boundary. (a) Conduction mode, (b) transition mode, and (c) keyhole mode.

The calculated processing map is shown in figure 7.4 and includes both the actual power as well as the power normalized by the liquid absorptivity. The normalized values allows easy comparison between the two laser sources, and show clearly in which regimes the green laser outperforms the IR laser more than expected from the difference in liquid properties alone.

The melting threshold was found at approximately 1800 W for the IR laser, and 60 W for the green laser. The transition mode occurs at 2000 W for IR and 500 W for the green laser, at low scanning speed. The dimensions of the melt pool are insensitive to the scanning speed, which is expected as the Péclet number is lower than 1 in all cases considered. Above the normalized power where the IR-laser induces a melt (175 W) the melt pool dimensions are almost identical for both laser sources. The width of the green laser weld is increasing linearly over the entire simulation range, whereas the IR laser exhibits a discrete jump from 0 µm to 50 µm. This is clearly seen by plotting the melt pool widths at 100 mm s^{-1} against the power, see figure 7.5. This is can be explained by the discrete change in the optical properties of the IR-spectrum at the phase transition.

A consequence of this is that there is a minimum size of the melt pool which can be formed by the IR-laser, as the liquid properties determine the melt pool dimensions, but only above the power where melting is initiated. Consequently the use of a green laser is beneficial in situations where a fine conduction mode weld is desired. If a melt would be, by some arbitrary mechanism, initiated and continued by the IR-laser, it would still be possible to form smaller welds. For the formation of larger welds, there is still the inherent benefit of the higher liquid absorptivity, but nothing exceeding this.

It is worth noting that the power required to form a melt with the IR-laser is high, and seem to be overestimated in the simulation. A reasonable explanation is that the reflectivity predicted in the liquid by Commin's model might be too high, but it is not known whether this is due to inherent flaws of the model, or whether the absorptivity is increased under the laser intensities of LPBF. However, the incorrect absolute values of the reflectivity are considered uncritical for these simulations since the focus of this work was to study the large step in the absorptivity at melting, which is accounted for by the model, as well as the difference in the normalized absorptivity at different wavelengths. Nevertheless, the uncertainty highlights the difficulty in choosing the correct parameters for simulations and other models. As a consequence the reflectivity will be set as a fixed constant for for the simulations presented below.

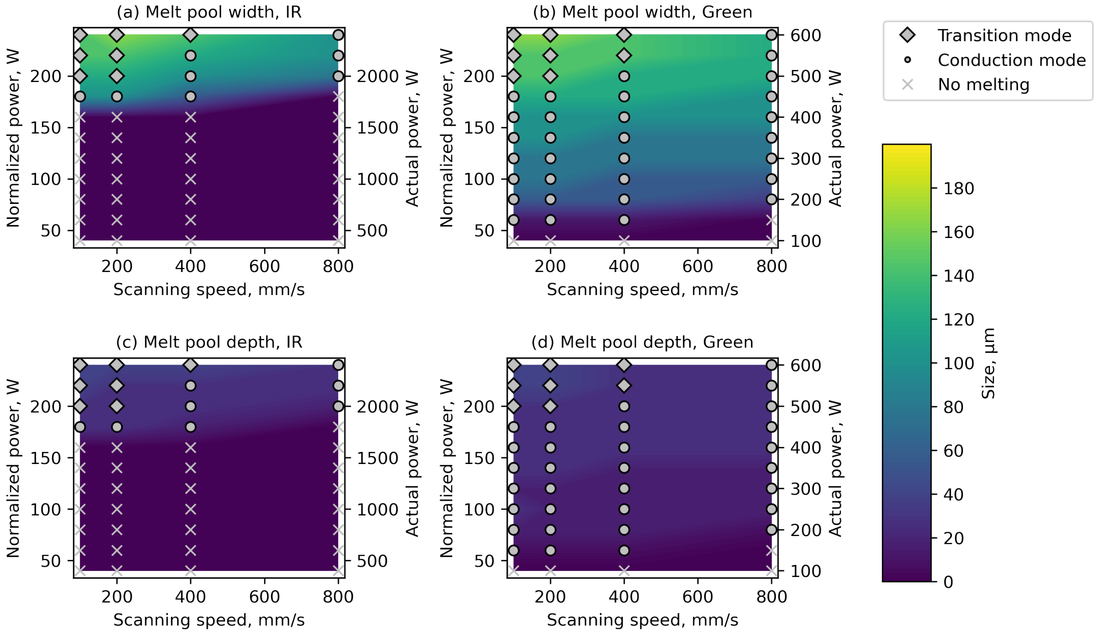

Figure 7.4 – Simulated melt pool dimensions and melting mode for laser welding of pure copper using an IR and green laser. The power is shown normalized by the liquid absorptivity on the left side, and non-normalized on the right side. (a) Width of melt pool with IR laser, (b) width of melt pool with green laser, (c) depth of melt pool with IR laser, and (d) depth of melt pool with green laser.

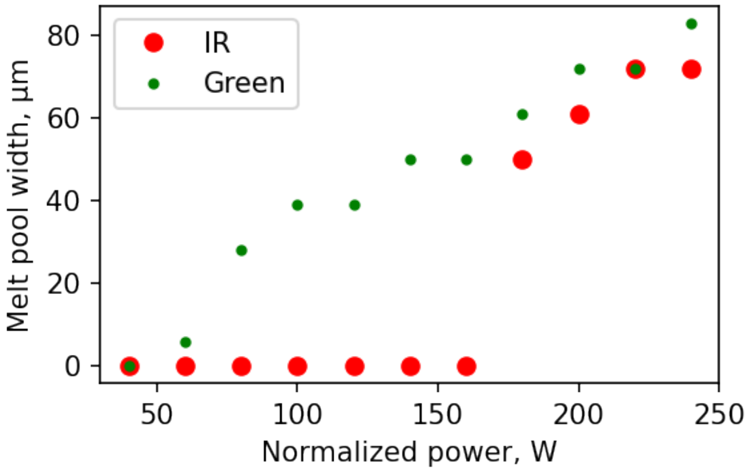

Figure 7.5 – The simulated melt pool widths for laser welding of copper at 100 mm s^{-1} with a green and IR laser source. The gap in properties as the melt threshold is reached is seen clearly.

7.1.2 Combined IR and green laser welding of copper

In the previous section it was shown that the melt pool dimensions are determined by the properties of the liquid phase, as long as the power is high enough to induce melting of the solid phase. It was further shown that, if the solid has a higher reflectivity than the liquid and if a melt is already present it is possible to sustain the melt below the melting threshold of the solid. In this section the possibility of forming a melt pool in copper at low laser power is investigated by combining an IR-laser with a Q-switched green laser. The IR-laser has a pulse length tunable in the ms-range and a tunable power in the range 5 W to 275 W, whereas the green laser has a pulse length of around 50 ns and a tunable pulse energy in the range 0 mJ to 3 mJ, equivalent to a peak power of around 150 kW. The two lasers are focused at the same spot, and synchronized at 10 Hz as shown schematically and explained in section 4.1.2.

The melt spots from the green laser are shown in figure 7.6 for different pulse energies, together with high speed camera images of the interaction area. As expected, the spots become larger with increasing energy, with clear ablation starting to occur from 0.9 mJ which is also when the final shape of the spot is reached.

If only the IR-laser is used, no melt formation is observed, as was expected. Melting in combination with the green laser was initiated for some of the pulses when the pulse energy of the green laser was 0.3 mJ. The fraction of pulses for which a melt was initiated by the IR-laser increased up to a pulse energy of 0.7 mJ for the green laser, at which a plateau was reached, see figure 7.7 a). A threshold is observed when varying the length of the IR-laser pulses No melt is observed at pulses of length 10 ms and shorter, see figure 7.7 b). The melts are shallow, as can be expected at the low power, and forms a cap. The SEM images in 7.7 c) shows that the microstructure is a columnar at the edges, and equiaxed at the center.

The formation of the melt with the IR-laser does not correlate with the formation of a melt from the green laser. This indicates that the melt is not initiated by the increased absorptivity of the liquid metal. To validate this hypothesis, a further experiment was performed in which the IR-pulses were overlapping. In a first trial, the green laser was synchronized with the IR-laser. In the second trial two passes were done, with the green laser on the first, and the IR-laser on the second and with a delay of around one minute between the passes. In both cases melting was initiated, verifying that the melting with the IR-laser was not initiated by the liquid formed with the green laser.

The origin of the melt initiation could not be conclusively determined, but a few possible origins can be postulated. One possibility might be oxidation of the surface, but as can be seen in figure 7.6 the green laser does not induce strong oxidation. Another possibility is multiple reflection from the edge of the melt spot from the green laser. The 10 ms delay in the formation of the IR-melt pool would in this case be explained by the time needed for the center of the IR-beam to traverse to the edge of the green laser melt. This hypotheis must however be considered unlikely since there is no melt forming at the center of the green spot, where there is significant ablation which presumably would provide a larger increase of the

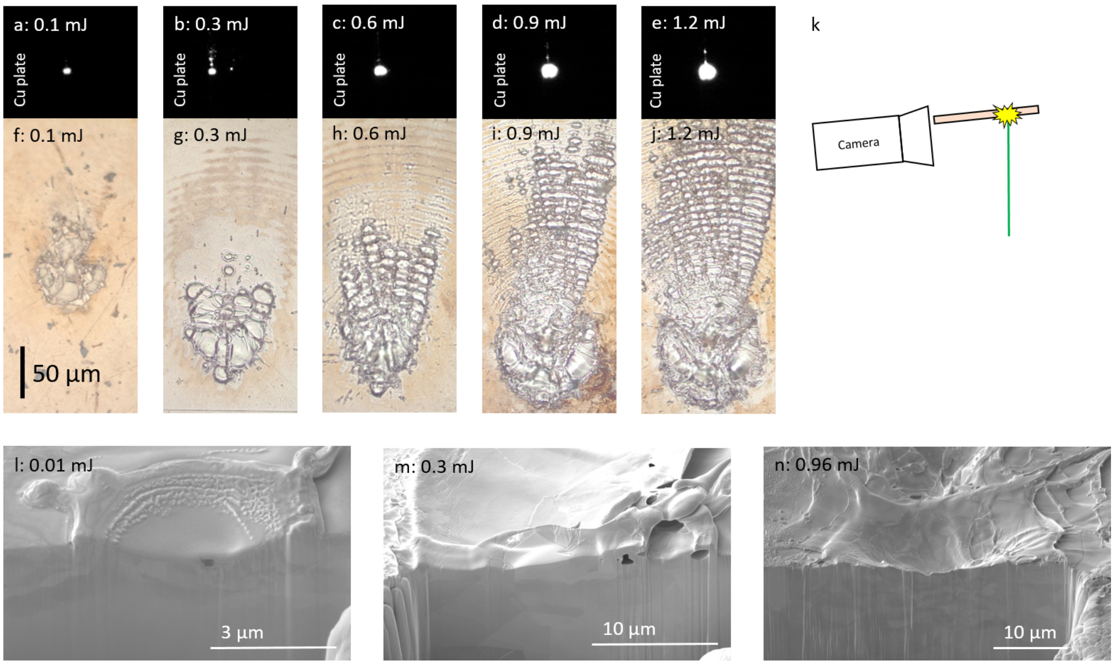

Figure 7.6 – Melt pools from the pulsed green Q-switched laser at different pulse energies. Frame (a-e) show high speed imaging captured during processing according to the sketch in frame (k). Frame (f-j) show top-view optical images of the melt pools. In frame (l-n) SEM images of the melt pool centers, cross-sectioned by FIB, are shown.

absorptivity than the edge. A third possibility is the redeposition of ablated material on the surface, increasing the absorbtivity by increased roughness or plasmonic resonance. This is supported by the observation of a delay in the melt formation, as the ablated material needs time to redeposit. However no deposited particles could be found by inspection of the surface with SEM.

Even though the mechanisms could not be completely determined from these experiments, it was verified that it is indeed possible to sustain melt with an IR laser below the IR-melting threshold. This can be useful for stabilizing the weld close to the melting threshold, where fluctuations in the coupling could possibly cause the weld to slowly fade. Possible methods for this include the method proposed above, but could also include the roughening of the solid surface, or the addition of absorbing films or nano-particles. These surface additions would not have to survive the melting, as the benefit comes from the initialization phase of the melt.

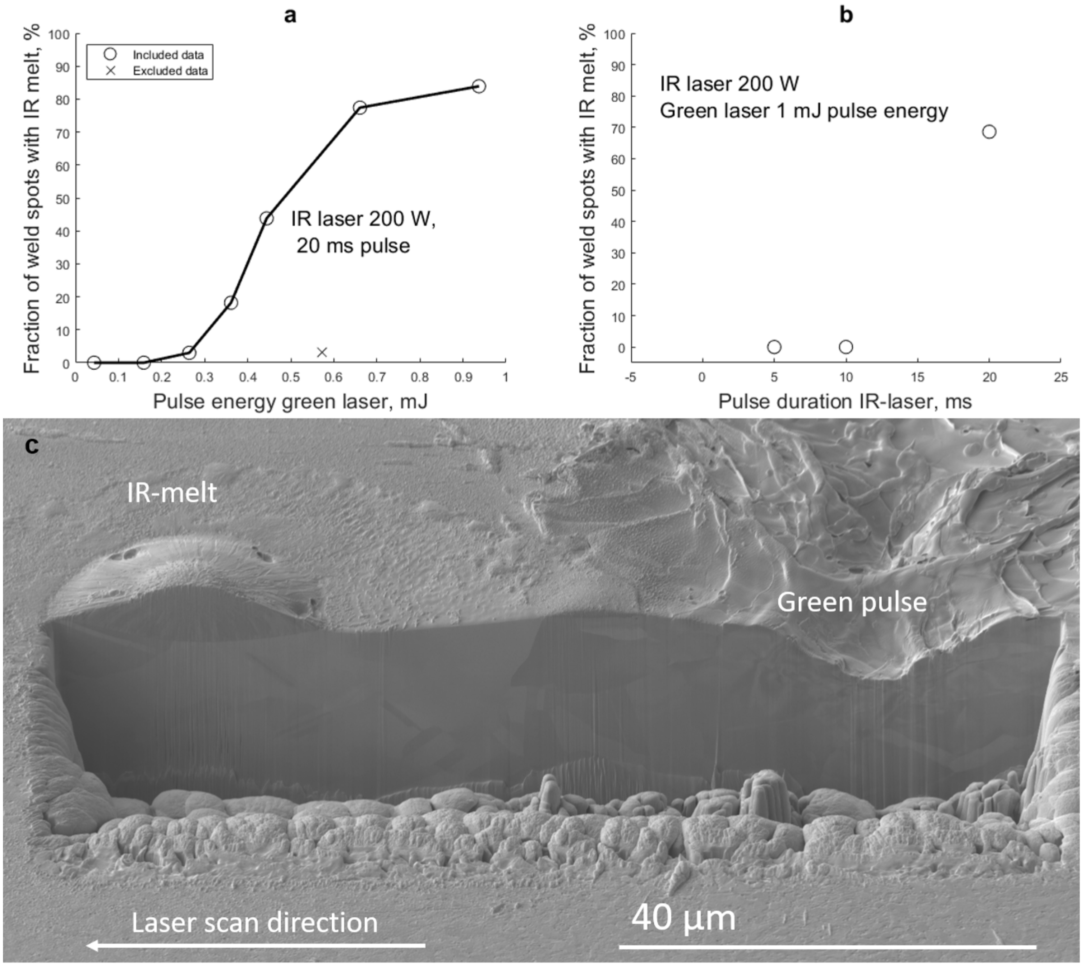

Figure 7.7 – Threshold for melt initiation in dual laser welding of copper. a) The melt fraction against the pulse energy of the green laser at the substrate. b) The melt fraction against the pulse duration of the IR laser. c) FIB Cross-section of green and IR-weld spots.

7.2 LPBF with green laser

The power required to melt powder is significantly lower than to induce melting on a flat plate, as shown in chapter 5 by the the copper samples, which melt without issue at 125 W. The reason is two-fold: the thermal isolation of the powder particles allow heat to accumulate in the powders until melting and wetting of the substrate increase the contact, and the increased absorptivity of the powder bed due to multiple reflections. On the other hand the experiments with coated powders showed that absorption in the solid phase is most likely important for the overall heat balance.

In the section below the optical interaction of the laser with the powder bed is investigated through CFD-simulations and experiments. The simulations aim at showing how the laser light is reflected from the melt pool, and to which degree these reflections contribute to the melt pool heat balance. The experiments are intended to verify the simulations and to serve as a proof-of-concept for using a green laser as a LPBF laser source.

7.2.1 Simulation of LPBF of copper with green and IR laser

LPBF of a single layer of copper was simulated with the CFD model described earlier to investigate the distribution of the laser light. To simplify the simulations the reflection model given by equation 3.19 was chosen. This model captures the most important aspect of the IR absorption: the presence of a discrete jump in the optical absorptivity at the melting point. The values of the reflectivity are selected as:

$$R_{\mathrm{IR}} = \begin{cases} 0.90 & \text{solid} \\ 0.75 & \text{liquid} \end{cases} \tag{7.1}$$

$$R_{\mathrm{green}} = \begin{cases} 0.60 & \text{solid} \\ 0.60 & \text{liquid} \end{cases} \tag{7.2}$$

The powder bed was simulated as an ordered, tightly packed bed with a lattice parameter of 50 µm, but like for the simulations presented in chapter 5, the powder particle diameter was decreased to 45 µm to ensure thermal isolation from each other and from the substrate. A simulation domain of the dimensions 800 µm × 275 µm × 300 µm was chosen with uniform mesh voxels of the dimension 2.5 µm × 2.5 µm × 2.5 µm. The laser scan velocity was set to 300 $\mathrm{mm\,s^{-1}}$, which is typical for LPBF processing. The laser spot size was chosen to be 50 µm in diameter.

The simulation results are shown in figure 7.8, and are arranged so that the adjacent green and IR simulations have the same power, normalized by the liquid absorptivity. The total reflectivity of the whole domain as a function of time is also shown in the figure. The simulations show the expected transition from incomplete melting, to balling, to conduction/transition mode as

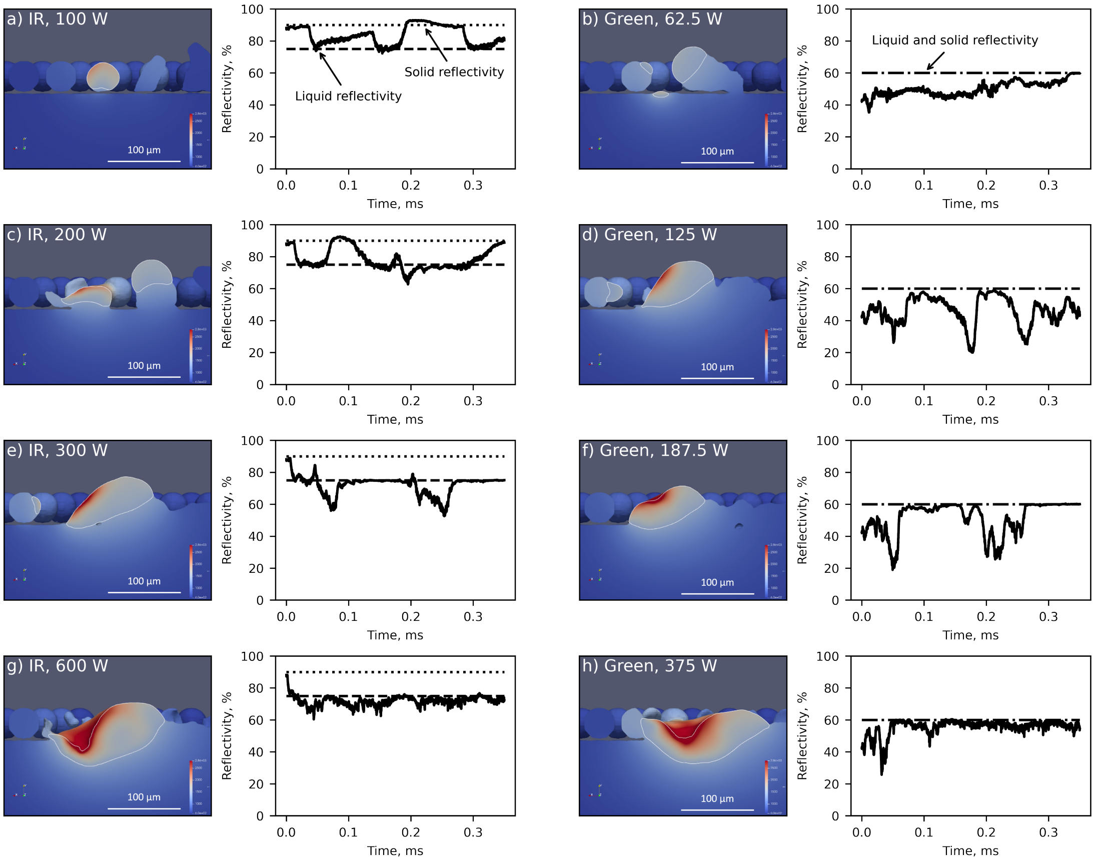

Figure 7.8 – Cross-sections along the centerline of simulated LPBF melt tracks of pure copper with IR (left column) and with green laser (right column) is shown together wit the time-dependence of the total reflectivity including the effect of multiple reflections. The power normalized by liquid absorptivity is the same in the welds made with the IR and green laser: a & b 25 W, c & d 50 W, e & f 75 W, and g & h 150 W.

the power is increased. The transitions for the green laser, however, occur at lower power, but once conduction mode is reached the shape of the melt pools converge. This can be explained by the reflections of the incoming laser light: In incomplete melting mode, light gets trapped in-between the powder particles, leading to increased coupling. In balling mode the melt pool is slushing backwards and forwards leading to a periodic variation of the absorptivity as the reflected light hits the powder in front of the melt. The increased coupling is much more pronounced with the green laser, as the solid absorptivity is higher. This leads to a preheating, which is large enough to partially melt the powder. In conduction mode melting, slushing of the melt pool is still observed, but not enough to reflect the light onto the powder ahead of the melt, making the reflectivity pattern more stable over time and leading to the convergence of the melt pool geometry.

This trend of the reflectivities is well illustrated by plotting the time-averaged total absorptivity of the melt and powder bed versus the normalized power, as shown in figure 7.9. At low power a high absorptivity of the powder bed is seen for the green laser, and a low absorptivity for the IR laser, whereas at high power the absorptivities converge. It is therefore assumed that the benefit of using a green laser is larger when processing with lower laser power. At a first glance this would speak against the green laser, as it is desired to operate in conduction mode where the benefit of the green laser stems from the increased liquid absorptivity only. However there will always be unexpected fluctuations decreasing the light coupling during processing, for example due a locally increased powder density or spatter temporarily blocking the beam. Under green laser light these fluctuations will be dampened out as they lead to higher absorptivity. The IR laser will, if close to the balling threshold, however amplify the disturbance as the absorptivity decreases. Thus, the green laser can be expected to lead to more robust results, allowing processing at lower power or higher speed.

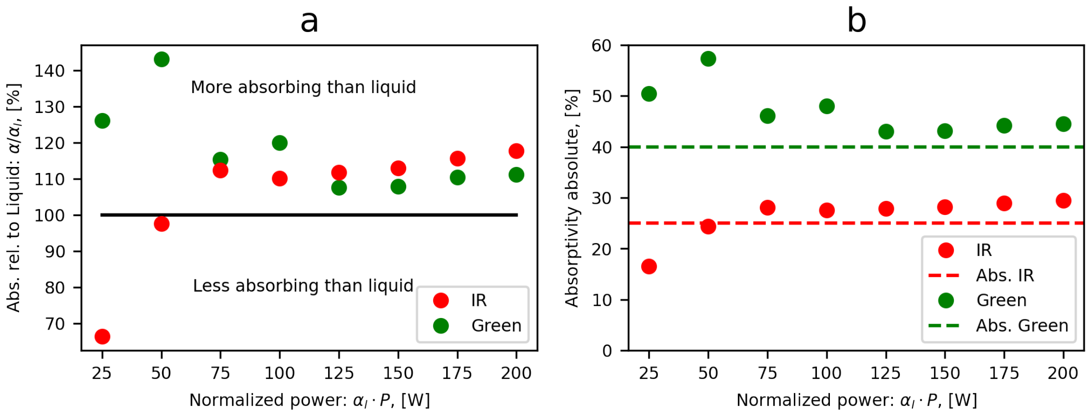

Figure 7.9 – (a) The absorptivity relative to the absorptivity of the liquid plotted against the laser power normalized by the liquid absorptivity for a single LPBF track on copper. (b) The absorptivity in absolute values against the laser power normalized by the liquid absorptivity for a single LPBF track on copper.

7.2.2 Back reflection measurement of single LPBF tracks

To verify the simulations results presented in section 7.2.1, single line scans were carried out with the IR-laser system described in section 4.1.4. Since the setup does not have a laser source powerful enough to cover the whole range of melting modes for copper, bronze was chosen as a model material. The parameters were scaled to achieve balling number and Péclet number corresponding to those in the simulations: Power in the range 50 W to 250 W and the scanning speed set to 100 mm s^{-1}. The substrate, with dimensions 25 mm × 25 mm × 3 mm, was made from the bronze powder with LPBF. This block was machined flat and grooves 50 µm deep were added on one surface. Before processing the powder was filled in the grooves and manually flattened with a metallic coater. The back reflections were measured through the focusing lens, and the tracks were imaged using SEM.

The experimental reflection spectra shown in figure 7.10 are qualitatively very similar to the simulated reflection spectra in section 7.2.1, with a stable reflection around the keyhole threshold, periodically oscillating around the balling threshold, and with massive reflection peaks when severe balling occurs. Some differences can be seen: for example, the reflection peaks are bell shaped in the experiment, but the simulations show step-like patterns. This is presumably due to the directionality of the sensor, which only account for the light which is reflected straight back. Similar effects could be seen for other parts of the other spectra, which seem to correlate with gaps in the melt track. Since the patterns shown in the back-reflection spectra are very clear and can be easily correlated with the physical processes, measuring the back reflected light is a good candidate for in-situ measurements of the melting mode. Such measurements could be used for defect measurement or fast validation of processing parameters.

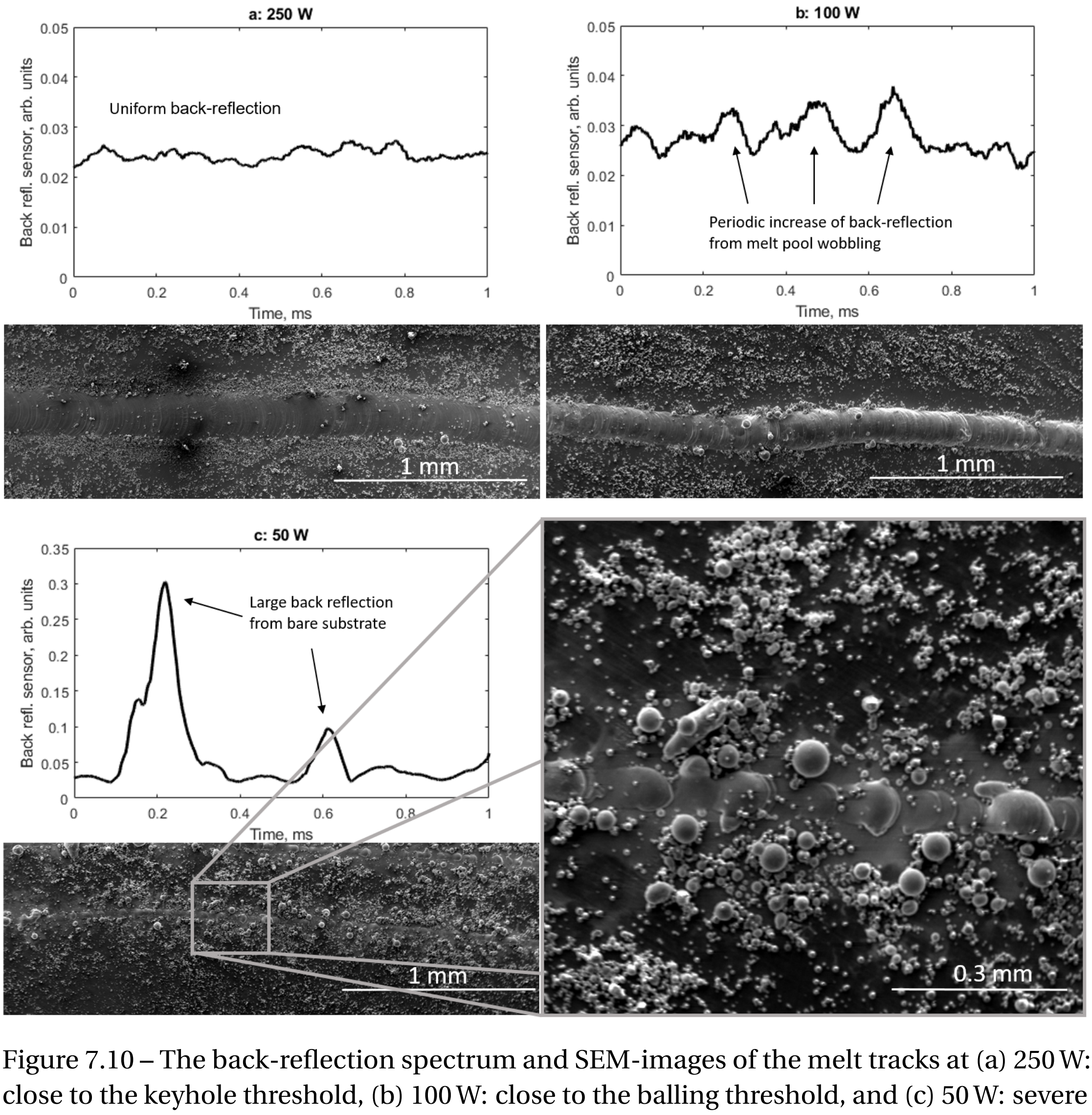

Figure 7.10 – The back-reflection spectrum and SEM-images of the melt tracks at (a) 250 W: close to the keyhole threshold, (b) 100 W: close to the balling threshold, and (c) 50 W: severe balling. Note that the scale for the back reflections is significantly enlarged in (c).

7.2.3 Single LPBF tracks of copper with green laser

As a proof-of-concept and to simulate LPBF of copper with a green laser source, single line scans of copper were performed using the green laser setup described in section 4.1.3. The power output of the laser system is 66 W, measured at the target. This power is, due to the small spot size of around 15 µm enough to cause melting of a flat surface, the melt pools will however not be large enough to avoid balling using regular 45 µm power. Assuming, in accordance with the simulations above, an absorptivity increase of 20 % to 40 % relative to a flat plate the expected maximum diameter for avoiding balling according to equation 5.16 is 6.4 µm to 7.5 µm. Thus to process the powder without balling, a fine powder sieved to a diameter of -5 µm was used.

The powder was placed in flat copper plates with 5 and 10 µm deep grooves on the surface. The precision of the groove depth was measured by confocal microscopy to be within 2 µm of the target depth. The scanning speed was set to the highest possible for the stage, $8\,\mathrm{mm\,s^{-1}}$, which is low for LPBF conditions. However the low scan speed was considered to be of minor importance since the balling defect formation is only weakly dependent on the scanning speed.

Due to the poor flowability of the powder, it was not possible to form 5 µm thick layers in the grooves. In the 5 µm grooves a minimum powder thickness of 10 µm was achieved, and for the 10 µm grooves, the thickness was around 20 µm. In the deeper grooves, the melting is clearly in balling mode, but in the thinner grooves, conduction mode welds form in regions where the powder was thinner. This is illustrated in figure 7.11 where confocal microscope mappings are shown before removing the loose powder.

The conduction mode caps are around 25 µm wide and are periodically interrupted. The track is surrounded by loosely bound balling-like features on the sides of the melt track. The gaps in the weld tracks correlate with the presence of these features indicating that these denudate the surface. Similar features was seen when processing without powder, indicating that the origin of these features is from the beam shape rather than reflections from the melt pool.

7.3 Conclusions

It could be shown for both laser welding and LPBF that strategies in which the absorptivity of the solid is increased is beneficial for processing of copper at lower laser power. However, the mechanisms are fundamentally different: In the case of laser welding the increase in absorptivity comes from a reduced melting threshold, allowing the laser to illuminate absorbing liquid. In the case of LPBF the effect comes from forward scattering of the laser beam which pre-heats the powder in front of the melt. The reason for this difference is the use of powder in the LPBF process, which unlike the flat surface melt at all relevant power levels, and since it is sticking out of the substrate, allowing the forward scattering of light. The benefit of increasing the solid absorptivity in both cases becomes less pronounced at high power laser processing.

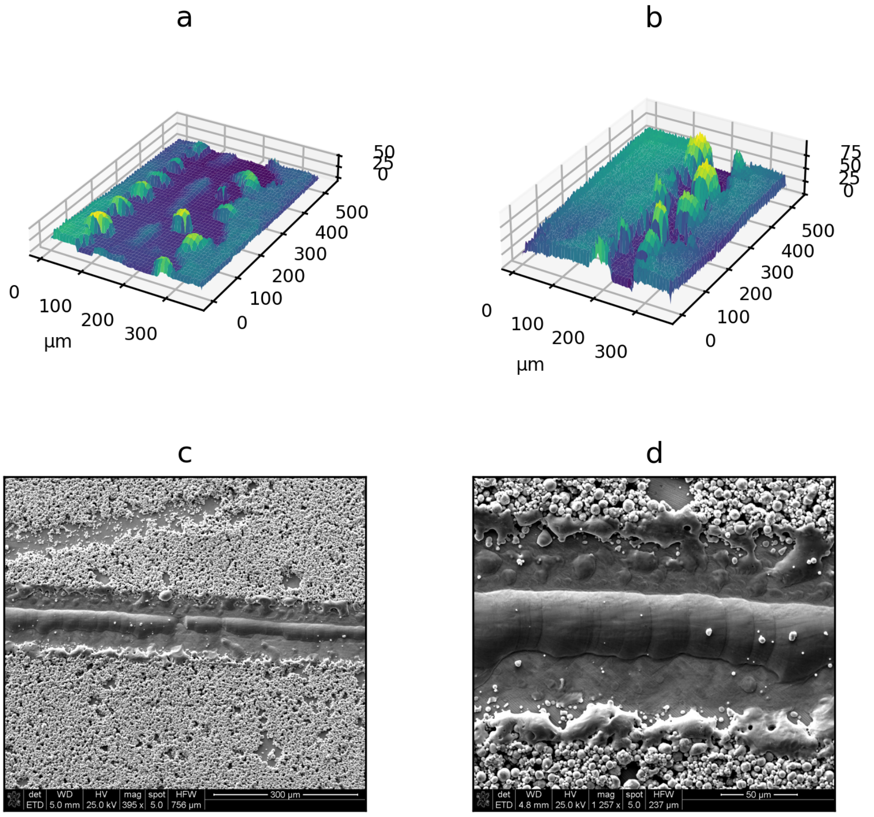

Figure 7.11 – Confocal microscope height map of LPBF line scans of copper with green laser. (a) 5 µm powder in 5 µm groove and a powder layer height of 10 µm in conduction mode. (b) 5 µm powder in 10 µm groove and a powder layer height of 20 µm in balling mode. (c) &(d) SEM images of the melt track seen from above.

In welding when the power is sufficiently high to initialize a melt on its own, and in LPBF when transition mode melting is reached.

8 Conclusion and outlook

A key question of this thesis was the origin of the balling type porosities typically seen in LPBF of copper. At low scanning speeds, this is well explained by the increased heat flow through the cap-substrate interface as the molten powder wets the substrate. The increased heat-flow eventually leads to a situation where the temperature of the cap edge reaches the solidification temperature, which effectively pins the spreading of liquid. This wetting width, which is the same as the melt pool width, together with the powder size and packing density thus determines the shape of the cap. It could be shown that in the case of a tightly packed powder bed of a uniform powder size distribution the width necessary to avoid balling pores is 2.6 times the powder diameter, a value which agrees well with the experimental results presented in chapter 5.

The power required to reach that wetting width defines the balling threshold, and using simple analytical models it can be shown that the power needed to reach this width is proportional to the powder radius, thermal conductivity and melting temperature and inversely proportional to the optical absorptivity:

$$P_{\text{balling}} \propto \frac{r_p K \Delta T_M}{\alpha} \tag{8.1}$$

The proportionality factor is in the case of a tightly packed single layer mentioned above approximately 25.5. This power can be used as a normalization factor for the power to get the balling number, Ba: a dimensionless number which shows how close to the balling threshold one is operating for any material given the processing power.

The balling number can be used as a predictor for the relative density of a part. Two clear regimes are seen, $Ba < 1$ where the density rapidly decreases linearly, and $Ba > 1$ where the density slowly increase. The discrete change in behavior which is seen as the balling threshold is surpassed, shows that it is reasonable to classify the low power defects into balling and lack-of-fusion defects rather than lumping them together under the same term. The physical difference between these two defects is that the former occurs in balling mode, where the heat is diffused through the cap leading to an approximately uniform substrate heat source term, and the latter in conduction mode, where the heat flow is approximated by the laser intensity distribution.

Processing at higher scanning speeds, where the Péclet number is above 1, makes the situation mathematically more complex. This case was not studied in this thesis but like for normalized enthalpy, the power will most likely need to be scaled by the Péclet number. At elevated scanning speeds, the assumption that the powder coagulation is fast with regard to the laser interaction time does also not necessarily hold anymore. For copper in balling mode, where the coagulation is the slowest, this point was predicted to occur at around $400\,\mathrm{mm\,s^{-1}}$, which corresponds to a drastic drop in the density of experimental samples. This mechanism was also not studied in detail, but is highly important for industrial applications where high processing speed is important from economical point-of-view.

The melt pool is highly dynamic, with the cap constantly sloshing and deforming due to the momentum added by the coagulating powder particles. The shape of the melt pool is strongly dependent on the melting mode, leading to different characteristic absorption profiles. In balling mode reflection from the melt is of high importance, leading to coupling and pre-heating of the powder ahead of the melt pool and on the substrate. This also occurs in conduction mode at low power, but as the power increases, the effect becomes less and less pronounced and becomes irrelevant at the transition to keyhole mode. The mechanism of forward scattering of the light is important for pore mitigation strategies as it means that the coupling around the balling threshold can be increased by increasing the optical absorptivity of the solid. The different reflection profiles can also be used as a fingerprint for the melting mode to in-situ evaluate the process parameters. More work is required to understand the influence of the processing parameters, and material properties on the pattern.

To fully make use of the information contained in the reflection pattern, the development of more accurate optical models is required. Such models would have to accurately account for temperature effects, alloying effects, polarization, formation of vapor and plasma close to the surface, etcetera. The development and implementation of more accurate optical models is also important for predictive modelling, allowing the models to be based on real physical properties rather than effective absorptivities which need to be calibrated to experiment. Closely related is the availability of high quality optical data at the full temperature range from room temperature to boiling, which currently is usually not available, except for a few pure elements.

The increase of the absorptivity of the solid was realized experimentally in two separate ways for LPBF: through the coating of the copper powder with a thin layer of more absorbing metal and through processing with a green laser source instead of a conventional near-IR laser source. The coatings, which are made using an immersion deposition method, are simple, cheap, and scalable, and can be tuned with respect to the choice of coating metal, morphology and thickness by varying the chemical composition of the bath. It could be shown that the amount of balling defects were significantly reduced for tin coated copper powders compared to in-situ alloyed powder mixtures of similar composition. This approach is suitable for copper alloys with a low alloying element content as it combines the alloying with a reduction of the balling threshold. The method is also expected to work well for gold and silver alloys, which are similar to copper both in their chemical and physical properties. It is a priori difficult to predict not only how much the absorptivity will increase because of the coatings and to which degree the increased absorption will contribute to decrease the porosity. These effects are not easy to capture with simple models as many different physical processes are interacting: dynamics of the fluid, change of physical propertie s due to spatially and temporarily varying concentrations, multiple reflections of the laser. High fidelity CFD-simulations could play a big role, but is as mentioned above dependent on development of reflection models. A good complement to the experiments performed in this thesis would also be the direct measurement of the total absorptivity of the system, preferably in combination with high speed imaging.

The use of a green laser increases the absorptivity of both the liquid and the solid. This is in many regards analogous to using metallic coatings, but without the need to introduce alloying elements. The use of a green laser in combination with a fine (< 5 µm) powder distribution allowed to avoid the occurence of balling mode in pure copper at a laser power as low as 66 W. The use of fine powder further allows to manufacture very fine structures. In this work the fabrication of 25 µm wide tracks was shown to be feasible, but according to the balling criterion discussed above, this value should be possible to decrease this value to around 15 µm using the same powder. However, The use of the fine powder makes coating of the substrate difficult, and more development work is needed for use in LPBF of whole parts.

A Detailed derivations

A.1 Derivation of equation 5.5 on dimensionless form

Starting from equation 5.5:

$$T(r,z) = T_0 + \frac{\alpha P}{2\pi r_w K}\int_0^\infty d\lambda \exp(-\lambda|z|)\frac{J_0(\lambda r)J_1(\lambda r_w)}{\lambda} \tag{A.1}$$

where the following identities hold:

$$I = \int_0^\infty d\lambda \frac{J_0(\lambda)J_1(\lambda)}{\lambda} \tag{A.2}$$

$$r_w = I\frac{\alpha P}{2\pi \Delta T_M K} \tag{A.3}$$

$$P_{\text{Balling}} = \frac{2\pi}{I}\frac{r_p K \Delta T_M}{\alpha} \tag{A.4}$$

$$Ba = \frac{P}{P_{\text{Balling}}} = \frac{r_w}{2.6 r_p} \tag{A.5}$$

To normalize we make the substitution to normalized temperature and coordinates:

$$\Theta = (T - T_0)/(T_M - T_0) \tag{A.6}$$

$$\mathfrak{R} = r/r_p \tag{A.7}$$

$$\mathfrak{Z} = z/r_p \tag{A.8}$$

$$\lambda' = \lambda r_P \tag{A.9}$$

Leading to the following equation

$$\Theta(\mathfrak{R},\mathfrak{Z}) = I^{-1}\int_0^\infty \frac{\exp\left(-\lambda'|\mathfrak{Z}|\right)J_0\left(\lambda'\mathfrak{R}\right)J_1\left(2.6Ba\lambda'\right)}{\lambda'}d\lambda' \tag{A.10}$$

A.2 Width to depth ratio in balling mode

Starting from the same point as in the last section but normalizing by wetting width:

$$\begin{aligned} \Theta &= (T - T_0)/(T_M - T_0) && \text{(A.11)} \\ \mathfrak{R}' &= r/r_w && \text{(A.12)} \\ \mathfrak{Z}' &= z/r_w && \text{(A.13)} \\ \lambda'' &= \lambda r_w && \text{(A.14)} \end{aligned}$$

we arrive at:

$$\Theta(\mathfrak{R}, \mathfrak{Z}) = I^{-1} \int_0^{\infty} \frac{\exp\left(-\lambda'' |\mathfrak{Z}|\right) J_0\left(\lambda' \mathfrak{R}\right) J_1\left(\lambda''\right)}{\lambda''} d\lambda'' \tag{A.15}$$

The depth of the melt is given by $\Theta(0, \mathfrak{Z}) = 1$:

$$1 = I^{-1} \int_0^{\infty} \frac{\exp\left(-\lambda'' |\mathfrak{Z}|\right) J_1\left(\lambda''\right)}{\lambda''} d\lambda'' = I^{-1} \left(\sqrt{\mathfrak{Z}'^2 + 1} - |\mathfrak{Z}'|\right) \tag{A.16}$$

This equation can be numerically solved to yield $\mathfrak{Z}' = 0.461\ldots$. The normalization makes it so that $D/W = \mathfrak{Z}'/2 \approx 0.231$. It is also interesting to note that the peak temperature is given by

$$\Theta(0,0) = I^{-1} \int_0^{\infty} \frac{J_1\left(\lambda''\right)}{\lambda''} d\lambda'' = I^{-1} \tag{A.17}$$

Measuring the melt pools diameters of the 316L samples from chapter 5.2.2 after chemical etching validates the theoretical value of the depth-to-width ratio. The measured ratio is shown in figure A.1, against the cap height for the sample produced at $Ba = 0.83$ and $Ba = 1.24$. For the lower power sample the ratio is reached at a cap height somewhere between 25 µm to 45 µm, above which it remains constant. At the higher power sample the ratio gets close to the theoretical balling mode value, but it is never reached, not even at a cap height larger than 70 µm. These masurements show that the balling mode heat-transfer proposed in chapter 5 is a good approximation below the balling threshold.

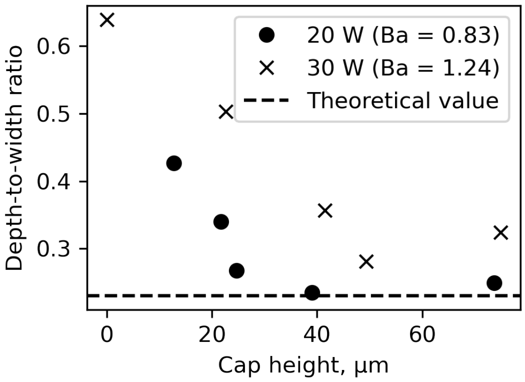

Figure A.1 – Depth-to-width ratio of melt pools in etched 316L samples above ($Ba = 1.24$) and below ($Ba = 0.83$) the balling threshold.

Bibliography

[1] Mohamadreza Afrasiabi, Christof Lüthi, Markus Bambach, and Konrad Wegener. Multi-resolution SPH simulation of a laser powder bed fusion additive manufacturing process. *Applied Sciences (Switzerland)*, 11(7), 2021.

[2] David Appleyard. Powering up on powder technology. *Metal Powder Report*, 70(6):285–289, 2015.

[3] Shaista Babar and J. H. Weaver. Optical constants of Cu, Ag, and Au revisited. *Applied Optics*, 54(3):477, 2015.

[4] Priyanshu Bajaj, Jonathan Wright, Iain Todd, and Eric A. Jägle. Predictive process parameter selection for Selective Laser Melting Manufacturing: Applications to high thermal conductivity alloys. *Additive Manufacturing*, 27:246–258, 2019.

[5] Dieter Bäurle. *Laser Processing and Chemistry*. Springer, Berlin Heidelberg, 4 edition, 2011.

[6] C. D. Boley, S. C. Mitchell, A. M. Rubenchik, and S. S. Q. Wu. Metal powder absorptivity: modeling and experiment. *Applied Optics*, 55(23):6496, 2016.

[7] J. U. Brackbill, D. B. Kothe, and C. Zemach. A continuum method for modeling surface tension. *Journal of Computational Physics*, 100(2):335–354, 1992.

[8] D. Braess. *Finite Elements: Theory, Fast Solvers, and Applications in Solid Mechanics*. Cambridge University Press, Cambridge, 3rd edition, 2007.

[9] J. Brent Hiskey and V. P. Atluri. Dissolution Chemistry of Gold and Silver in Different Lixiviants. *Mineral Processing and Extractive Metallurgy Review*, 4(1-2):95–134, 1988.

[10] Damien Buchbinder, Wilhelm Meiners, Norbert Pirch, Konrad Wissenbach, and Johannes Schrage. Investigation on reducing distortion by preheating during manufacture of aluminum components using selective laser melting. *Journal of Laser Applications*, 26(1):012004, 2014.

[11] Claus Cagran. *Thermal conductivity and thermal diffusivity of liquid copper*. PhD thesis, TU Graz, 2000.

[12] H.S. Carslaw and J.C. Jaeger. *Conduction of heat in solids.* Oxford University Press, Oxford, 2nd edition, 1959.

[13] M. N. Chandrasekharaiah. Weldability and weld joint failures. *Sadhana*, 20(1):213–232, 1995.

[14] Da Chen and Xiaoyu Zheng. Multi-material Additive Manufacturing of Metamaterials with Giant, Tailorable Negative Poisson's Ratios. *Scientific Reports*, 8(1):1–8, 2018.

[15] Qiang Chen, Gildas Guillemot, Charles André Gandin, and Michel Bellet. Three-dimensional finite element thermomechanical modeling of additive manufacturing by selective laser melting for ceramic materials. *Additive Manufacturing*, 16:124–137, 2017.

[16] Jung Ho Cho, Dave F. Farson, John O. Milewski, and Kendall J. Hollis. Weld pool flows during initial stages of keyhole formation in laser welding. *Journal of Physics D: Applied Physics*, 42(17), 2009.

[17] J. A. Choren, S. M. Heinrich, and M. B. Silver-Thorn. Young's modulus and volume porosity relationships for additive manufacturing applications. *Journal of Materials Science*, 48(15):5103–5112, 2013.

[18] Michael Cloots, Peter J. Uggowitzer, and Konrad Wegener. Investigations on the microstructure and crack formation of IN738LC samples processed by selective laser melting using Gaussian and doughnut profiles. *Materials and Design*, 89:770–784, 2016.

[19] W. W. Coblentz. The reflecting power of various metals. *NBS Bulletin*, 7(2):197–193, 1911.

[20] N. R. Comins. The optical properties of liquid metals. *Philosophical Magazine*, 25(4):817–831, 1972.

[21] Frank Cooper. Sintering and additive manufacturing: "additive manufacturing and the new paradigm for the jewellery manufacturer". *Progress in Additive Manufacturing*, 1(1-2):29–43, 2016.

[22] Di Cui, Antaryami Mohanta, and Marc Leparoux. Interface control in additive manufacturing of dissimilar metals forming intermetallic compounds—Fe-Ti as a model system. *Materials*, 13(21):1–13, 2020.

[23] Anthony De Luca, Christoph Kenel, Seth Griffiths, Shreyas S. Joglekar, Christian Leinenbach, and David C. Dunand. Microstructure and defects in a Ni-Cr-Al-Ti γ/γ' model superalloy processed by laser powder bed fusion. *Materials and Design*, 201, 2021.

[24] T. DebRoy, H. L. Wei, J. S. Zuback, T. Mukherjee, J. W. Elmer, J. O. Milewski, A. M. Beese, A. Wilson-Heid, A. De, and W. Zhang. Additive manufacturing of metallic components – Process, structure and properties. *Progress in Materials Science*, 92:112–224, 2018.

[25] Carl Deckard. Method and Apparatus for Producing Parts by Selective Sintering. *US Patent No: 4,863,538*, 1986.

[26] Erik R. Denlinger, Jeff Irwin, and Pan Michaleris. Thermomechanical modeling of additive manufacturing large parts. *Journal of Manufacturing Science and Engineering, Transactions of the ASME*, 136(6):1–8, 2014.

[27] Suraj S. Deshpande, Lakshman Anumolu, and Mario F. Trujillo. Evaluating the performance of the two-phase flow solver interFoam. *Computational Science and Discovery*, 5:1–36, 2012.

[28] Christopher J. Doona and David M. Stanbury. Equilibrium and redox kinetics of copper(II)-thiourea complexes. *Inorganic Chemistry*, 35(11):3210–3216, 1996.

[29] A. du Plessis and E. Macdonald. Hot isostatic pressing in metal additive manufacturing: X-ray tomography reveals details of pore closure. *Additive Manufacturing*, 34:101191, 2020.

[30] I. Egry, E. Ricci, R. Novakovic, and S. Ozawa. Surface tension of liquid metals and alloys-Recent developments. *Advances in Colloid and Interface Science*, 159(2):198–212, 2010.

[31] Sebastian Engler, Reiner Ramsayer, and Reinhart Poprawe. Process studies on laser welding of copper with brilliant green and infrared lasers. *Physics Procedia*, 12(Pt. 2):342–349, 2011.

[32] By Joerg Fischer-Buehner, Pietro Poliero, Riccardo Bertoncello, Andrea Basso, and Massimo Poliero. Rapid Jewelry Manufacturing By Laser Melting of Precious Metal Powders (PLM): Fiction Or Future? In *Proc. of Santa Fe Symposium on Jewelry Manufacturing Technology*, pages 177–202, 2012.

[33] Gerald B. Folland. *Fourier Analysis and Its Applications.* American Mathematical Society, Providence, 1992.

[34] Jan Philipp Fürstenau, Henning Wessels, Christian Weißenfels, and Peter Wriggers. Generating virtual process maps of SLM using powder-scale SPH simulations. *Computational Particle Mechanics*, 7(4):655–677, 2020.

[35] A. N.D. Gasper, D. Hickman, I. Ashcroft, S. Sharma, X. Wang, B. Szost, D. Johns, and A. T. Clare. Oxide and spatter powder formation during laser powder bed fusion of Hastelloy X. *Powder Technology*, 354:333–337, 2019.

[36] Hossein Ghasemi-Tabasi, Jamasp Jhabvala, Eric Boillat, Toni Ivas, Rita Drissi-Daoudi, and Roland E. Logé. An effective rule for translating optimal selective laser melting processing parameters from one material to another. *Additive Manufacturing*, 36:101496, 2020.

[37] A. I. Golovashkin and G. P. Motulevich. Optical and Electrical Properties of Tin. *Jornal of Experimental and Theoretical Physics (U.S.S.R)*, 46(2):460–470, 1963.

[38] S. Griffiths, H. Ghasemi Tabasi, T. Ivas, X. Maeder, A. De Luca, K. Zweiacker, R. Wróbel, J. Jhabvala, R. E. Logé, and C. Leinenbach. Combining alloy and process modification for micro-crack mitigation in an additively manufactured Ni-base superalloy. *Additive Manufacturing*, 36, 2020.

[39] Darko Grujicic and Batric Pesic. Electrodeposition of copper: The nucleation mechanisms. *Electrochimica Acta*, 47(18):2901–2912, 2002.

[40] Dongdong Gu, Yifu Shen, Shangqing Fang, and Jun Xiao. Metallurgical mechanisms in direct laser sintering of Cu-CuSn-CuP mixed powder. *Journal of Alloys and Compounds*, 438(1-2):184–189, 2007.

[41] F. J. Gürtler, M. Karg, K. H. Leitz, and M. Schmidt. Simulation of laser beam melting of steel powders using the three-dimensional volume of fluid method. *Physics Procedia*, 41:881–886, 2013.

[42] Neil J. Harrison, Iain Todd, and Kamran Mumtaz. Reduction of micro-cracking in nickel superalloys processed by Selective Laser Melting: A fundamental alloy design approach. *Acta Materialia*, 94:59–68, 2015.

[43] A. Harten. High Resolution Schemes for Hyperboliy Conservation Laws. *Journal of computational physics*, 49:357–393, 1983.

[44] Hamidreza Hekmatjou and Homam Naffakh-Moosavy. Hot cracking in pulsed Nd:YAG laser welding of AA5456. *Optics and Laser Technology*, 103:22–32, 2018.

[45] Axel Hess, Rainer Schuster, Andreas Heider, Rudolf Weber, and Thomas Graf. Continuous wave laser welding of copper with combined beams at wavelengths of 1030 nm and of 515 nm. *Physics Procedia*, 12(Pt. 1):88–94, 2011.

[46] C. W. Hirt and B. D. Nichols. Volume of Fluid (VOF) Method for the Dynamics of Free Boundaries. *Journal of computational physics*, 39:201–225, 1981.

[47] Christian Hoppmann, Kirsten Bobzin, Mathias Weber, Mehmet Öte, Philipp Ochotta, and Xifang Liao. IMKS and IMMS - Two Integrated Methods for the One-Step-Production of Plastic/Metal Hybrid Parts. In Christian Brecher, editor, *Advances in Production Technology*. Springer International Publishing, Cham, 2015.

[48] Liang-Kai Huang and Mao-Jiun J. Wang. Image thresholding by minimizing the measures of fuzziness. *Pattern Recignition*, 28(1):41–51, 1995.

[49] Charles W Hull. Apparatus for Production of Three-Dimensonal Objects By Stereolithography. *US Patent No: 2,908,54510/1*, 1984.

[50] E. Huttunen-Saarivirta, T. Tiainen, and T. Lepistö. Microstructural study of the initiation and formation of immersion tin coating on copper. *Materials Science and Engineering A*, 336(1-2):52–58, 2002.

[51] Elina Huttunen-Saarivirta. Observations on the uniformity of immersion tin coatings on copper. *Surface and Coatings Technology*, 160(2-3):288–294, 2002.

[52] Toshi Taka Ikeshoji, Kazuya Nakamura, Makiko Yonehara, Ken Imai, and Hideki Kyogoku. Selective Laser Melting of Pure Copper. *Jom*, 70(3):396–400, 2018.

[53] Jadhav, Dadbakhsh, Vleugels, Hofkens, Puyvelde, Yang, Kruth, Humbeeck, and Vanmeensel. Influence of Carbon Nanoparticle Addition (and Impurities) on Selective Laser Melting of Pure Copper. *Materials*, 12(15):2469, 2019.

[54] S. D. Jadhav, S. Dadbakhsh, L. Goossens, J. P. Kruth, J. Van Humbeeck, and K. Vanmeensel. Influence of selective laser melting process parameters on texture evolution in pure copper. *Journal of Materials Processing Technology*, 270:47–58, 2019.

[55] Suraj Dinkar Jadhav, Dongmei Fu, Maxim Deprez, Kristof Ramharter, Denise Willems, Brecht Van Hooreweder, and Kim Vanmeensel. Highly conductive and strong CuSn0.3 alloy processed via laser powder bed fusion starting from a tin-coated copper powder. *Additive Manufacturing*, 36:101607, 2020.

[56] Suraj Dinkar Jadhav, Jozef Vleugels, Jean-Pierre Kruth, Jan Van Humbeeck, and Kim Vanmeensel. Mechanical and electrical properties of selective laser-melted parts produced from surface-oxidized copper powder. *Material Design & Processing Communications*, 2(2):1–8, 2019.

[57] Jamasp Jhabvala, Eric Boillat, Thibaud Antignac, and Rémy Glardon. On the effect of scanning strategies in the selective laser melting process. *Virtual and Physical Prototyping*, 5(2):99–109, 2010.

[58] Jamasp Jhabvala, Eric Boillat, and Rémy Glardon. On the use of EBSD analysis to investigate the microstructure of gold samples built by selective laser melting. *Gold Bulletin*, 44(2):113–118, 2011.

[59] Haolin Jia, Hua Sun, Hongze Wang, Yi Wu, and Haowei Wang. Scanning strategy in selective laser melting (SLM): a review. *International Journal of Advanced Manufacturing Technology*, 113(9-10):2413–2435, 2021.

[60] P.B. Johnson and R. W. Christy. Optical Constant of the Nobel Metals. *Physical Review B*, 6(12):4370–4379, 1972.

[61] Christer Jonsson, Towe Norlén, Lena Thorsson, and Björn Eklund. Sätt att framställa smycken och andra ädelmetallprodukter med komplexa geometrier. *Swedish patent no: SE527291C2*, 2003.

[62] Lisa Kaden, Gabor Matthäus, Tobias Ullsperger, Hannes Engelhardt, Markus Rettenmayr, Andreas Tünnermann, and Stefan Nolte. Selective laser melting of copper using ultrashort laser pulses. *Applied Physics A*, 123(9):596, 2017.

[63] Nikola Kalentics, Navid Sohrabi, Hossein Ghasemi Tabasi, Seth Griffiths, Jamasp Jhabvala, Christian Leinenbach, Andreas Burn, and Roland E. Logé. Healing cracks in selective laser melting by 3D laser shock peening. *Additive Manufacturing*, 30:100881, 2019.

[64] Minjung Kang, Heung Nam Han, and Cheolhee Kim. Microstructure and solidification crack susceptibility of Al 6014 molten alloy subjected to a spatially oscillated laser beam. *Materials*, 11(4), 2018.

[65] J.N. Kapur, P.K Sahoo, and A.K.C. Wong. A New Method for Gray-Level Picture Thresholding Using the Entropy of the Histogram. *Computer vision graphics and image processing*, 29:273–285, 1985.

[66] Saad A Khairallah, Andrew T Anderson, Alexander Rubenchik, and Wayne E King. Laser powder-bed fusion additive manufacturing: Physics of complex melt flow and formation mechanisms of pores, spatter, and denudation zones. *Acta Materialia*, 108:36–45, 2016.

[67] Mushtaq Khan and Phill Dickens. Selective Laser Melting (SLM) of pure gold. *Gold Bulletin*, 43(2):114–121, 2010.

[68] Charles Kittel. *Introduction to solid state physics*. John Wiley & Sons, Hoboken, NJ, 8 edition, 2005.

[69] F. Klocke and C. Wagner. Coalescence behaviour of two metallic particles as base mechanism of selective laser sintering. *CIRP Annals - Manufacturing Technology*, 52(1):177–180, 2003.

[70] Ulrich E Klotz, Dario Tiberto, and Franz Held. Additive Manufacturing of 18-Karat Yellow-Gold Alloys. In *Proc. of Santa Fe Symposium on Jewelry Manufacturing Technology*, pages 255–272, 2016.

[71] Ulrich E. Klotz, Dario Tiberto, and Franz Held. Optimization of 18-karat yellow gold alloys for the additive manufacturing of jewelry and watch parts. *Gold Bulletin*, 50(2):111–121, 2017.

[72] J. A. Koepf, D. Soldner, M. Ramsperger, J. Mergheim, M. Markl, and C. Körner. Numerical microstructure prediction by a coupled finite element cellular automaton model for selective electron beam melting. *Computational Materials Science*, 162:148–155, 2019.

[73] Carolin Körner, Matthias Markl, and Johannes A. Koepf. Modeling and Simulation of Microstructure Evolution for Additive Manufacturing of Metals: A Critical Review. *Metallurgical and Materials Transactions A: Physical Metallurgy and Materials Science*, 51(10):4970–4983, 2020.

[74] Zlata Kovac and King Ning Tu. Immersion Tin: Its Chemistry, Metallurgy, and Application in Electronic Packaging Technology. *IBM Journal of Research and Development*, 28(6):726–734, 1984.

[75] J.P Kruth, B. Vandenbroucke, J. van Vaerenbergh, and I. Naert. Rapid Manufacturing of Dental Prostheses by means of Selective Laser Sintering/Melting. In *Proceedings of the 2nd International Conference on Advanced Research in Virtual and Rapid Prototyping*, volume 4, pages 176–186, 2005.

[76] Salomea Krzewska and Halina Podsiadły. Studies on the reaction of copper(II) with thiourea-I. *Journal of Inorganic and Nuclear Chemistry*, 42(1):83–85, 1980.

[77] Salomea Krzewska, Halina Podsiadły, and Lech Pajdowski. Studies on the Reaction of Copper(II) with Thiourea-III. *Journal of Inorganic and Nuclear Chemistry*, 42:89–94, 1980.

[78] Salomea Krzewska, Halina Podsiadły, and Lech Pajdowski. Studies on the reaction of copper(II) with thiourea—II. *Journal of Inorganic and Nuclear Chemistry*, 42(1):89–94, 1980.

[79] Ralf Larson. Sätt och anordning för siktvis framställning av koppar från pulver. *Swedish patent no: SE504560*, 1993.

[80] K. Q. Le, C. Tang, and C. H. Wong. On the study of keyhole-mode melting in selective laser melting process. *International Journal of Thermal Sciences*, 145(May), 2019.

[81] Jae Y. Lee, Sung H. Ko, Dave F. Farson, and Choong D. Yoo. Mechanism of keyhole formation and stability in stationary laser welding. *Journal of Physics D: Applied Physics*, 35(13):1570–1576, 2002.

[82] Joonho Lee, Wataru Shimoda, and Toshihiro Tanaka. Surface tension and its temperature coefficient of liquid Sn-X (X=Ag, Cu) alloys. *Materials Transactions*, 45(9):2864–2870, 2004.

[83] Y. S. Lee and W. Zhang. Modeling of heat transfer, fluid flow and solidification microstructure of nickel-base superalloy fabricated by laser powder bed fusion. *Additive Manufacturing*, 12:178–188, 2016.

[84] Ruidi Li, Jinhui Liu, Yusheng Shi, Li Wang, and Wei Jiang. Balling behavior of stainless steel and nickel powder during selective laser melting process. *International Journal of Advanced Manufacturing Technology*, 59(9-12):1025–1035, 2012.

[85] Xiaoshuang Li. *Rapid Solidification of Alloys and Selective laser Melting of Metal Matrix Composites for Abrasive Applications.* PhD thesis, ETH Zürich, 2019.

[86] Xuan Liang, Lin Cheng, Qian Chen, Qingcheng Yang, and Albert C. To. A modified method for estimating inherent strains from detailed process simulation for fast residual

distortion prediction of single-walled structures fabricated by directed energy deposition. *Additive Manufacturing*, 23:471–486, 2018.

[87] Viktor Lindström and Christian Leinenbach. Modeling and simulation of balling defect formation during laser powder bed fusion. *In submission*, 2021.

[88] Viktor Lindström, Oleksii Liashenko, Kai Zweiacker, Serhii Derevianko, Vladyslav Morozovych, Yurij Lyashenko, and Christian Leinenbach. Laser powder bed fusion of metal coated copper powders. *Materials*, 13(16), 2020.

[89] Jiangwei Liu, Pingwang Zeng, and Sindo Kou. Solidification cracking susceptibility of quaternary aluminium alloys. *Science and Technology of Welding and Joining*, 26(3):244–257, 2021.

[90] R. Liu, Z. Wang, T. Sparks, F. Liou, and J. Newkirk. *Aerospace applications of laser additive manufacturing.* Elsevier Ltd, Amsterdam, 2017.

[91] Yang Liu, Yongqiang Yang, and Di Wang. A study on the residual stress during selective laser melting (SLM) of metallic powder. *International Journal of Advanced Manufacturing Technology*, 87(1-4):647–656, 2016.

[92] P.A. Lykov, E.V. Safonov, and A.M. Akhmedianov. Selective Laser Melting of Copper. *Materials Science Forum*, 843:284–288, 2016.

[93] M. N. Polyanskiy. Refractive index database. https://refractiveindex.info, accesed on 2018-08-10.

[94] Zhongfa Mao, David Z. Zhang, Junjie Jiang, Guang Fu, and Peng Zhang. Processing optimisation, mechanical properties and microstructural evolution during selective laser melting of Cu-15Sn high-tin bronze. *Materials Science and Engineering A*, 721:125–134, 2018.

[95] Zhongfa Mao, David Z. Zhang, Peitang Wei, and Kaifei Zhang. Manufacturing feasibility and forming properties of Cu-4Sn in selective laser melting. *Materials*, 10(333), 2017.

[96] Hiroshige Masuo, Yuzo Tanaka, Shotaro Morokoshi, Hajime Yagura, Tetsuya Uchida, Yasuhiro Yamamoto, and Yukitaka Murakami. Influence of defects, surface roughness and HIP on the fatigue strength of Ti-6Al-4V manufactured by additive manufacturing. *International Journal of Fatigue*, 117(April):163–179, 2018.

[97] R. A. Matula. Electrical resistivity of copper, gold, palladium, and silver. *Journal of Physical and Chemical Reference Data*, 8(4):1147–1298, 1979.

[98] Peter Mercelis and Jean Pierre Kruth. Residual stresses in selective laser sintering and selective laser melting. *Rapid Prototyping Journal*, 12(5):254–265, 2006.

[99] Jitka Metelkova, Daniel Ordnung, Yannis Kinds, and Brecht Van Hooreweder. Novel strategy for quality improvement of up-facing inclined surfaces of LPBF parts by combining laser-induced shock waves and in situ laser remelting. *Journal of Materials Processing Technology*, 290(August 2020):116981, 2021.

[100] Jane C. Miller. Optical properties of liquid metals at high temperatures. *Philosophical Magazine*, 20(168):1115–1132, 1969.

[101] Elham Mirkoohi, Daniel E. Seivers, Hamid Garmestani, and Steven Y. Liang. Heat source modeling in selective laser melting. *Materials*, 12(13):1–18, 2019.

[102] Muhammad and C. W. Lim. Phononic metastructures with ultrawide low frequency three-dimensional bandgaps as broadband low frequency filter. *Scientific Reports*, 11(1):1–11, 2021.

[103] J. P. Neumann, T. Zhong, and Y. A. Chang. The Cu-O (Copper-Oxygen) system. *Bulletin of Alloy Phase Diagrams*, 5(2):136–140, 1984.

[104] Tuan D. Ngo, Alireza Kashani, Gabriele Imbalzano, Kate T.Q. Nguyen, and David Hui. Additive manufacturing (3D printing): A review of materials, methods, applications and challenges. *Composites Part B: Engineering*, 143(December 2017):172–196, 2018.

[105] Carl Nordling and Jonny Österman. *Physics Handbook for Science and Engineering*. Studentlitteratur AB, Lund, 2 edition, 2006.

[106] Towe Norlen. Private communication over phone, 2018-04-20, 2018.

[107] A C Nunes. An Extended Rosenthal Weld Model: A moving heat source weld model can be extended to include effects of phase changes and circulations in the weld pool. *Welding journal*, 62(6):165–170, 1983.

[108] Paulo J . Oliveira and Raad I Issa. An improved PISO algorithm for the computation of boyancy driven flows. *Numerical Heat Transfer*, 40:473–493, 2001.

[109] Mark A. Ordal, Robert J. Bell, Ralph W. Alexander, Larry L. Long, and Marvin R. Querry. Optical properties of Au, Ni, and Pb at submillimeter wavelengths. *Applied Optics*, 26(4):744, 1987.

[110] M. Otter. Temperaturabhängigkeit der optischen Konstanten massiver Metalle. *Zeitschrift für Physik*, 161(5):539–549, 1961.

[111] Nachiket Patil. A Novel Numerical Framework for Simulation ofMultiscale Spatio-Temporally Non-Linear Systems inAdditive Manufacturing Processes. *Department of Industrial Engineering*, 2014.

[112] S. R. Pogson, P. Fox, C. J. Sutcliffe, and W. O'Neill. The production of copper parts using DMLR. *Rapid Prototyping Journal*, 9(5):334–343, 2003.

[113] Reinhart Poprawe, Christian Hinke, Wilhelm Meiners, Johannes Schrage, Sebastian Bremen, and Simon Merkt. SLM Production Systems: Recent Developments in Process Development, Machine Concepts and Component Design. In Christian Brecher, editor, *Advances in Production Technology*. Springer International Publishing, Cham, 2015.

[114] Alexander M. Rubenchik, Wayne E. King, and Sheldon S. Wu. Scaling laws for the additive manufacturing. *Journal of Materials Processing Technology*, 257:234–243, 2018.

[115] W. J. Sames, F. A. List, S. Pannala, R. R. Dehoff, and S. S. Babu. The metallurgy and processing science of metal additive manufacturing. *International Materials Reviews*, 61(5):315–360, 2016.

[116] Benjamin Scharifker. Theoretical and experimental studies of multiple nucleation. *Electrochemica Acta.*, 28(7):879–889, 1983.

[117] Johannes Schindelin, Ignacio Arganda-Carreras, Erwin Frise, Verena Kaynig, Mark Longair, Tobias Pietzsch, Stephan Preibisch, Curtis Rueden, Stephan Saalfeld, Benjamin Schmid, Jean Yves Tinevez, Daniel James White, Volker Hartenstein, Kevin Eliceiri, Pavel Tomancak, and Albert Cardona. Fiji: An open-source platform for biological-image analysis. *Nature Methods*, 9(7):676–682, 2012.

[118] Günther Schuh, Christina Reuter, Annika Hauptvogel, and Christian Dölle. Hypotheses for a Theory of Production in the Context of Industrie 4.0. In Christian Brecher, editor, *Advances in Production Technology*. Springer International Publishing, Cham, 2015.

[119] S. Scudino, C. Unterdörfer, K. G. Prashanth, H. Attar, N. Ellendt, V. Uhlenwinkel, and J. Eckert. Additive manufacturing of Cu-10Sn bronze. *Materials Letters*, 156:202–204, 2015.

[120] Vladimir Semak and Akira Matsunawa. The role of recoil pressure in energy balance during laser materials processing. *Journal of Physics D: Applied Physics*, 30(18):2541–2552, 1997.

[121] Iñaki Setien, Michele Chiumenti, Sjoerd van der Veen, Maria San Sebastian, Fermín Garciandía, and Alberto Echeverría. Empirical methodology to determine inherent strains in additive manufacturing. *Computers and Mathematics with Applications*, 78(7):2282–2295, 2019.

[122] V. Shankar, T. P.S. Gill, S. L. Mannan, and S. Sundarlsan. Solidification cracking in austenitic stainless steel welds. *Sadhana - Academy Proceedings in Engineering Sciences*, 28(3-4):359–382, 2003.

[123] S. A. Shevchik, C. Kenel, C. Leinenbach, and K. Wasmer. Acoustic emission for in situ quality monitoring in additive manufacturing using spectral convolutional neural networks. *Additive Manufacturing*, 21:598–604, 2018.

[124] Sergey A. Shevchik, Tri Le-Quang, Farzad Vakili Farahani, Neige Faivre, Bastian Meylan, Silvio Zanoli, and Kilian Wasmer. Laser welding quality monitoring via graph support vector machine with data adaptive kernel. *IEEE Access*, 7:93108–93122, 2019.

[125] Edward Siegel. Optical reflectivity of liquid metals at their melting temperatures Optical Reflectivity of Liquid Metals at their Melting Temperatures. *Physics and Chemistry of Liquids*, 5(1):9–27, 1976.

[126] Cassidy Silbernagel, Leonidas Gargalis, Ian Ashcroft, Richard Hague, Michael Galea, and Phill Dickens. Electrical resistivity of pure copper processed by medium-powered laser powder bed fusion additive manufacturing for use in electromagnetic applications. *Additive Manufacturing*, 29:1–11, 2019.

[127] A. B. Spierings, M. Voegtlin, T. Bauer, and K. Wegener. Powder flowability characterisation methodology for powder-bed-based metal additive manufacturing. *Progress in Additive Manufacturing*, 1(1-2):9–20, 2016.

[128] Ernie W Spisz, Albert J Weigund, Robert L Bowmun, and John R Juck. Solar absorptances and spectral reflectances of 12 metals for temperatures ranging from 300 to 500 K. *NASA Technical Note*, TN D-5353, 1969.

[129] Peter Stritt, Christian Hagenlocher, Christine Kizler, Rudolf Weber, Christoph Rüttimann, and Thomas Graf. Laser spot welding of copper-aluminum joints using a pulsed dual wavelength laser at 532 and 1064 nm. *Physics Procedia*, 56(C):759–767, 2014.

[130] Josefine Svenungsson. *Conduction laser welding modelling of melt pool with free surface deformation*. PhD thesis, University West, 2019.

[131] Mohsen Taheri Andani, Reza Dehghani, Mohammad Reza Karamooz-Ravari, Reza Mirzaeifar, and Jun Ni. A study on the effect of energy input on spatter particles creation during selective laser melting process. *Additive Manufacturing*, 20:33–43, 2018.

[132] Ming Tang, P. Chris Pistorius, and Jack L. Beuth. Prediction of lack-of-fusion porosity for powder bed fusion. *Additive Manufacturing*, 14:39–48, 2017.

[133] Dario Tiberto, Ulrich E. Klotz, Franz Held, and Gerhard Wolf. Additive manufacturing of copper alloys: influence of process parameters and alloying elements. *Materials Science and Technology (United Kingdom)*, 35(8):969–977, 2019.

[134] E. Uhlmann, A.E. Tekkaya, V. Kasjevko, S. Gies, R. Reimann, and P. John. Qualification of CuCr1 for the SLM Process. In *7th International Conference on High Speed Forming*, pages 173–182, 2016.

[135] Kikuo Ujihara. Reflectivity of metals at high temperatures. *Journal of Applied Physics*, 43(5):2376–2383, 1972.

[136] Naor Elad Uzan, Shlomo Ramati, Roni Shneck, Nachum Frage, and Ori Yeheskel. On the effect of shot-peening on fatigue resistance of AlSi10Mg specimens fabricated by additive manufacturing using selective laser melting (AM-SLM). *Additive Manufacturing*, 21(March):458–464, 2018.

[137] H.K. Versteeg and W Malalasekera. *An Introduction to Computational Fluid Dynamics: The Finite Volume Method.* Pearson Education Limited, London, 2nd edition, 2007.

[138] Viktor Lindström and Christian Leinenbach. The influence of the processing parameters on selective laser melting of copper using a green laser source, 2020.

[139] William T Walter. Change in reflectivity of metals under intense laser radiation. Technical report, Polytechnic Institute of New York, 1981.

[140] Kaiwen Wei, Xiaoyan Zeng, Zemin Wang, Jinfeng Deng, Mengna Liu, Gao Huang, and Xiaochi Yuan. Selective laser melting of Mg-Zn binary alloys: Effects of Zn content on densification behavior, microstructure, and mechanical property. *Materials Science and Engineering A*, 756:226–236, 2019.

[141] Johannes Weirather, Vladyslav Rozov, Mario Wille, Paul Schuler, Christian Seidel, Nikolaus A. Adams, and Michael F. Zaeh. A Smoothed Particle Hydrodynamics Model for Laser Beam Melting of Ni-based Alloy 718. *Computers and Mathematics with Applications*, 78(7):2377–2394, 2019.

[142] H. G. Weller, G. Tabor, H. Jasak, and C. Fureby. A tensorial approach to computational continuum mechanics using object-oriented techniques. *Computers in Physics*, 12(6):620, 1998.

[143] James R. Welty, Charles E. Wicks, Robert E. Wilson, and Gregory Rorrer. *Fundamentals of momentum, heat and mass transfer.* John Wiley & Sons, 5th edition, 2000.

[144] Kaufui V. Wong and Aldo Hernandez. A Review of Additive Manufacturing. *ISRN Mechanical Engineering*, 2012:1–10, 2012.

[145] Gentry Wood, Shahrukh Al Islam, and Patricio F. Mendez. Calibrated expressions for welding and ther application to isotherm width in a thick plate. *Soldagem e Inspecao*, 19(3):212–220, 2014.

[146] I. Yadroitsev, A. Gusarov, I. Yadroitsava, and I. Smurov. Single track formation in selective laser melting of metal powders. *Journal of Materials Processing Technology*, 210(12):1624–1631, 2010.

[147] E. Yasa, J. P. Kruth, and J. Deckers. Manufacturing by combining Selective Laser Melting and Selective Laser Erosion/laser re-melting. *CIRP Annals - Manufacturing Technology*, 60(1):263–266, 2011.

[148] T. E. Zavecz, M. A. Saifi, and M. Notis. Metal reflectivity under high-intensity optical radiation. *Applied Physics Letters*, 26(4):165–168, 1975.

[149] D.Q. Zhang, Z.H. Liu, and C.K. Chua. Investigation on forming process of Cu by SLM. In *High value manufacturing: Advanced Research in Virtual and Rapid Prototyping*, pages 285–289. Taylor & Francis, 2014.

[150] Pu Zhang, Jakub Toman, Yiqi Yu, Emre Biyikli, Mesut Kirca, Markus Chmielus, and Albert C. To. Efficient design-optimization of variable-density hexagonal cellular structure by additive manufacturing: Theory and validation. *Journal of Manufacturing Science and Engineering, Transactions of the ASME*, 137(2):41–45, 2015.

[151] Yanning Zhang and Amit Bandyopadhyay. Direct fabrication of bimetallic Ti6Al4V+Al12Si structures via additive manufacturing. *Additive Manufacturing*, 29:100783, 2019.

[152] Cang Zhao, Kamel Fezzaa, Ross W. Cunningham, Haidan Wen, Francesco De Carlo, Lianyi Chen, Anthony D. Rollett, and Tao Sun. Real-time monitoring of laser powder bed fusion process using high-speed X-ray imaging and diffraction. *Scientific Reports*, 7(1):1–11, 2017.

[153] Xiaoming Zhao, Xin Lin, Jing Chen, Lei Xue, and Weidong Huang. The effect of hot isostatic pressing on crack healing, microstructure, mechanical properties of Rene88DT superalloy prepared by laser solid forming. *Materials Science and Engineering A*, 504(1-2):129–134, 2009.

[154] Longchao Zhuo, Zeyu Wang, Hongjia Zhang, Enhuai Yin, Yanlin Wang, Tao Xu, and Chao Li. Effect of post-process heat treatment on microstructure and properties of selective laser melted AlSi10Mg alloy. *Materials Letters*, 234:196–200, 2019.

[155] Damiano Zito. Why Should We Direct 3D Print Jewelry? A Comparison between Two Thoughts: Today and Tomorrow. In *Proc. of Santa Fe Symposium on Jewelry Manufacturing Technology*, pages 515–556, 2017.

[156] Damiano Zito, Alessio Carlotto, Alessandro Loggi, Patrizio Sbornicchia, Daniele Maggian, S A Progold, Peter Unterberg, and Matthias Fockele. Optimization of SLM Technology Main Parameters in the Production of Gold and Platinum Jewelry. In *Proc. of Santa Fe Symposium on Jewelry Manufacturing Technology*, pages 439–470, 2014.

[157] Damiano Zito, Alessio Carlotto, Alessandro Loggi, Patrizio Sbornicchia, Daniele Maggian, S A Progold, Trissino Vi, Matthias Fockele, and Peter Unterberg. Optimization of the Main Selective Laser Melting Technology Parameters in the Production of Precious Metal Jewelry. In *Proc. of Santa Fe Symposium on Jewelry Manufacturing Technology*, pages 1–20, 2013.

Viktor Lindström

Hüeblistrasse 112, 8636 Wald

epfl@lindstroem.ch
+41 (0)76 386 2238

Date of birth:	10.01.1990
Nationality:	Sweden
Residence permit:	B

Academic background

2017– 2021	**Empa/EPFL** **PhD Student** **Thesis**: Defect formation and mitigation during laser powder bed fusion of copper
2017	**ETH Zürich** **Master Thesis** at the *Materials Theory* group in the *Department of Materials Science* **Thesis**: First principles-based computational study of Fe-Ni-based compounds
2014-2017	**Chalmers University of Technology, Gothenburg, Sweden** **MSc Student** in Applied Physics
2014-2015	**ETH Zürich** **Exchange student** through the *UNITECH* program, *Department of Physics*
2010-2013	**Chalmers University of Technology, Gothenburg, Sweden** **BSc student** in Chemical Engineering with Engineering Physics **Thesis:** Indunstningsmetodens påverkan på frisättningen av 2-n-oktyl-4-isotiazol-3-on ur mikrosfärer av polymetylmetakrylat

Professional experience

2016	**ABB Corporate Research, Baden, Switzerland** **Intern**, Semiconductor Packaging

Languages

English	C2
German	C1
Swedish	Mother tongue

Publications and scientific conference contributions

Lindström Viktor & Leinenbach Christian, " Modeling and simulation of balling defect formation during laser powder bed fusion". *In submission.* 2021

Lindström Viktor & Leinenbach Christian, "Influence of process parameters of SLM of copper using a green laser source." *Material Science and Engineering Congress,* 2020.

Lindström, Viktor, et al. "Laser Powder Bed Fusion of Metal Coated Copper Powders." *Materials* 13.16 (2020): 3493.

Lindström Viktor, et al. "Powder coating as an alloying strategy for selective laser melting of copper alloys*." AAMS; Alloys for additive manufacturing symposium.* 2019

Schuderer, Juergen, et al. "Transfer molding for power semiconductor modules." *CIPS 2018; 10th International Conference on Integrated Power Electronics Systems*. VDE, 2018.